NTNU – Trondheim
Norwegian University of
Science and Technology

Modelling and Control of Six-Phase Induction Motor Drive

Nebrom Berihu Araya

Master of Science in Electric Power Engineering
Submission date: July 2012
Supervisor: Tom F. Nestli, ELKRAFT
Co-supervisor: Roy Nilsen, Wärtsilä Norway AS

Norwegian University of Science and Technology
Department of Electric Power Engineering

Modelling and Control of Six-Phase Induction Motor Drive

by

Nebrom Berihu Araya

A thesis submitted to

Department of Electric Power Engineering
Norwegian University of Science and Technology

in partial fulfillment of the requirements for the degree
Master of Science
in Electric Power Engineering

July 2012

Problem Description

Multiphase machines are of interest to be applied in electric ship propulsion where increased power ratings, reliability of operation, redundancy and efficiency are required. The study of modelling and control of multiphase drives is important to realize this application. A general model of six-phase machines has been developed. Control methods for Induction Machine and Permanent Magnet Machines have been simulated in previous works. Detailed simulation models of inverters have also been developed.

A laboratory setup for a six-phase induction machine was assembled and programmed for Double Synchronous Frame Current Control in a previous master thesis. In a specialization project, the student has carried out a simulation study of modelling and current control methods in six-phase machines. This master thesis should build on the previous results. In this thesis work, the student should

- Carry out a more detailed simulation study of both Double Synchronous Frame Current Control (DSFCC) & Single Synchronous Frame Current Control (SSFCC) using Matlab Simulink/SimPowerSystems.
- Improve the DSFCC control method using new transformation methods and limiter functions in order to avoid unstable oscillations and improve response to DC link under-voltage.
- Implement and test the control methods in the existing laboratory setup for a six-phase induction machine.

Assignment given: 30. January 2012

Supervisor: Tom F. Nestli, Elkraft
Co-supervisor: Roy Nilsen, Wärtsilä Norway

Preface

This master thesis was done in cooperation with Wärtsilä Norway AS. The thesis work has been both challenging and interesting, and it has given me valuable experience in my education.

I would like to thank Professor Tom F. Nestli, my supervisor, for his guidance and for giving me the opportunity to explore this important field of application. I am very grateful to Professor Roy Nilsen of Wärtsilä Norway. He has contributed immensely to this work through many discussions, literature and simulation models. I want to thank Mr Sachin Thopate for his guidance as I learned the drive setup in July 2011. I would also like to thank the administrative and technical staff in the department of Electric Power Engineering for providing me the necessary resources. Lastly, I thank my family and friends for their love and encouragement.

Nebrom Berihu Araya

Trondheim, Norway

July 2012

Abstract

Multiphase machines are of interest to be applied in electric ship propulsion, where increased power ratings, reliability of operation, redundancy and efficiency are required. The study of modelling and control of multiphase drives is important to realize this application.

The main purpose of this thesis was to implement and test control methods for a six-phase induction motor drive. The work focused on continuation and improvement of previous results achieved in the same area of application. The modelling of six-phase induction machine using two different approaches was studied. Based on these approaches, two types of vector control methods were implemented. These are single synchronous frame control (SSFC) and double synchronous frame control (DSFC).

The six-phase induction motor drive was tested for different operating conditions using the two control methods. The motor is normally supplied from two inverters with a split DC link. The DC link voltages are kept equal and the two 3-phase groups of the motor share the torque and power equally. Testing the drive during normal operation showed desired control performance using both SSFC and DSFC methods.

Asymmetrical operation of the drive was also investigated. In this case, the currents in the two 3-phase groups of the six-phase motor are unequal. Thus, both do not have equal contribution to the torque developed in the motor. The results obtained using SSFC and DSFC are as desired in both torque control and speed control modes.

The third case of interest in the drive testing was the investigation of supply asymmetries and faults. During under-voltage in one DC link, failure of one rectifier, or trip of one inverter, the DSFC method gave desired response in both torque control and speed control modes. Similar results were obtained using SSFC except for the case of inverter trip during speed control mode.

From the results obtained, it was concluded that both SSFC and DSFC methods give desired performance during normal operation of the drive. This is also the case for current asymmetries in the motor when there are no supply faults. In the case of supply faults, the DSFC method gave better control of the drive. The DSFC method was also found to be simpler to implement and less computationally demanding.

Contents

List of Figures

List of Tables

Acronyms

AC	Alternating Current
CSI	Current Source Inverter
DC	Direct Current
DSFC	Double Synchronous Frame Control
FPGA	Field Programmable Gate Array
IM	Induction Machine
MSPS	Million Samples Per Second
PI	Proportional Integral
pu	per unit
PWM	Pulse Width Modulation
SPWM	Sinusoidal Pulse Width Modulation
SSFC	Single Synchronous Frame Control
VSI	Voltage Source Inverter

Notations

Symbol	Explanation
U	Voltage
I	Current
R	Resistance
L	Inductance
Ψ	Flux linkage
S	Apparent power
P	Real power
φ	power factor angle
$\underline{U}$	Column matrix of voltages
$\underline{I}$	Column matrix of currents
$\underline{\Psi}$	Column matrix of flux linkages
$\mathbf{R}$	Matrix of resistances
$\mathbf{L}$	Matrix of inductances
x_s	stator reactance
$x_{s\sigma}$	stator leakage reactance
x_r	rotor reactance
$x_{r\sigma}$	rotor leakage reactance
x_h	mutual reactance
x_d	direct axis reactance
x_q	quadrature axis reactance
T_r	Rotor time constant
n	Rotor speed [pu]
f_k	Synchronous speed [pu]
f_r	Slip speed [pu]
ω_n	Rated angular speed, electrical
θ	Rotor angle, electrical
θ_k	Angle of rotor flux vector, electrical
θ_r	Angle of rotor flux vector with respect to rotor, electrical

J	Total moment of inertia of drive referred to the machine side
Ω	Angular speed, mechanical
M_e	Electromagnetic torque
M_L	Load Torque
θ_{mech}	Rotor angle, mechanical
p	number of pole pairs
T_m	Mechanical time constant
U_{dc1}	DC link voltage 1
U_{dc2}	DC link voltage 2
u_{st}	Control voltage
ζ	Angle of voltage space vector
ω_s	Angular speed of voltage space vector
$\mathbf{T}_{SS}$	Transformation matrix for stator quantities
$\mathbf{T}_{RR}$	Transformation matrix for rotor quantities
$\mathbf{T}$	Total transformation matrix
$\mathbf{J}$	Rotation matrix used in transformation

Superscript	**Explanation**
S	Stator quantities in stator coordinates
R	Rotor quantities in rotor coordinates
SR	Both stator and rotor quantities in their original coordinates
s	parameter referred to stator
r	parameter referred to rotor
k	parameter referred to a synchronously rotating frame
I	parameter or quantity in single synchronous modelling
II	parameter or quantity in single synchronous modelling

Subscript	**Explanation**
a_1, b_1, c_1	Phase group 1 of a six phase machine
a_2, b_2, c_2	Phase group 1 of a six phase machine
d	d-axis quantity
q	q-axis quantity
z_1	z_1-axis quantity
z_2	z_2-axis quantity
0_1	0_1-axis quantity
0_2	0_2-axis quantity
s	stator quantity
r	rotor quantity
N	rated (nominal) value
n	basis (reference) value
ph	phase
LL	line-to-line

1 Introduction

1.1 Background

Electric propulsion for ships emerged during the early 20th century. However, propulsion systems driven by diesel engines and gas turbines have been the most widely used. Electric ship propulsion has gained a renewed interest during recent decades because it provides several advantages. Some of these benefits include reduced fuel consumption and maintenance, improved maneuverability, less propulsion noise and vibration, reduced vulnerability to a single system failure and flexibility in location of thruster devices [1]. The increased interest in electric ship propulsion can be mainly attributed to advances in power electronics, digital control systems and electric machine design. These advances have enabled the recently increasing applications of electric motor drives in the marine industry [2].

A number of requirements exist for the application of electric drives in ship propulsion. These include high power ratings, efficiency, reliability and fault tolerant operation. In meeting these requirements, multiphase machine drives can be better alternatives as compared to the conventional three-phase machine drives [3]. Multiphase drives possess several advantages over conventional three-phase drives such as: reduced current stress on power electronic switches without reducing the power, lower electromagnetic torque pulsations, reduced rotor harmonic losses, reduced harmonic currents of the DC link current, and improved overall system reliability [4]-[6], [22]. Multiphase machines can have various possible phase numbers including 5, 6, 7, 9, 12 and 18 [4]. Among these the six-phase machine with two sets of three-phase windings spatially shifted by 30 electrical degrees is probably the most widely studied.

Wärtsilä, a leading company in marine solutions and flexible power plants, has been conducting research on the application of multiphase drives in electric ship propulsion. Some of the work has served as the main reference for this thesis. Modelling of synchronous machines with 2, 3, 6 and 9 phases was presented in [7], whereas [8] discussed modelling techniques for six-phase PM machines. Modelling and control of a six-phase permanent magnet synchronous machine (PMSM) was discussed in [9]. This work presented simulation results of double synchronous frame current control (DSFCC) in six-phase PMSM supplied by two three-phase inverters with separate DC links. In [10] simulation results on control of six-phase PMSM using two different current control methods were presented. The control of a six-phase induction motor drive was implemented in a laboratory setup in the work documented in [11]. Based on this work, study of the drive system and implementation of limiter functions was done on the same laboratory setup in [12]. The modelling and control of six-phase PM machine was carried out in [13], and simulation results were presented. The modelling of six-phase induction machine was also presented in the same work.

The work done in this thesis concentrates on the modelling and control of six-phase induction machine. Theoretical study and experimental implementation are both presented. The models, control methods and results in the aforementioned works are the bases for this project. The challenges documented in these papers are studied to get insight for improved modelling and control methods.

1.2 Literature Review

The study of electrical machines with more than three phases dates back to the 1910s. The theory for three, four and six – phase armature windings for a symmetrical poly-phase system was presented in [14]. Double winding generators were proposed later in order to reduce the fault current stress on circuit breakers [15]. The extension of Park's 2-reaction theory to multiphase synchronous machines was discussed in [16]. However, there was limited opportunity for application of multiphase machines. One of the reasons for this is the machines had to be supplied from three phase sources as power processing units were yet to come.

Research on multiphase machines started to get more attention in early 1970s with the advent of power diodes and thyristors. Nelson and Krause [17] presented analysis of multiphase induction machines with arbitrary displacements between winding sets. They also indicated that, in a machine with two three phase groups, an arrangement with 30 electrical degree displacement between the two phase groups gives significantly improved torque characteristic. Lipo [18] presented a d-q model for a six-phase machine supplied from a current source inverter (CSI). A comprehensive work including space harmonics, time harmonics and symmetrical component analysis of multiphase induction motors was done by Klingshirn [4]. Experimental work on six- and nine-phase machines was also presented by the same author [19]. A six-phase induction motor voltage driven by a voltage source inverter (VSI) was presented in [20].

Lipo and Zhao [21] introduced the modelling of six-phase induction machine using vector space decomposition. This was an important work that simplified the modelling and control of six-phase machines. It simplified the vector control of these machines using space vector and other PWM techniques. Research on multiphase machines has proliferated over the last decade. In many of the publications, the most widely discussed multiphase machine is a six-phase induction machine with 30 electrical degree separation between phase groups and with isolated neutral points [5], [6], [20]-[26].

The six-phase induction machine can be modelled using the technique of vector space decomposition as demonstrated in [21], [24]-[26]. This method results in a model of the machine in single six-phase reference frame with three pairs of axes decoupled from one another. A less common modelling technique is the dual stator approach mentioned in [23], [24] and [26]. It considers the six-phase machine as two coupled three-phase machines, and uses three phase transformations.

Vector control is the commonly used control technique for multiphase induction machines although direct torque control can also be used [22]-[24]. Two different current control techniques can be used in vector (field oriented) control: double synchronous frame control (DSFC) and single synchronous frame control (SSFC) [24]. Current control in stationary reference frame is also mentioned in [25]. There are various pulse width modulation (PWM) techniques for VSI driven multiphase induction machine. Sinusoidal PWM, sinusoidal PWM with third harmonic injection, and different variations of space vector PWM are the most common as discussed in [6], [22] and [27].

In many of the publications referred, only normal operation of six-phase induction machine is considered [5][21] [24][25]. The two stator phase groups of the machine share the power equally. Moreover, the machine is supplied using a six-phase VSI. The analysis in [26] considered unbalanced current sharing between the two phase groups. Fault tolerance operation of multiphase drives to open circuit in one or some of the phases is discussed in [28] and [29]. The work in [30] analyzed the fault tolerant operation to one or more failed inverters in a six-phase induction machine supplied by four 2-level three-phase inverters.

In this thesis, the modelling and control of six-phase induction machine in both single and double synchronous frames is investigated. The machine is supplied from two 2-level three-phase inverters with split DC link. Modelling of these inverters is also discussed. The results of experimental work are presented and discussed. Normal drive operation, and fault tolerant operation during current asymmetries, supply asymmetries and failures are investigated.

1.3 Thesis Scope and Limitations

This thesis focuses on modelling and control of six-phase machine. Scope of the work includes:

- Modelling of six-phase induction machine in single and double synchronous frames,
- Modelling of inverters for six-phase machine,
- Control techniques for six-phase induction motor drive in single and double synchronous frames,
- Experimental results of normal and fault tolerant operation of the drive, and
- Analysis of the results, including comparison between the two techniques.

Limitations of the work include:

- Experimental parameter identification of the six-phase induction machine is not considered.
- Field weakening operation of the drive is not studied.
- PWM techniques considered are SPWM and SPWM with 3rd harmonic injection.

In addition to these limitations, a number of simplifying but appropriate assumptions are taken into account in the modelling of the machine, inverters and control structures. These have been explained in their respective topics.

1.4 Organization of the Report

In chapter 1, the background and motivation for the thesis, the scope and limitations of the work, and a brief literature review are presented. Chapter 2 deals with the modelling of six-phase induction machine in both single and double synchronous reference frames. Modelling and modulation techniques for 2-level three-phase inverters are discussed in chapter 3. Chapter 4 presents control methods (DSFC and SSFC) for six-phase induction machine. The experimental setup used in the thesis work is discussed in chapter 5, whereas chapter 6 presents the simulation and experimental results. The results for different operating conditions are included. In chapter 7, discussion of the experimental results is presented. Finally, chapter 8 concludes the report with recommendations for further work. Moreover, the machine nameplate data and parameters, control parameters and additional simulation results are included in the appendix.

2 Modelling of Six-Phase Induction Machine

2.1 Introduction

An induction machine is a type of AC machine in which alternating current is supplied to the stator windings directly. Alternating current also flows in the rotor due to electromagnetic induction from the stator. The rotor, which is separated from the stator by an air-gap, can be of two types. A wound rotor has a winding similar to and with the same number of poles as the stator, and slip rings are used to connect it to external circuit. A squirrel-cage rotor, on the other hand, is built with conducting bars embedded in the rotor iron and short-circuited at each end by conducting rings [31].

The three-phase induction machine with squirrel-cage rotor is the most widely used electrical machine industry. Single-phase induction machines have also been commonly used in household appliances, whereas two-phase induction machines are mainly used as servomotors in a control system [32]. Recently multiphase induction machines, i.e. having more than three phases, have gained increased interest mainly in some specialized applications including electric ship propulsion and traction. This is because multiphase machines have better efficiency, greater fault tolerance and less susceptibility to time harmonics than their three-phase counterparts [22].

In this work a six-phase induction machine with squirrel-cage rotor is considered. The stator of the machine has two three-phase winding sets which are separated by 30 electrical degrees in space. Each phase group is star-connected and has three windings separated by 120 electrical degrees. The two phase groups have isolated neutrals. All the stator phase windings are distributed sinusoidally, giving a synchronously rotating sinusoidal magnetic field around the air gap of the machine. A schematic representation of the machine is shown in Figure 2.1. A machine with one pole pair is shown for simplicity, whereas the actual machine considered has two pole pairs (four poles). Phase group 1 stator winding axes are labeled as a_1^s, b_1^s and c_1^s; whereas a_2^s, b_2^s and c_2^s indicate axes of phase group 2 stator windings. Each winding is shown as a concentrated coil along its own magnetic axis.

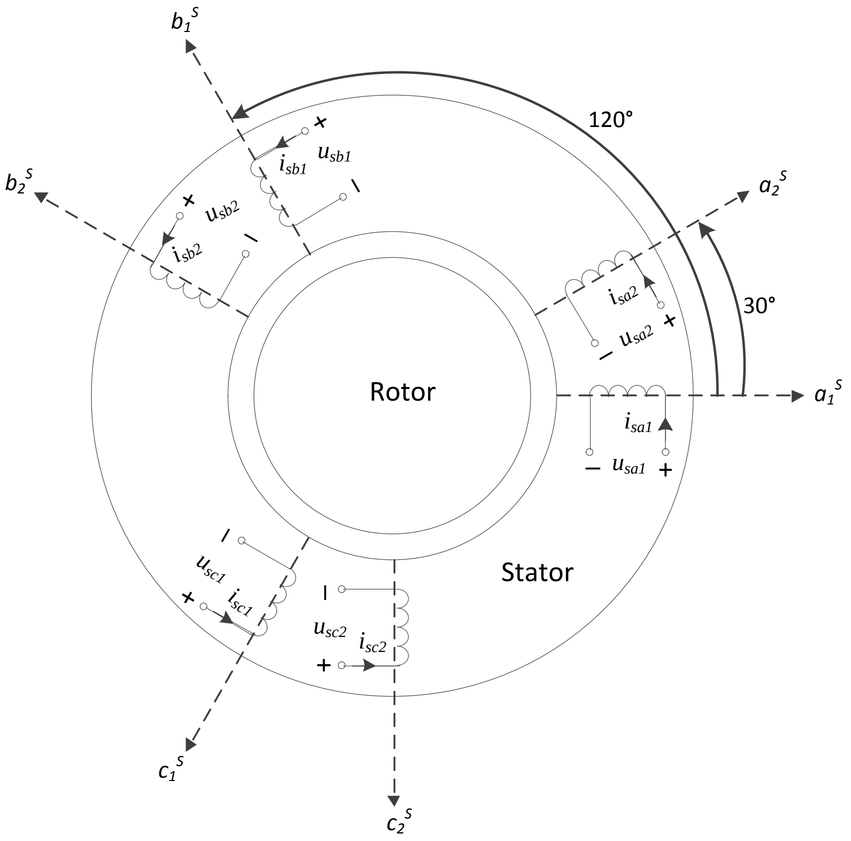

Figure 2.1: Schematic representation of six-phase induction machine

Modelling of the machine is needed in order to implement control of the machine practically. Moreover, it is also important to model the machine and test the control principles using simulation software.

Different modelling approaches can be used depending on the control technique desired. For a stationary frame control, modelling of the machine is done in coordinates that are fixed to the stator [25]. If rotor field oriented control is desired, the modelling is done in synchronous reference frame, i.e. a reference frame rotating with the rotor flux. Two modelling approaches can be used in the synchronous frame, namely single synchronous frame modelling and double synchronous frame modelling. These approaches lead to two types of control techniques [24]. These techniques are discussed in chapter 4.

The following assumptions are taken into account in the machine modelling [7], [24]:

- The stator windings give a sinusoidally distributed magnetic field around the air-gap of the machine, i.e. only the fundamental component of the field is modelled.
- The stator windings are all equal, but have different directions of winding axes.

- Resistances and inductances are assumed to be independent of temperature and frequency.
- Magnetic saturation, hysteresis and eddy currents are not considered.
- The rotor cage is equivalent to a wound rotor.

2.2 Modelling in Single Synchronous Reference Frame

This modelling approach is based on the vector space decomposition technique introduced in [21], which transforms the stator and rotor quantities into a single six-phase stationary frame. To transform these quantities into a common six-phase rotating frame, a modified transformation based on [7] and [8] is used.

Initially the equations of the machine are established by modelling the physical system. Then appropriate transformation and per unit system is used to obtain the per unit model of the machine in synchronous reference frame.

2.2.1 Physical Modelling

For simpler analysis, the squirrel cage rotor can be replaced by equivalent windings [24]. Thus the rotor cage is taken as equivalent to a six-phase wound rotor as shown in Figure 2.2.

In this modelling approach twelve voltage and flux linkage equations can be obtained, six in the stator and six in the rotor. The voltage and flux linkage equations are given compactly in matrix form as

$$\underline{U}^{SR} = \mathbf{R}^{SR} \cdot \underline{I}^{SR} + \frac{d\underline{\Psi}^{SR}}{dt} \tag{2.1}$$

$$\underline{\Psi}^{SR} = \mathbf{L}^{SR} \cdot \underline{I}^{SR} \tag{2.2}$$

These equations describe the electromagnetic system in the machine. The vectors and matrices in the equations contain stator and rotor quantities in their original frames of reference, i.e. stator quantities in stator frame and rotor quantities in rotor frame. The voltage, current and flux linkage vectors are

$$\begin{aligned}
\underline{U}^{SR} &= \left[\mathrm{U_{sa1}} \quad \mathrm{U_{sa2}} \quad \mathrm{U_{sb1}} \quad \mathrm{U_{sb2}} \quad \mathrm{U_{sc1}} \quad \mathrm{U_{sc2}} \quad \mathrm{U_{ra1}} \quad \mathrm{U_{ra2}} \quad \mathrm{U_{rb1}} \quad \mathrm{U_{rb2}} \quad \mathrm{U_{rc1}} \quad \mathrm{U_{rc2}}\right]^{\mathrm{T}} \\
\underline{I}^{SR} &= \left[\mathrm{I_{sa1}} \quad \mathrm{I_{sa2}} \quad \mathrm{I_{sb1}} \quad \mathrm{I_{sb2}} \quad \mathrm{I_{sc1}} \quad \mathrm{I_{sc2}} \quad \mathrm{I_{ra1}} \quad \mathrm{I_{ra2}} \quad \mathrm{I_{rb1}} \quad \mathrm{I_{rb2}} \quad \mathrm{I_{rc1}} \quad \mathrm{I_{rc2}}\right]^{\mathrm{T}} \\
\underline{\Psi}^{SR} &= \left[\Psi_{\mathrm{sa1}} \quad \Psi_{\mathrm{sa2}} \quad \Psi_{\mathrm{sb1}} \quad \Psi_{\mathrm{sb2}} \quad \Psi_{\mathrm{sc1}} \quad \Psi_{\mathrm{sc2}} \quad \Psi_{\mathrm{ra1}} \quad \Psi_{\mathrm{ra2}} \quad \Psi_{\mathrm{rb1}} \quad \Psi_{\mathrm{rb2}} \quad \Psi_{\mathrm{rc1}} \quad \Psi_{\mathrm{rc2}}\right]^{\mathrm{T}}
\end{aligned} \tag{2.3}$$

The rotor voltages are zero since the rotor is short circuited, but are shown in their respective symbols for completeness.

The resistances of the physical model are given by the following diagonal matrix:

$$\mathbf{R}^S = diag\left[\mathrm{R_s} \quad \mathrm{R_s} \quad \mathrm{R_s} \quad \mathrm{R_s} \quad \mathrm{R_s} \quad \mathrm{R_s} \quad \mathrm{R_r} \quad \mathrm{R_r} \quad \mathrm{R_r} \quad \mathrm{R_r} \quad \mathrm{R_r} \quad \mathrm{R_r}\right] \tag{2.4}$$

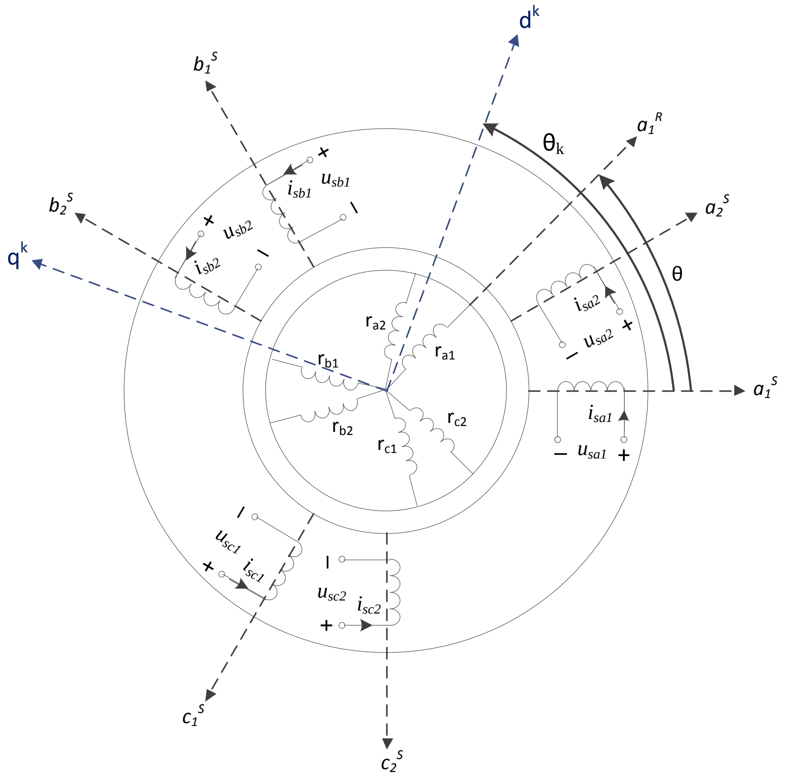

Figure 2.2: Six-phase induction machine with equivalent six-phase wound rotor

The inductance matrix contains the stator self and mutual inductances, rotor self and mutual inductances, and the mutual inductances between the stator and the rotor.

$$\mathbf{L}^{SR} = \begin{bmatrix} \mathbf{L}_{\mathbf{ss}}^S & \mathbf{L}_{sr}^S(\theta) \\ \mathbf{L}_{rs}^R(\theta) & \mathbf{L}_{rr}^R \end{bmatrix} \tag{2.5}$$

where θ is angle of the rotor a_1 axis with respect to the stator a_1 axis as shown in Figure 2.2.

The different sub matrices in the inductance matrix of equation (2.5) are given below. The stator self- and mutual inductances are given in the matrix

$$\mathbf{L}_{\mathbf{ss}}^{S} = \begin{bmatrix} L_{sa1} & L_{sa1sa2} & L_{sa1sb1} & L_{sa1sb2} & L_{sa1sc1} & L_{sa1sc2} \\ L_{sa2sa1} & L_{sa2} & L_{sa2sb1} & L_{sa2sb2} & L_{sa2sc1} & L_{sa2sc2} \\ L_{sb1sa1} & L_{sb1sa2} & L_{sb1} & L_{sb1sb2} & L_{sb1sc1} & L_{sb1sc2} \\ L_{sb2sa1} & L_{sb2sa2} & L_{sb2sb1} & L_{sb2} & L_{sb2sc1} & L_{sb2sc2} \\ L_{sc1sa1} & L_{sc1sa2} & L_{sc1sb1} & L_{sc1sb2} & L_{sc1} & L_{sc1sc2} \\ L_{sc2sa1} & L_{sc2sa2} & L_{sc2sb1} & L_{sc2sb2} & L_{sc2sc1} & L_{sc2} \end{bmatrix} \tag{2.6}$$

The inductances in this matrix are given by

$$\mathbf{L}_{\mathbf{ss}}^{S} = L_{s\sigma} \cdot \mathbf{I_6} + \mathbf{L}_{sh}^{S} \tag{2.7}$$

where $\mathbf{I}_6$ is a 6 × 6 identity matrix, and the $\mathbf{L}_{sh}^{S}$ matrix is

$$\mathbf{L}_{sh}^{S} = L_{sh} \cdot \begin{bmatrix} 1 & \frac{\sqrt{3}}{2} & -\frac{1}{2} & -\frac{\sqrt{3}}{2} & -\frac{1}{2} & 0 \\ \frac{\sqrt{3}}{2} & 1 & 0 & -\frac{1}{2} & -\frac{\sqrt{3}}{2} & -\frac{1}{2} \\ -\frac{1}{2} & 0 & 1 & \frac{\sqrt{3}}{2} & -\frac{1}{2} & -\frac{\sqrt{3}}{2} \\ -\frac{\sqrt{3}}{2} & -\frac{1}{2} & \frac{\sqrt{3}}{2} & 1 & 0 & -\frac{1}{2} \\ -\frac{1}{2} & -\frac{\sqrt{3}}{2} & -\frac{1}{2} & 0 & 1 & \frac{\sqrt{3}}{2} \\ 0 & -\frac{1}{2} & -\frac{\sqrt{3}}{2} & -\frac{1}{2} & \frac{\sqrt{3}}{2} & 1 \end{bmatrix} \tag{2.8}$$

Similarly, the rotor inductances are given as follows:

$$\mathbf{L}_{rr}^{R} = \begin{bmatrix} L_{ra1} & L_{ra1ra2} & L_{ra1rb1} & L_{ra1rb2} & L_{ra1rc1} & L_{ra1rc2} \\ L_{ra2ra1} & L_{ra2} & L_{ra2rb1} & L_{ra2rb2} & L_{ra2rc1} & L_{ra2rc2} \\ L_{rb1ra1} & L_{rb1ra2} & L_{rb1} & L_{rb1rb2} & L_{rb1rc1} & L_{rb1rc2} \\ L_{rb2ra1} & L_{rb2ra2} & L_{rb2rb1} & L_{rb2} & L_{rb2rc1} & L_{rb2rc2} \\ L_{rc1ra1} & L_{rc1ra2} & L_{rc1rb1} & L_{rc1rb2} & L_{rc1} & L_{rc1rc2} \\ L_{rc2ra1} & L_{rc2ra2} & L_{rc2rb1} & L_{rc2rb2} & L_{rc2rc1} & L_{rc2} \end{bmatrix} \tag{2.9}$$

This is given as

$$\mathbf{L}_{rr}^{R} = L_{r\sigma} \cdot \mathbf{I_6} + \mathbf{L}_{rh}^{R} \tag{2.10}$$

where $\mathbf{I}_6$ is a 6 × 6 identity matrix, and the $\mathbf{L}_{rh}^{R}$ matrix is

$$\mathbf{L}_{rh}^{R} = L_{rh} \cdot \begin{bmatrix} 1 & \frac{\sqrt{3}}{2} & -\frac{1}{2} & -\frac{\sqrt{3}}{2} & -\frac{1}{2} & 0 \\ \frac{\sqrt{3}}{2} & 1 & 0 & -\frac{1}{2} & -\frac{\sqrt{3}}{2} & -\frac{1}{2} \\ -\frac{1}{2} & 0 & 1 & \frac{\sqrt{3}}{2} & -\frac{1}{2} & -\frac{\sqrt{3}}{2} \\ -\frac{\sqrt{3}}{2} & -\frac{1}{2} & \frac{\sqrt{3}}{2} & 1 & 0 & -\frac{1}{2} \\ -\frac{1}{2} & -\frac{\sqrt{3}}{2} & -\frac{1}{2} & 0 & 1 & \frac{\sqrt{3}}{2} \\ 0 & -\frac{1}{2} & -\frac{\sqrt{3}}{2} & -\frac{1}{2} & \frac{\sqrt{3}}{2} & 1 \end{bmatrix} \tag{2.11}$$

The mutual inductances between stator and rotor windings are given in the matrices below

$$\mathbf{L}_{sr}^{S}(\theta) = L_h \cdot \begin{bmatrix} \cos\theta & \cos\left(\theta+\frac{\pi}{6}\right) & \cos\left(\theta+\frac{2\pi}{3}\right) & \cos\left(\theta+\frac{5\pi}{6}\right) & \cos\left(\theta+\frac{4\pi}{3}\right) & \cos\left(\theta+\frac{3\pi}{2}\right) \\ \cos\left(\theta-\frac{\pi}{6}\right) & \cos(\theta) & \cos\left(\theta+\frac{\pi}{2}\right) & \cos\left(\theta+\frac{2\pi}{3}\right) & \cos\left(\theta+\frac{7\pi}{6}\right) & \cos\left(\theta+\frac{4\pi}{3}\right) \\ \cos\left(\theta-\frac{2\pi}{3}\right) & \cos\left(\theta-\frac{\pi}{2}\right) & \cos(\theta) & \cos\left(\theta+\frac{\pi}{6}\right) & \cos\left(\theta+\frac{2\pi}{3}\right) & \cos\left(\theta+\frac{5\pi}{6}\right) \\ \cos\left(\theta-\frac{5\pi}{6}\right) & \cos\left(\theta-\frac{2\pi}{3}\right) & \cos\left(\theta-\frac{\pi}{6}\right) & \cos(\theta) & \cos\left(\theta+\frac{\pi}{2}\right) & \cos\left(\theta+\frac{2\pi}{3}\right) \\ \cos\left(\theta-\frac{4\pi}{3}\right) & \cos\left(\theta-\frac{7\pi}{6}\right) & \cos\left(\theta-\frac{2\pi}{3}\right) & \cos\left(\theta-\frac{\pi}{2}\right) & \cos(\theta) & \cos\left(\theta+\frac{\pi}{6}\right) \\ \cos\left(\theta-\frac{3\pi}{2}\right) & \cos\left(\theta-\frac{4\pi}{3}\right) & \cos\left(\theta-\frac{5\pi}{6}\right) & \cos\left(\theta-\frac{2\pi}{3}\right) & \cos\left(\theta-\frac{\pi}{6}\right) & \cos(\theta) \end{bmatrix} \tag{2.12}$$

$$\mathbf{L}_{rs}^{R}(\theta) = \left(\mathbf{L}_{sr}^{S}(\theta)\right)^{\mathrm{T}}$$

The different constant terms used in the inductance matrices are defined as follows:

$L_{s\sigma}$ – Leakage inductance of each stator winding

$L_{r\sigma}$ – Leakage inductance of each rotor winding

L_{sh} – Peak value of the mutual inductance between two stator windings

L_{rh} – Peak value of the mutual inductance between two rotor windings

L_h – Peak value of the mutual inductance between one stator winding and one rotor winding

The electromagnetic torque, linking the electromagnetic and mechanical systems, can be obtained using the co-energy concept as

$$M_e = \frac{1}{2} \cdot \left(\underline{I}^{SR}\right)^T \cdot \frac{\partial \mathbf{L}^{SR}(\theta)}{\partial \theta_{mech}} \cdot \underline{I}^{SR} = \frac{p}{2} \cdot \left(\underline{I}^{SR}\right)^T \cdot \frac{\partial \mathbf{L}^{SR}(\theta)}{\partial \theta} \cdot \underline{I}^{SR} \tag{2.13}$$

The mechanical system is governed by the following equations:

$$J \cdot \frac{d\Omega}{dt} = M_e - M_L \qquad \frac{d\theta_{mech}}{dt} = \Omega \qquad \theta = p \cdot \theta_{mech} \tag{2.14}$$

2.2.2 Transformation of the model

2.2.2.1 Coordinate Transformations

In order to simplify the dynamic control of the machine, a rotor field-oriented coordinate system is used based on the method of rotating vector space decomposition [7]. The original stator and rotor coordinates are transformed to a common rotor field-oriented system composed of three orthogonal subspaces (d, q), (z_1, z_2) and (0_1, 0_2).

The amplitude invariant transformation matrix for the stator quantities is given as follows [7]:

$$\mathbf{T}_{SS}^{k} = \frac{1}{3} \cdot \begin{bmatrix} \cos\theta_k & \cos\left(\theta_k - \frac{\pi}{6}\right) & \cos\left(\theta_k - \frac{2\pi}{3}\right) & \cos\left(\theta_k - \frac{5\pi}{6}\right) & \cos\left(\theta_k - \frac{4\pi}{3}\right) & \cos\left(\theta_k - \frac{3\pi}{2}\right) \\ -\sin\theta_k & -\sin\left(\theta_k - \frac{\pi}{6}\right) & -\sin\left(\theta_k - \frac{2\pi}{3}\right) & -\sin\left(\theta_k - \frac{5\pi}{6}\right) & -\sin\left(\theta_k - \frac{4\pi}{3}\right) & -\sin\left(\theta_k - \frac{3\pi}{2}\right) \\ \cos\theta_k & \cos\left(\theta_k - \frac{7\pi}{6}\right) & \cos\left(\theta_k - \frac{2\pi}{3}\right) & \cos\left(\theta_k - \frac{11\pi}{6}\right) & \cos\left(\theta_k - \frac{4\pi}{3}\right) & \cos\left(\theta_k - \frac{\pi}{2}\right) \\ -\sin(\theta_k - \pi) & -\sin\left(\theta_k - \frac{\pi}{6}\right) & -\sin\left(\theta_k - \frac{5\pi}{3}\right) & -\sin\left(\theta_k - \frac{5\pi}{6}\right) & -\sin\left(\theta_k - \frac{\pi}{3}\right) & -\sin\left(\theta_k - \frac{3\pi}{2}\right) \\ 1 & 0 & 1 & 0 & 1 & 0 \\ 0 & 1 & 0 & 1 & 0 & 1 \end{bmatrix} \tag{2.15}$$

where θ_k is the angle of the synchronously rotating d-axis with respect to the stator a_1 axis as shown in Figure 2.2.

Similarly the transformation matrix for the rotor quantities is

$$\mathbf{T}_{RR}^{k} = \frac{1}{3} \cdot \begin{bmatrix} \cos\theta_r & \cos\left(\theta_r - \frac{\pi}{6}\right) & \cos\left(\theta_r - \frac{2\pi}{3}\right) & \cos\left(\theta_r - \frac{5\pi}{6}\right) & \cos\left(\theta_r - \frac{4\pi}{3}\right) & \cos\left(\theta_r - \frac{3\pi}{2}\right) \\ -\sin\theta_r & -\sin\left(\theta_r - \frac{\pi}{6}\right) & -\sin\left(\theta_r - \frac{2\pi}{3}\right) & -\sin\left(\theta_r - \frac{5\pi}{6}\right) & -\sin\left(\theta_r - \frac{4\pi}{3}\right) & -\sin\left(\theta_r - \frac{3\pi}{2}\right) \\ \cos\theta_r & \cos\left(\theta_r - \frac{7\pi}{6}\right) & \cos\left(\theta_r - \frac{2\pi}{3}\right) & \cos\left(\theta_r - \frac{11\pi}{6}\right) & \cos\left(\theta_r - \frac{4\pi}{3}\right) & \cos\left(\theta_r - \frac{\pi}{2}\right) \\ -\sin(\theta_r - \pi) & -\sin\left(\theta_r - \frac{\pi}{6}\right) & -\sin\left(\theta_r - \frac{5\pi}{3}\right) & -\sin\left(\theta_r - \frac{5\pi}{6}\right) & -\sin\left(\theta_r - \frac{\pi}{3}\right) & -\sin\left(\theta_r - \frac{3\pi}{2}\right) \\ 1 & 0 & 1 & 0 & 1 & 0 \\ 0 & 1 & 0 & 1 & 0 & 1 \end{bmatrix} \tag{2.16}$$

where θ_r is the angle of synchronously rotating d-axis with respect to the rotor a_1 axis. This angle is given by

$$\theta_r = \theta_k - \theta \tag{2.17}$$

The complete transformation matrix from the physical stator and rotor windings to a common rotor field oriented system becomes

$$\mathbf{T}^k = \begin{bmatrix} \mathbf{T}_{SS}^k & \mathbf{0} \\ & \\ \mathbf{0} & \mathbf{T}_{RR}^k \end{bmatrix} \tag{2.18}$$

The transformed model can be obtained by applying this transformation on equations (2.1), (2.2) and (2.13).

$$\begin{aligned} \mathbf{T}^k \cdot \underline{U}^{SR} &= \mathbf{T}^k \cdot \mathbf{R}^{\mathbf{SR}} \cdot \underline{I}^{SR} + \mathbf{T}^k \cdot \frac{d\underline{\Psi}^{SR}}{dt} \\ \underline{U}^k &= \mathbf{T}^k \cdot \mathbf{R}^{\mathbf{SR}} \cdot \mathbf{T}^{-k} \cdot \underline{I}^k + \mathbf{T}^k \cdot \frac{d\left(\mathbf{T}^{-k} \cdot \underline{\Psi}^k\right)}{dt} \\ \underline{U}^k &= \mathbf{R}^k \cdot \underline{I}^k + \frac{d\underline{\Psi}^k}{dt} + \mathbf{T}^k \cdot \frac{d\mathbf{T}^{-k}}{dt} \cdot \underline{\Psi}^k \end{aligned} \tag{2.19}$$

where $\mathbf{T}^{-k}$ is the inverse of the matrix $\mathbf{T}^k$.

By introducing the rotation matrix $\mathbf{J}$, the voltage equation can be written as

$$\underline{U}^k = \mathbf{R}^k \cdot \underline{I}^k + \frac{d\underline{\Psi}^k}{dt} + \omega_x \cdot \mathbf{J} \cdot \underline{\Psi}^k \tag{2.20}$$

where $\frac{d\theta_x}{dt} = \omega_x$, $\mathbf{J} = \mathbf{T}_{ss}^{-r} \cdot \frac{d\mathbf{T}_{ss}^{-r}}{d\theta_x}$ and x can be k or r, for stator or rotor quantity.

The vectors and matrices in the transformed voltage equation are

$$\begin{aligned} \underline{U}^k &= \left[\mathrm{U_{sd}} \quad \mathrm{U_{sq}} \quad \mathrm{U_{sz_1}} \quad \mathrm{U_{sz_2}} \quad \mathrm{U_{s0_1}} \quad \mathrm{U_{s0_2}} \quad \mathrm{U_{rd}} \quad \mathrm{U_{rq}} \quad \mathrm{U_{rz_1}} \quad \mathrm{U_{rz_2}} \quad \mathrm{U_{r0_1}} \quad \mathrm{U_{r0_2}}\right]^{\mathrm{T}} \\ \underline{I}^k &= \left[\mathrm{I_{sd}} \quad \mathrm{I_{sq}} \quad \mathrm{I_{sz_1}} \quad \mathrm{I_{sz_2}} \quad \mathrm{I_{s0_1}} \quad \mathrm{I_{s0_2}} \quad \mathrm{I_{rd}} \quad \mathrm{I_{rq}} \quad \mathrm{I_{rz_1}} \quad \mathrm{I_{rz_2}} \quad \mathrm{I_{r0_1}} \quad \mathrm{I_{r0_2}}\right]^{\mathrm{T}} \\ \underline{\Psi}^k &= \left[\Psi_{\mathrm{sd}} \quad \Psi_{\mathrm{sq}} \quad \Psi_{\mathrm{sz_1}} \quad \Psi_{\mathrm{sz_2}} \quad \Psi_{\mathrm{s0_1}} \quad \Psi_{\mathrm{s0_2}} \quad \Psi_{\mathrm{rd}} \quad \Psi_{\mathrm{rq}} \quad \Psi_{\mathrm{rz_1}} \quad \Psi_{\mathrm{rz_2}} \quad \Psi_{\mathrm{r0_1}} \quad \Psi_{\mathrm{r0_2}}\right]^{\mathrm{T}} \\ \mathbf{R}^k &= diag\left[\mathrm{R_s} \quad \mathrm{R_s} \quad \mathrm{R_s} \quad \mathrm{R_s} \quad \mathrm{R_s} \quad \mathrm{R_s} \quad \mathrm{R_r} \quad \mathrm{R_r} \quad \mathrm{R_r} \quad \mathrm{R_r} \quad \mathrm{R_r} \quad \mathrm{R_r}\right] \end{aligned} \tag{2.21}$$

The rotation matrix is obtained as

$$\mathbf{J} = \begin{bmatrix} 0 & -1 & 0 & 0 & 0 & 0 & 0 & 0 & 0 \\ 1 & 0 & 0 & 0 & 0 & 0 & 0 & 0 & 0 \\ 0 & 0 & 0 & 0 & 0 & 0 & 0 & 0 & 0 \\ 0 & 0 & 0 & 0 & -1 & 0 & 0 & 0 & 0 \\ 0 & 0 & 0 & 1 & 0 & 0 & 0 & 0 & 0 \\ 0 & 0 & 0 & 0 & 0 & 0 & 0 & 0 & 0 \\ 0 & 0 & 0 & 0 & 0 & 0 & 0 & -1 & 0 \\ 0 & 0 & 0 & 0 & 0 & 0 & 1 & 0 & 0 \\ 0 & 0 & 0 & 0 & 0 & 0 & 0 & 0 & 0 \end{bmatrix} \tag{2.22}$$

The flux linkage equations are transformed as

$$\begin{aligned} &\mathbf{T}^{k} \cdot \underline{\Psi}^{SR} = \mathbf{T}^{k} \cdot \mathbf{L}^{SR} \cdot \underline{I}^{SR} \\ &\underline{\Psi}^{k} = \mathbf{T}^{k} \cdot \mathbf{L}^{SR} \cdot \mathbf{T}^{-k} \cdot \underline{I}^{k} \\ &\underline{\Psi}^{k} = \mathbf{L}^{k} \cdot \underline{I}^{k} \end{aligned} \tag{2.23}$$

The transformed inductance matrix is obtained as follows:

$$\mathbf{L}^{k} = \begin{bmatrix} L_s & 0 & 0 & 0 & 0 & 0 & L_h & 0 & 0 & 0 & 0 & 0 \\ 0 & L_s & 0 & 0 & 0 & 0 & 0 & L_h & 0 & 0 & 0 & 0 \\ 0 & 0 & L_{s\sigma} & 0 & 0 & 0 & 0 & 0 & 0 & 0 & 0 & 0 \\ 0 & 0 & 0 & L_{s\sigma} & 0 & 0 & 0 & 0 & 0 & 0 & 0 & 0 \\ 0 & 0 & 0 & 0 & L_{s\sigma} & 0 & 0 & 0 & 0 & 0 & 0 & 0 \\ 0 & 0 & 0 & 0 & 0 & L_{s\sigma} & 0 & 0 & 0 & 0 & 0 & 0 \\ L_h & 0 & 0 & 0 & 0 & 0 & L_r & 0 & 0 & 0 & 0 & 0 \\ 0 & L_h & 0 & 0 & 0 & 0 & 0 & L_r & 0 & 0 & 0 & 0 \\ 0 & 0 & 0 & 0 & 0 & 0 & 0 & 0 & L_{r\sigma} & 0 & 0 & 0 \\ 0 & 0 & 0 & 0 & 0 & 0 & 0 & 0 & 0 & L_{r\sigma} & 0 & 0 \\ 0 & 0 & 0 & 0 & 0 & 0 & 0 & 0 & 0 & 0 & L_{r\sigma} & 0 \\ 0 & 0 & 0 & 0 & 0 & 0 & 0 & 0 & 0 & 0 & 0 & L_{r\sigma} \end{bmatrix} \tag{2.24}$$

where $L_s = L_{s\sigma} + 3 \cdot L_{sh}$ $\quad L_r = L_{r\sigma} + 3 \cdot L_{rh}$ $\quad L_h = 3 \cdot L_{srh}$

Transformation of the electromagnetic torque equation is given as

$$\begin{aligned} &M_e = \frac{p}{2} \cdot \left(\underline{I}^{SR}\right)^{\mathrm{T}} \cdot \frac{\partial \mathbf{L}^{\mathbf{SR}}}{\partial \theta} \cdot \underline{I}^{SR} \\ &M_e = \frac{p}{2} \cdot \left(\mathbf{T}^{-k} \cdot \underline{I}^{k}\right)^{\mathrm{T}} \cdot \frac{\partial \mathbf{L}^{\mathbf{SR}}}{\partial \theta} \cdot \mathbf{T}^{-k} \cdot \underline{I}^{kr} \\ &M_e = \frac{p}{2} \cdot \left(\underline{I}^{k}\right)^{\mathrm{T}} \cdot \left(\mathbf{T}^{-k}\right)^{\mathrm{T}} \cdot \frac{\partial \mathbf{L}^{\mathbf{SR}}}{\partial \theta} \cdot \mathbf{T}^{-k} \cdot \underline{I}^{k} \end{aligned} \tag{2.25}$$

The torque equation in transformed equations is obtained as:

$$M_e = 3 \cdot p \cdot L_h \cdot \left(I_{sq} \cdot I_{rd} - I_{sd} \cdot I_{rq} \right) \tag{2.26}$$

Using the transformed flux linkage equations from (2.23), the torque can be written as

$$M_e = 3 \cdot p \cdot \left(\Psi_{rq} \cdot I_{rd} - \Psi_{rd} \cdot I_{rq} \right) \tag{2.27}$$

2.2.2.2 Per Unit System

The basis for power in an AC machine is usually taken as the total power into the stator winding in steady state. By averaging the power in each winding over one fundamental period, the rated input power can be written as [7]

$$\mathrm{P_{sN}} = 6 \cdot \frac{\hat{U}_{phN} \cdot \hat{I}_{phN}}{2} \cdot \cos\varphi_N = 6 \cdot U_{phN,rms} \cdot I_{phN,rms} \cdot \cos\varphi_N \tag{2.28}$$

The rated apparent power, which is used as basis for power in the machine, is

$$\mathrm{S_N} = 6 \cdot \frac{\hat{U}_{phN} \cdot \hat{I}_{phN}}{2} = 3 \cdot \hat{U}_{phN} \cdot \hat{I}_{phN} = 6 \cdot U_{phN,rms} \cdot I_{phN,rms} = 2 \cdot \sqrt{3} \cdot U_N \cdot I_N \tag{2.29}$$

where U_N is the rms value of the line-to-line voltage in one of the two three-phase groups, and I_N is the rms value of the current in one winding, i.e. the phase current.

The rated per phase peak values are used as basis values in the stator windings. Thus the basis values for current, voltage, impedance and flux in transformed coordinates are

$$\begin{aligned}
&\mathrm{I_{sdn}} = \mathrm{I_{sqn}} = \mathrm{I_{sz1n}} = \mathrm{I_{sz2n}} = \mathrm{I_{s01n}} = \mathrm{I_{s02n}} = \hat{I}_N \\
&\mathrm{U_{sdn}} = \mathrm{U_{sqn}} = \mathrm{U_{sz1n}} = \mathrm{U_{sz2n}} = \mathrm{U_{s01n}} = \mathrm{U_{s02n}} = \hat{U}_{ph,N} \\
&\mathrm{Z_{sdn}} = \mathrm{Z_{sqn}} = \mathrm{Z_{sz1n}} = \mathrm{Z_{sz2n}} = \mathrm{Z_{s01n}} = \mathrm{Z_{s02n}} = \frac{\hat{U}_{ph,N}}{\hat{I}_N} \\
&\Psi_{\mathrm{sdn}} = \Psi_{\mathrm{sqn}} = \Psi_{\mathrm{sz1n}} = \Psi_{\mathrm{sz2n}} = \Psi_{\mathrm{s01n}} = \Psi_{\mathrm{s02n}} = \Psi_{\mathrm{n}} = \frac{\hat{U}_{ph,N}}{\omega_n} = \frac{\hat{U}_{ph,N}}{2 \cdot \pi \cdot f_n}
\end{aligned} \tag{2.30}$$

The basis values for the rotor quantities are the same as the corresponding stator basis values.

The basis for torque is

$$M_n = \frac{S_N}{\Omega_N} = p \cdot \frac{S_N}{\omega_n} = 3 \cdot p \cdot \frac{\hat{U}_{phN} \cdot \hat{I}_{phN}}{\omega_n} = 3 \cdot p \cdot \hat{\Psi}_n \cdot \hat{I}_{phN} \tag{2.31}$$

where Ω_N is the rated synchronous speed in mechanical radians per second.

2.2.2.3 The Transformed per unit model

The transformed per unit model of the machine is obtained after scaling the transformed equations (2.20), (2.23) and (2.27) by the basis values of the aforementioned per unit system.

The voltage equations are obtained as

$$\begin{aligned}
u_{sd} &= r_s \cdot i_{sd} + \frac{1}{\omega_n} \cdot \frac{d\psi_{sd}}{dt} - f_k \cdot \psi_{sq} & u_{sq} &= r_s \cdot i_{sq} + \frac{1}{\omega_n} \cdot \frac{d\psi_{sq}}{dt} + f_k \cdot \psi_{sd} \\
u_{sz1} &= r_s \cdot i_{sz1} + \frac{1}{\omega_n} \cdot \frac{d\psi_{sz1}}{dt} + f_k \cdot \psi_{sz2} & u_{sz2} &= r_s \cdot i_{sz2} + \frac{1}{\omega_n} \cdot \frac{d\psi_{sz2}}{dt} - f_k \cdot \psi_{sz1} \\
u_{s01} &= r_s \cdot i_{s01} + \frac{1}{\omega_n} \cdot \frac{d\psi_{s01}}{dt} & u_{s02} &= r_s \cdot i_{s02} + \frac{1}{\omega_n} \cdot \frac{d\psi_{s02}}{dt} \\
0 &= r_r \cdot i_{rd} + \frac{1}{\omega_n} \cdot \frac{d\psi_{rd}}{dt} - f_r \, \psi_{rq} & 0 &= r_r \cdot i_{rq} + \frac{1}{\omega_n} \cdot \frac{d\psi_{rq}}{dt} + f_r \, \psi_{rd}
\end{aligned} \tag{2.32}$$

The flux linkages are

$$\begin{aligned}
\psi_{sd} &= x_s \cdot i_{sd} + x_h \cdot i_{rd} & \psi_{sq} &= x_s \cdot i_{sq} + x_h \cdot i_{rq} \\
\psi_{sz1} &= x_{s\sigma} \cdot i_{sz1} & \psi_{sz2} &= x_{s\sigma} \cdot i_{sz2} \\
\psi_{s01} &= x_{s\sigma} \cdot i_{s01} & \psi_{s02} &= x_{s\sigma} \cdot i_{s02} \\
\psi_{rd} &= x_r \cdot i_{rd} + x_h \cdot i_{sd} & \psi_{rq} &= x_r \cdot i_{rq} + x_h \cdot i_{sq} \\
x_s &= x_h + x_{s\sigma} & x_r &= x_h + x_{r\sigma}
\end{aligned} \tag{2.33}$$

The mechanical system equations in per unit become

$$\begin{aligned}
& m_e = \psi_{rq} \cdot i_{rd} - \psi_{rd} \cdot i_{rq} \\
& T_m \cdot \frac{dn}{dt} = m_e - m_L & & T_m = \frac{J \cdot \Omega_N^2}{S_N} \\
& \frac{d\theta}{dt} = \omega_n \cdot n & & \theta_{\text{mech}} = \frac{\theta}{p} \\
& f_r = f_k - n & & f_k = \frac{\omega_k}{\omega_n} \qquad f_r = \frac{\omega_r}{\omega_n}
\end{aligned} \tag{2.34}$$

Since there is no excitation of the (z_1, z_2) and (0_1, 0_2) subspaces in the rotor circuit, the corresponding equations have been left out of the model. The rotor voltages are zero as mentioned earlier. Considering that the two stator three phase groups have isolated neutrals, there is no excitation of the (0_1, 0_2) in the stator. Therefore, it can be omitted from modelling. However, the stator (z_1, z_2) system can be excited due to current or supply asymmetries between the two phase groups; hence, it is included in the model.

From the voltage and flux linkage equations in (2.32) and (2.33), the per unit equivalent circuit of the machine in single synchronous frame is given in Figure 2.3.

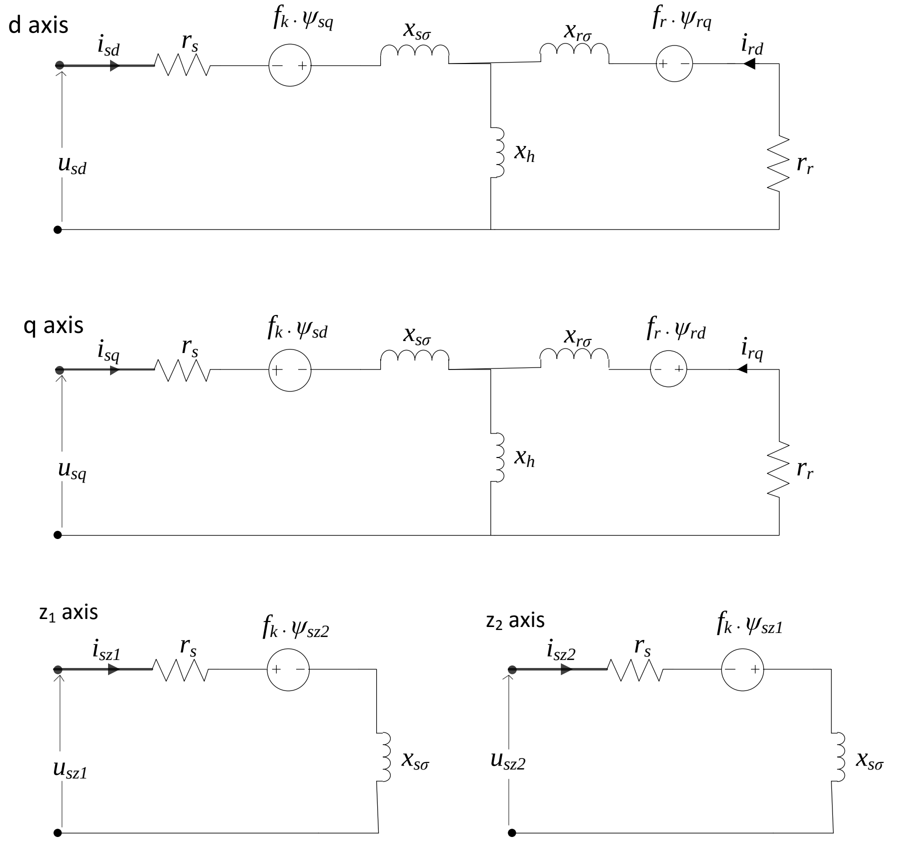

Figure 2.3: Per unit equivalent circuit of SPIM in single synchronous frame

2.3 Modelling in Double Synchronous Reference Frame

The six-phase induction machine can also be modelled in double synchronous reference frame as an alternative to the single synchronous modelling presented earlier as demonstrated in [24]. This approach is based on the modelling principle of three-phase machines. In the following sections, model of the physical system is established first. Then a transformed per unit model is derived. Finally the equivalent circuit of the machine based on this modelling approach is presented. The physical modelling of the stator and the transformations are based on the work in [8].

2.3.1 Physical Modelling

The two stator three-phase groups are taken as separate ones, but the mutual impedance between the two is considered in the inductance matrix. Each 3-phase group is transformed to a synchronously rotating *d-q-0* coordinate system. The squirrel cage rotor is modeled as an equivalent three phase wound rotor as shown in Figure 2.4.

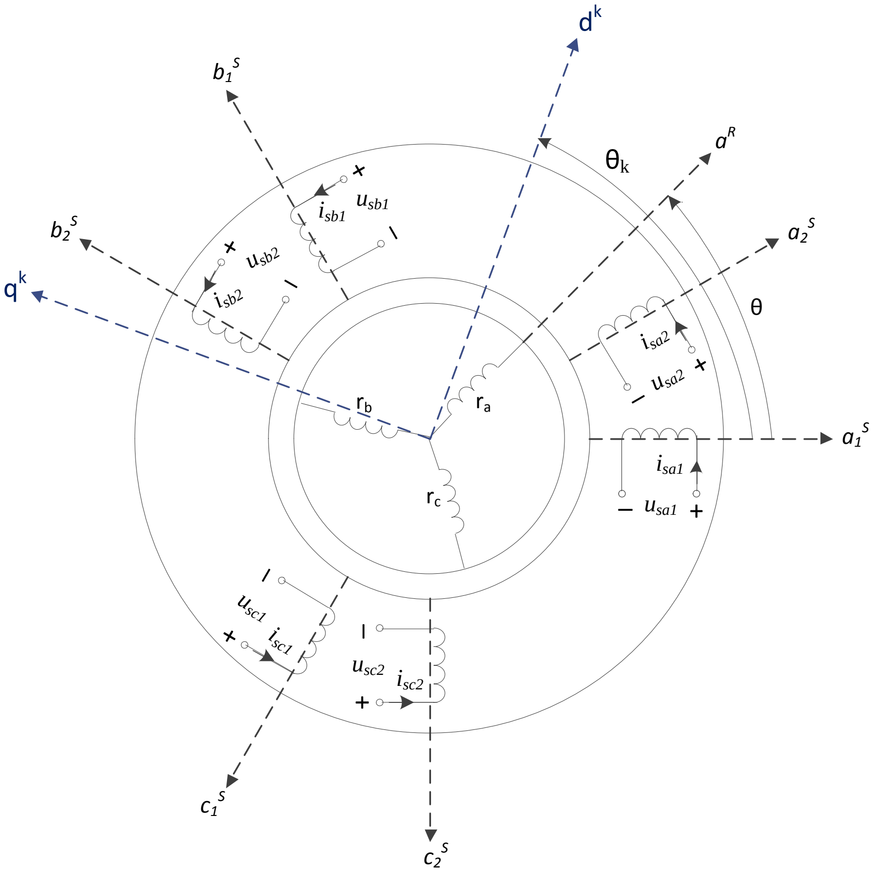

Figure 2.4: Six-phase induction machine with equivalent three-phase wound rotor

The voltage and flux linkage equations of the stator and rotor can be written in matrix form as

$$\underline{U}^{SR} = \mathbf{R}^{SR} \cdot \underline{I}^{SR} + \frac{d\underline{\Psi}^{SR}}{dt} \tag{2.35}$$

$$\underline{\Psi}^{SR} = \mathbf{L}^{SR} \cdot \underline{I}^{SR} \tag{2.36}$$

The voltage, current and flux linkage vectors are

$$\begin{aligned} \underline{U}^{SR} &= \begin{bmatrix} \mathrm{U_{sa1}} & \mathrm{U_{sb1}} & \mathrm{U_{sc1}} & \mathrm{U_{sa2}} & \mathrm{U_{sb2}} & \mathrm{U_{sc2}} & \mathrm{U_{rd}} & \mathrm{U_{rq}} & \mathrm{U_{r0}} \end{bmatrix}^{\mathrm{T}} \\ \underline{I}^{SR} &= \begin{bmatrix} \mathrm{I_{sa1}} & \mathrm{I_{sb1}} & \mathrm{I_{sc1}} & \mathrm{I_{sa2}} & \mathrm{I_{sb2}} & \mathrm{I_{sc2}} & \mathrm{I_{ra}} & \mathrm{I_{rb}} & \mathrm{I_{rc}} \end{bmatrix}^{\mathrm{T}} \\ \underline{\Psi}^{SR} &= \begin{bmatrix} \Psi_{\mathrm{sa1}} & \Psi_{\mathrm{sb1}} & \Psi_{\mathrm{sc1}} & \Psi_{\mathrm{sa2}} & \Psi_{\mathrm{sb2}} & \Psi_{\mathrm{sc2}} & \Psi_{\mathrm{ra}} & \Psi_{\mathrm{rb}} & \Psi_{\mathrm{rc}} \end{bmatrix}^{\mathrm{T}} \end{aligned} \tag{2.37}$$

The resistance matrix of the physical model is

$$\mathbf{R}^{SR} = diag\begin{bmatrix} \mathrm{R_s} & \mathrm{R_s} & \mathrm{R_s} & \mathrm{R_s} & \mathrm{R_s} & \mathrm{R_s} & \mathrm{R_r} & \mathrm{R_r} & \mathrm{R_r} \end{bmatrix} \tag{2.38}$$

The inductance matrix of the physical model is given as follows:

$$\mathbf{L}^{SR} = \begin{bmatrix} \mathbf{L}_{\mathbf{ss}}^{S} & \mathbf{L}_{sr}^{S}(\theta) \\ \mathbf{L}_{rs}^{R}(\theta) & \mathbf{L}_{rr}^{R} \end{bmatrix} \tag{2.39}$$

The sub-matrix of stator self and mutual inductances is

$$\mathbf{L}_{\mathbf{ss}}^{S} = \begin{bmatrix} L_{sa1} & L_{sa1sb1} & L_{sa1sc1} & L_{sa1sa2} & L_{sa1sb2} & L_{sa1sc2} \\ L_{sb1sa1} & L_{sb1} & L_{sb1sc1} & L_{sb1sa2} & L_{sb1sb2} & L_{sb1sc2} \\ L_{sc1sa1} & L_{sc1sb1} & L_{sc1} & L_{sc1sa2} & L_{sc1sb2} & L_{sc1sc2} \\ L_{sa2sa1} & L_{sa2sb1} & L_{sa2sc1} & L_{sa2} & L_{sa2sb2} & L_{sa2sc2} \\ L_{sb2sa1} & L_{sb2sb1} & L_{sb2sc1} & L_{sb2sa2} & L_{sb2} & L_{sb2sc2} \\ L_{sc2sa1} & L_{sc2sb1} & L_{sc2sc1} & L_{sc2sa2} & L_{sc2sb2} & L_{sc2} \end{bmatrix} \tag{2.40}$$

The values of the inductances in this matrix are given by

$$\mathbf{L}_{\mathbf{ss}}^{S} = L_{s\sigma} \cdot \mathbf{I_6} + \mathbf{L}_{sh}^{S} \tag{2.41}$$

where $\mathbf{I}_6$ is a 6 × 6 identity matrix and

$$\mathbf{L}_{sh}^{S} = L_{sh} \cdot \begin{bmatrix} 1 & -\frac{1}{2} & -\frac{1}{2} & \frac{\sqrt{3}}{2} & -\frac{\sqrt{3}}{2} & 0 \\ -\frac{1}{2} & 1 & -\frac{1}{2} & 0 & \frac{\sqrt{3}}{2} & -\frac{\sqrt{3}}{2} \\ -\frac{1}{2} & -\frac{1}{2} & 1 & -\frac{\sqrt{3}}{2} & 0 & \frac{\sqrt{3}}{2} \\ \frac{\sqrt{3}}{2} & 0 & -\frac{\sqrt{3}}{2} & 1 & -\frac{1}{2} & -\frac{1}{2} \\ -\frac{\sqrt{3}}{2} & \frac{\sqrt{3}}{2} & 0 & -\frac{1}{2} & 1 & -\frac{1}{2} \\ 0 & -\frac{\sqrt{3}}{2} & \frac{\sqrt{3}}{2} & -\frac{1}{2} & -\frac{1}{2} & 1 \end{bmatrix} \tag{2.42}$$

The sub-matrix of rotor self and mutual inductances is

$$\mathbf{L}_{rr}^{R} = \begin{bmatrix} L_{ra} & L_{rarb} & L_{rarc} \\ L_{rbra} & L_{rb} & L_{rbrc} \\ L_{rcra} & L_{rcrb} & L_{rc} \end{bmatrix} \tag{2.43}$$

The values of the rotor inductances are given by

$$\mathbf{L}_{rr}^{R} = L_{r\sigma} \cdot \mathbf{I}_3 + \mathbf{L}_{rh}^{R} \tag{2.44}$$

where $\mathbf{I}_3$ is a 3 × 3 identity matrix and

$$\mathbf{L}_{rh}^{R} = L_{rh} \cdot \begin{bmatrix} 1 & -\frac{1}{2} & -\frac{1}{2} \\ -\frac{1}{2} & 1 & -\frac{1}{2} \\ -\frac{1}{2} & -\frac{1}{2} & 1 \end{bmatrix} \tag{2.45}$$

The mutual inductance sub-matrices between stator and rotor are

$$\mathbf{L}_{\mathbf{sr}}^{S}(\theta) = \begin{bmatrix} L_{sa1ra} & L_{sa1rb} & L_{sa1rc} \\ L_{sb1ra} & L_{sb1rb} & L_{sb1rc} \\ L_{sc1ra} & L_{sc1rb} & L_{sc1rc} \\ L_{sa2ra} & L_{sa2rb} & L_{sa2rc} \\ L_{sb2ra} & L_{sb2rb} & L_{sb2rc} \\ L_{sc2ra} & L_{sc2rb} & L_{sc2rc} \end{bmatrix}$$

$$\mathbf{L}_{rs}^{R}(\theta) = \left(\mathbf{L}_{\mathbf{sr}}^{S}(\theta)\right)^{T} \tag{2.46}$$

where the values of each inductance are given in the following matrices

$$\mathbf{L}_{sr}^{S}(\theta) = L_{srh} \cdot \begin{bmatrix} \cos\theta & \cos\left(\theta + \frac{2\pi}{3}\right) & \cos\left(\theta + \frac{4\pi}{3}\right) \\ \cos\left(\theta - \frac{2\pi}{3}\right) & \cos(\theta) & \cos\left(\theta + \frac{2\pi}{3}\right) \\ \cos\left(\theta - \frac{4\pi}{3}\right) & \cos\left(\theta - \frac{2\pi}{3}\right) & \cos(\theta) \\ \cos\left(\theta - \frac{\pi}{6}\right) & \cos\left(\theta + \frac{\pi}{2}\right) & \cos\left(\theta + \frac{7\pi}{6}\right) \\ \cos\left(\theta - \frac{5\pi}{6}\right) & \cos\left(\theta - \frac{\pi}{6}\right) & \cos\left(\theta - \frac{2\pi}{3}\right) \\ \cos\left(\theta - \frac{3\pi}{2}\right) & \cos\left(\theta - \frac{5\pi}{6}\right) & \cos\left(\theta - \frac{\pi}{6}\right) \end{bmatrix}$$

$$\mathbf{L}_{rs}^{R}(\theta) = \left(\mathbf{L}_{sr}^{S}(\theta)\right)^{\mathrm{T}} \tag{2.47}$$

The different terms in the inductance matrices are defined as

$L_{s\sigma}$ – Leakage inductance of each stator winding

$L_{r\sigma}$ – Leakage inductance of each rotor winding

L_{sh} – Peak value of the mutual inductance between two stator windings

L_{rh} – Peak value of the mutual inductance between two rotor windings

L_{srh} – Peak value of the mutual inductance between one stator winding and one rotor winding

θ – Position of the rotor with respect to the stator a_1 axis

The equations describing the mechanical system are:

$$M_e = \frac{1}{2} \cdot \left(\underline{I}^S\right)^T \cdot \frac{\partial \mathbf{L}_{\mathbf{ss}}^S(\theta)}{\partial \theta_{mech}} \cdot \underline{I}^S = \frac{p}{2} \cdot \left(\underline{I}^S\right)^T \cdot \frac{\partial \mathbf{L}_{\mathbf{ss}}^S(\theta)}{\partial \theta} \cdot \underline{I}^S \tag{2.48}$$

$$J \cdot \frac{d\Omega}{dt} = M_e - M_L \qquad \frac{d\theta_{mech}}{dt} = \Omega \qquad \theta = p \cdot \theta_{mech} \tag{2.49}$$

2.3.2 The Transformed Per Unit Model

2.3.2.1 Coordinate Transformations

A double synchronous transformation is used to transform the stator (a_1, b_1, c1) and (a_2, b_2, c_2) quantities into (d_1, q_1, 0_1) and (d_2, q_2, 0_2) coordinate systems respectively. Both (d_1, q_1, 0_1) and (d_2, q_2, 0_2) systems coincide. The amplitude invariant transformation matrix for the stator quantities is given as

$$\mathbf{T}_{ss}^k = \frac{2}{3} \cdot \begin{bmatrix} \cos\theta_k & \cos\left(\theta_k - \frac{2\pi}{3}\right) & \cos\left(\theta_k - \frac{4\pi}{3}\right) & 0 & 0 & 0 \\ -\sin\theta_k & -\sin\left(\theta_k - \frac{2\pi}{3}\right) & -\sin\left(\theta_k - \frac{4\pi}{3}\right) & 0 & 0 & 0 \\ \frac{1}{2} & \frac{1}{2} & \frac{1}{2} & 0 & 0 & 0 \\ 0 & 0 & 0 & \cos\left(\theta_k - \frac{\pi}{6}\right) & \cos\left(\theta_k - \frac{5\pi}{6}\right) & \cos\left(\theta_k - \frac{3\pi}{2}\right) \\ 0 & 0 & 0 & -\sin\left(\theta_k - \frac{\pi}{6}\right) & -\sin\left(\theta_k - \frac{5\pi}{6}\right) & -\sin\left(\theta_k - \frac{3\pi}{2}\right) \\ 0 & 0 & 0 & \frac{1}{2} & \frac{1}{2} & \frac{1}{2} \end{bmatrix} \tag{2.50}$$

where θ_k is the angle of the synchronously rotating d-axes (d_1 and d_2) with respect to the stator a_1 axis.

The rotor (a, b, c) quantities are transformed into a synchronously rotating (d, q, 0) coordinate system, which coincides with (d_1, q_1, 0_1) and (d_2, q_2, 0_2). The transformation matrix for the rotor quantities is

$$\mathbf{T}_{RR}^k = \frac{2}{3} \cdot \begin{bmatrix} \cos\theta_r & \cos\left(\theta_r - \frac{2\pi}{3}\right) & \cos\left(\theta_r - \frac{4\pi}{3}\right) \\ -\sin\theta_r & -\sin\left(\theta_r - \frac{2\pi}{3}\right) & -\sin\left(\theta_r - \frac{4\pi}{3}\right) \\ \frac{1}{2} & \frac{1}{2} & \frac{1}{2} \end{bmatrix} \tag{2.51}$$

where θ_r is the angle of the synchronously rotating d-axis with respect to the rotor a-axis. It is given by

$$\theta_r = \theta_k - \theta \tag{2.52}$$

The complete transformation matrix from the physical stator and rotor windings to a common rotor field oriented coordinate system becomes

$$\mathbf{T}^k = \begin{bmatrix} \mathbf{T}_{SS}^k & \mathbf{0} \\ \mathbf{0} & \mathbf{T}_{RR}^k \end{bmatrix} \tag{2.53}$$

Therefore, the complete transformation matrix is

$$\mathbf{T}^k = \frac{2}{3} \cdot \begin{bmatrix} \cos\theta_k & \cos\left(\theta_k - \frac{2\pi}{3}\right) & \cos\left(\theta_k - \frac{4\pi}{3}\right) & 0 & 0 & 0 & 0 & 0 & 0 \\ -\sin\theta_k & -\sin\left(\theta_k - \frac{2\pi}{3}\right) & -\sin\left(\theta_k - \frac{4\pi}{3}\right) & 0 & 0 & 0 & 0 & 0 & 0 \\ \frac{1}{2} & \frac{1}{2} & \frac{1}{2} & 0 & 0 & 0 & 0 & 0 & 0 \\ 0 & 0 & 0 & \cos\left(\theta_k - \frac{\pi}{6}\right) & \cos\left(\theta_k - \frac{5\pi}{6}\right) & \cos\left(\theta_k - \frac{3\pi}{2}\right) & 0 & 0 & 0 \\ 0 & 0 & 0 & -\sin\left(\theta_k - \frac{\pi}{6}\right) & -\sin\left(\theta_k - \frac{5\pi}{6}\right) & -\sin\left(\theta_k - \frac{3\pi}{2}\right) & 0 & 0 & 0 \\ 0 & 0 & 0 & \frac{1}{2} & \frac{1}{2} & \frac{1}{2} & 0 & 0 & 0 \\ 0 & 0 & 0 & 0 & 0 & 0 & \cos\theta_r & \cos\left(\theta_r - \frac{2\pi}{3}\right) & \cos\left(\theta_r - \frac{4\pi}{3}\right) \\ 0 & 0 & 0 & 0 & 0 & 0 & -\sin\theta_r & -\sin\left(\theta_r - \frac{2\pi}{3}\right) & -\sin\left(\theta_r - \frac{4\pi}{3}\right) \\ 0 & 0 & 0 & 0 & 0 & 0 & \frac{1}{2} & \frac{1}{2} & \frac{1}{2} \end{bmatrix} \tag{2.54}$$

The inverse of the transformation matrix is

$$\mathbf{T}^{-k} = \begin{bmatrix} \cos\theta_k & -\sin\theta_k & 1 & 0 & 0 & 0 & 0 & 0 & 0 \\ \sin\left(\theta_k - \frac{\pi}{6}\right) & \cos\left(\theta_k - \frac{\pi}{6}\right) & 1 & 0 & 0 & 0 & 0 & 0 & 0 \\ -\sin\left(\theta_k + \frac{\pi}{6}\right) & -\cos\left(\theta_k + \frac{\pi}{6}\right) & 1 & 0 & 0 & 0 & 0 & 0 & 0 \\ 0 & 0 & 0 & \cos\left(\theta_k - \frac{\pi}{6}\right) & -\sin\left(\theta_k - \frac{\pi}{6}\right) & 1 & 0 & 0 & 0 \\ 0 & 0 & 0 & -\cos\left(\theta_k + \frac{\pi}{6}\right) & \sin\left(\theta_k + \frac{\pi}{6}\right) & 1 & 0 & 0 & 0 \\ 0 & 0 & 0 & -\sin\theta_k & -\cos\theta_k & 1 & 0 & 0 & 0 \\ 0 & 0 & 0 & 0 & 0 & 0 & \cos\theta_r & -\sin\theta_r & 1 \\ 0 & 0 & 0 & 0 & 0 & 0 & \sin\left(\theta_r - \frac{\pi}{6}\right) & \cos\left(\theta_r - \frac{\pi}{6}\right) & 1 \\ 0 & 0 & 0 & 0 & 0 & 0 & -\sin\left(\theta_r + \frac{\pi}{6}\right) & -\cos\left(\theta_r + \frac{\pi}{6}\right) & 1 \end{bmatrix} \tag{2.55}$$

Introducing the transformation and inverse transformation matrices into equation (2.35) gives

$$\underline{U}^k = \mathbf{T}^k \cdot \underline{U}^{SR} = \mathbf{T}^k \cdot \mathbf{R}^{\mathbf{SR}} \cdot \mathbf{T}^{-k} \cdot \underline{I}^k + \mathbf{T}^k \cdot \frac{d\left(\mathbf{T}^{-k} \cdot \underline{\Psi}^k\right)}{dt} = \mathbf{R}^k \cdot \underline{I}^k + \frac{d\underline{\Psi}^k}{dt} + \mathbf{T}^k \cdot \frac{d\mathbf{T}^{-k}}{dt} \cdot \underline{\Psi}^k \tag{2.56}$$

By introducing the matrix $\mathbf{J}$, the voltage equation can be written as

$$\underline{U}^k = \mathbf{R}^k \cdot \underline{I}^k + \frac{d\underline{\Psi}^k}{dt} + \omega_{\mathrm{n}} \cdot f_x \cdot \mathbf{J} \cdot \underline{\Psi}^k$$
$$\text{where} \quad \mathbf{J} = \mathbf{T}^k \cdot \frac{d\mathbf{T}^{-k}}{d\theta_x}, \qquad \frac{d\theta_x}{dt} = \omega_{\mathrm{n}} \cdot f_x \tag{2.57}$$

x represents k in stator terms and r in rotor terms

The matrix $\mathbf{J}$ is given as:

$$\mathbf{J} = \begin{bmatrix} 0 & -1 & 0 & 0 & 0 & 0 & 0 & 0 & 0 \\ 1 & 0 & 0 & 0 & 0 & 0 & 0 & 0 & 0 \\ 0 & 0 & 0 & 0 & 0 & 0 & 0 & 0 & 0 \\ 0 & 0 & 0 & 0 & -1 & 0 & 0 & 0 & 0 \\ 0 & 0 & 0 & 1 & 0 & 0 & 0 & 0 & 0 \\ 0 & 0 & 0 & 0 & 0 & 0 & 0 & 0 & 0 \\ 0 & 0 & 0 & 0 & 0 & 0 & 0 & -1 & 0 \\ 0 & 0 & 0 & 0 & 0 & 0 & 1 & 0 & 0 \\ 0 & 0 & 0 & 0 & 0 & 0 & 0 & 0 & 0 \end{bmatrix} \tag{2.58}$$

The flux linkage equation is transformed into

$$\underline{\Psi}^k = \mathbf{T}^k \cdot \underline{\Psi}^{SR} = \mathbf{T}^k \cdot \mathbf{L}^{SR} \cdot \underline{I}^{SR} = \mathbf{T}^k \cdot \mathbf{L}^{SR} \cdot \mathbf{T}^{-k} \cdot \underline{I}^k = \mathbf{L}^k \cdot \underline{I}^k \tag{2.59}$$

The voltage, current and flux linkage vectors in the transformed equations are

$$\begin{aligned} \underline{U}^k &= \left[\mathrm{U}_{\mathrm{sd1}} \quad \mathrm{U}_{\mathrm{sq1}} \quad \mathrm{U}_{\mathrm{s01}} \quad \mathrm{U}_{\mathrm{sd2}} \quad \mathrm{U}_{\mathrm{sq2}} \quad \mathrm{U}_{\mathrm{s02}} \quad \mathrm{U}_{\mathrm{rd}} \quad \mathrm{U}_{\mathrm{rq}} \quad \mathrm{U}_{\mathrm{r0}}\right]^{\mathrm{T}} \\ \underline{I}^k &= \left[\mathrm{I}_{\mathrm{sd1}} \quad \mathrm{I}_{\mathrm{sq1}} \quad \mathrm{I}_{\mathrm{s01}} \quad \mathrm{I}_{\mathrm{sd2}} \quad \mathrm{I}_{\mathrm{sq2}} \quad \mathrm{I}_{\mathrm{s02}} \quad \mathrm{I}_{\mathrm{rd}} \quad \mathrm{I}_{\mathrm{rq}} \quad \mathrm{I}_{\mathrm{r0}}\right]^{\mathrm{T}} \\ \underline{\Psi}^k &= \left[\Psi_{sd1} \quad \Psi_{sq1} \quad \Psi_{s01} \quad \Psi_{sd2} \quad \Psi_{sq2} \quad \Psi_{\mathrm{s02}} \quad \Psi_{\mathrm{rd}} \quad \Psi_{\mathrm{rq}} \quad \Psi_{\mathrm{r0}}\right]^{\mathrm{T}} \end{aligned} \tag{2.60}$$

The resistances are given in the diagonal matrix

$$\mathbf{R}^k = diag\left[\mathrm{R_s} \quad \mathrm{R_s} \quad \mathrm{R_s} \quad \mathrm{R_s} \quad \mathrm{R_s} \quad \mathrm{R_s} \quad \mathrm{R_r} \quad \mathrm{R_r} \quad \mathrm{R_r}\right] \tag{2.61}$$

The inductance matrix after transformation is obtained as

$$\mathbf{L}^k = \begin{bmatrix} L_{s\sigma} + \frac{3}{2}L_{sh} & 0 & 0 & \frac{3}{2}L_{sh} & 0 & 0 & \frac{3}{2}L_{srh} & 0 & 0 \\ 0 & L_{s\sigma} + \frac{3}{2}L_{sh} & 0 & 0 & \frac{3}{2}L_{sh} & 0 & 0 & \frac{3}{2}L_{srh} & 0 \\ 0 & 0 & L_{s\sigma} & 0 & 0 & 0 & 0 & 0 & 0 \\ \frac{3}{2}L_{sh} & 0 & 0 & L_{s\sigma} + \frac{3}{2}L_{sh} & 0 & 0 & \frac{3}{2}L_{srh} & 0 & 0 \\ 0 & \frac{3}{2}L_{sh} & 0 & 0 & L_{s\sigma} + \frac{3}{2}L_{sh} & 0 & 0 & \frac{3}{2}L_{srh} & 0 \\ 0 & 0 & 0 & 0 & 0 & L_{s\sigma} & 0 & 0 & 0 \\ \frac{3}{2}L_{srh} & 0 & 0 & \frac{3}{2}L_{srh} & 0 & 0 & L_{r\sigma} + \frac{3}{2}L_{rh} & 0 & 0 \\ 0 & \frac{3}{2}L_{srh} & 0 & 0 & \frac{3}{2}L_{srh} & 0 & 0 & L_{r\sigma} + \frac{3}{2}L_{rh} & 0 \\ 0 & 0 & 0 & 0 & 0 & 0 & 0 & 0 & L_{r\sigma} \end{bmatrix} \tag{2.62}$$

The inductance matrix can be written as

$$\mathbf{L}^k = \begin{bmatrix} L_s & 0 & 0 & L_h & 0 & 0 & L_h & 0 & 0 \\ 0 & L_s & 0 & 0 & L_h & 0 & 0 & L_h & 0 \\ 0 & 0 & L_{s\sigma} & 0 & 0 & 0 & 0 & 0 & 0 \\ L_h & 0 & 0 & L_s & 0 & 0 & L_h & 0 & 0 \\ 0 & L_h & 0 & 0 & L_s & 0 & 0 & L_h & 0 \\ 0 & 0 & 0 & 0 & 0 & L_{s\sigma} & 0 & 0 & 0 \\ L_h & 0 & 0 & L_h & 0 & 0 & L_{rd} & 0 & 0 \\ 0 & L_h & 0 & 0 & L_h & 0 & 0 & L_{rq} & 0 \\ 0 & 0 & 0 & 0 & 0 & 0 & 0 & 0 & L_{r\sigma} \end{bmatrix} \tag{2.63}$$

where

$$L_s = L_{s\sigma} + \frac{3}{2} L_{sh} \qquad L_r = L_{r\sigma} + \frac{3}{2} L_{srh} \qquad L_h = \frac{3}{2} L_{srh} = \frac{3}{2} L_{sh} \tag{2.64}$$

The electromagnetic torque can be obtained in terms of the transformed quantities using the following equation:

$$M_e = \frac{p}{2} \cdot \left(\underline{I}^{SR}\right)^{\mathsf{T}} \cdot \frac{\partial \mathbf{L}^{SR}(\theta)}{\partial \theta} \cdot \underline{I}^{SR} = \frac{p}{2} \cdot \left(\mathbf{T}^{-k} \cdot \underline{I}^k\right)^{\mathsf{T}} \cdot \frac{\partial \mathbf{L}^{SR}(\theta)}{\partial \theta} \cdot \mathbf{T}^{-k} \cdot \underline{I}^k = \frac{p}{2} \cdot \left(\underline{I}^k\right)^{\mathsf{T}} \cdot \left(\mathbf{T}^{-k}\right)^{\mathsf{T}} \cdot \frac{\partial \mathbf{L}^{SR}(\theta)}{\partial \theta} \cdot \mathbf{T}^{-k} \cdot \underline{I}^k \tag{2.65}$$

This gives

$$M_e = \frac{p}{2} \cdot 3 \cdot L_h \cdot \left(I_{sq1} \cdot I_{rd} - I_{sd1} \cdot I_{rq} + I_{sq2} \cdot I_{rd} - I_{sd2} \cdot I_{rq}\right) \tag{2.66}$$

which can be written in terms of rotor quantities as

$$M_e = \frac{p}{2} \cdot 3 \cdot \left(\Psi_{rq} \cdot I_{rd} - \Psi_{rd} \cdot I_{rq}\right) \tag{2.67}$$

The torque expression in terms of stator quantities is

$$M_e = \frac{p}{2} \cdot 3 \cdot \left(\Psi_{sd1} \cdot I_{sq1} - \Psi_{sq1} \cdot I_{sd1} + \Psi_{sd2} \cdot I_{sq2} - \Psi_{sq2} \cdot I_{sd2}\right) \tag{2.68}$$

2.3.2.2 Transformed Per Unit Model

The transformed per unit model of the machine in double synchronous coordinates is obtained after scaling the transformed equations in (2.57), (2.59) and (2.67) by the basis values. The same definition of the per unit system used is used as the one in single synchronous modelling (section 2.2.2.2). Thus the peak phase voltages, peak phase currents and peak flux linkage values are used as the basis values for voltage, current and flux linkage respectively. The basis values for power and torque are the same as the ones used in single synchronous modelling.

The stator and rotor voltage equations in per unit are obtained as

$$\begin{aligned} u_{sd1} &= r_s \cdot i_{sd1} + \frac{1}{\omega_n} \cdot \frac{d\psi_{sd1}}{dt} - f_k \cdot \psi_{sq1} & u_{sq1} &= r_s \cdot i_{sq1} + \frac{1}{\omega_n} \cdot \frac{d\psi_{sq1}}{dt} + f_k \cdot \psi_{sd1} \\ u_{sd2} &= r_s \cdot i_{sd2} + \frac{1}{\omega_n} \cdot \frac{d\psi_{sd2}}{dt} - f_k \cdot \psi_{sq2} & u_{sq2} &= r_s \cdot i_{sq2} + \frac{1}{\omega_n} \cdot \frac{d\psi_{sq2}}{dt} + f_k \cdot \psi_{sd2} \\ 0 &= r_r \cdot i_{rd} + \frac{1}{\omega_n} \cdot \frac{d\psi_{rd}}{dt} - f_r \cdot \psi_{rq} & 0 &= r_r \cdot i_{rq} + \frac{1}{\omega_n} \cdot \frac{d\psi_{rq}}{dt} + f_r \cdot \psi_{rd} \end{aligned} \tag{2.68}$$

The flux linkages are

$$\begin{aligned} \psi_{sd1} &= x_s \cdot i_{sd1} + x_h \cdot i_{sd2} + x_h \cdot i_{rd} & \psi_{sq1} &= x_s \cdot i_{sq1} + x_h \cdot i_{sq2} + x_h \cdot i_{rq} \\ \psi_{sd2} &= x_s \cdot i_{sd2} + x_h \cdot i_{sd1} + x_h \cdot i_{rd} & \psi_{sq2} &= x_s \cdot i_{sq2} + x_h \cdot i_{sq1} + x_h \cdot i_{rq} \\ \psi_{rd} &= x_r \cdot i_{rd} + x_h \cdot i_{sd1} + x_h \cdot i_{sd2} & \psi_{rq} &= x_r \cdot i_{rq} + x_h \cdot i_{sq1} + x_h \cdot i_{sq2} \end{aligned} \tag{2.69}$$

The quantities in (0_1, 0_2) subspace are not excited for similar reasons as in the single synchronous modelling. Thus they are omitted from the model.

The electromagnetic torque and other mechanical system equations in per unit are given as

$$\begin{aligned} & m_e = \frac{\psi_{sd1} \cdot i_{sq1} - \psi_{sq1} \cdot i_{sd1} + \psi_{sd2} \cdot i_{sq2} - \psi_{sq2} \cdot i_{sd2}}{2} \\ & T_m \cdot \frac{dn}{dt} = m_e - m_L \qquad T_m = \frac{J \cdot \Omega_N^2}{S_N} \\ & \frac{d\theta}{dt} = \omega_n \cdot n \qquad \theta_{mech} = \frac{\theta}{p} \\ & f_r = f_k - n \qquad f_k = \frac{\omega_k}{\omega_n} \qquad f_r = \frac{\omega_r}{\omega_n} \end{aligned} \tag{2.70}$$

From the voltage and flux linkage equations in (2.68) and (2.69), the per unit equivalent circuit of the machine in double synchronous frame can be drawn as in Figure 2.5.

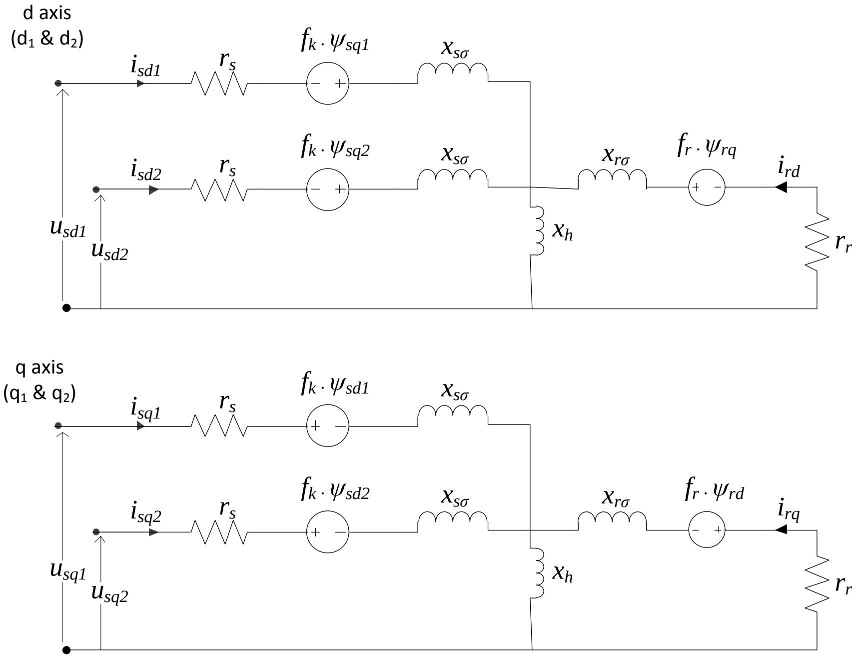

Figure 2.5: Per unit equivalent circuit of SPIM in double synchronous frame

In this chapter, two different modelling approaches of the six-phase induction machine were considered. It is important to establish the relationship between the two models. From the definition of rotor windings, the transformation equations, the transformed inductance matrices and the pu system definitions, the relationship between the two pu models is derived and summarized as follows:

Equivalent circuit parameters

$$r_s^{II} = r_s^I \qquad x_{s\sigma}^{II} = x_{s\sigma}^I$$

$$r_r^{II} = \frac{r_r^I}{2} \qquad x_{r\sigma}^{II} = \frac{x_{r\sigma}^I}{2} \qquad x_h^{II} = \frac{x_h^I}{2}$$

Currents

$$i_{sd}^I = \frac{i_{sd1}^{II} + i_{sd2}^{II}}{2} \qquad i_{sq}^I = \frac{i_{sq1}^{II} + i_{sq2}^{II}}{2}$$

$$i_{rd}^I = \frac{i_{rd}^{II}}{2} \qquad i_{rq}^I = \frac{i_{rq}^{II}}{2}$$

Fluxes

$$\psi_{sd}^I = \frac{\psi_{sd1}^{II} + \psi_{sd2}^{II}}{2} \qquad \psi_{sq}^I = \frac{\psi_{sq1}^{II} + \psi_{sq2}^{II}}{2}$$

$$\psi_{rd}^I = \psi_{rd}^{II} \qquad \psi_{rq}^I = \psi_{rq}^{II}$$

Voltages

$$u_{sd}^I = \frac{u_{sd1}^{II} + u_{sd2}^{II}}{2} \qquad u_{sq}^I = \frac{u_{sq1}^{II} + u_{sq2}^{II}}{2}$$

$$u_{rd}^I = u_{rd}^{II} = 0 \qquad u_{rq}^I = u_{rq}^{II} = 0 \tag{2.71}$$

Torque

$$m_e^I = m_e^{II}$$

The superscript I indicates quantities in single synchronous modelling, whereas quantities in double synchronous modelling are designated using the superscript II.

3 Modelling of Inverters for Six-Phase Induction Machine

3.1 Introduction

Inverters are required to supply six-phase machines mainly for two reasons. The first is because the mains supply is normally three-phase. Therefore, a supply that can give six-phase currents with the correct phase difference is required. Secondly the currents into the machine need to be controlled precisely for variable speed operation.

In this chapter, two different topologies of inverters for a six-phase machine are discussed. A brief discussion of six-phase two-level inverter is presented first. Then a more detailed analysis of two three-phase inverters with separate DC links is presented. Pulse width modulation (PWM) techniques for this topology are mentioned with particular emphasis on sinusoidal PWM with 3rd harmonic injection. Only voltage source inverter (VSI) is considered in this chapter.

3.2 Six-phase Two-level Inverter

A six-phase two-level inverter can be built by connecting six bridge legs as shown in Figure 3.1. The a_1, a_2, b_1, b_2, c_1 and c_2 terminals are connected to the corresponding six-phase machine terminals. The switch gate signals are obtained from a controller so that appropriate magnitude and phase of currents are delivered to the machine. A six-phase two-level inverter can also be formed from two three-phase two-level inverters by connecting them to a common DC link.

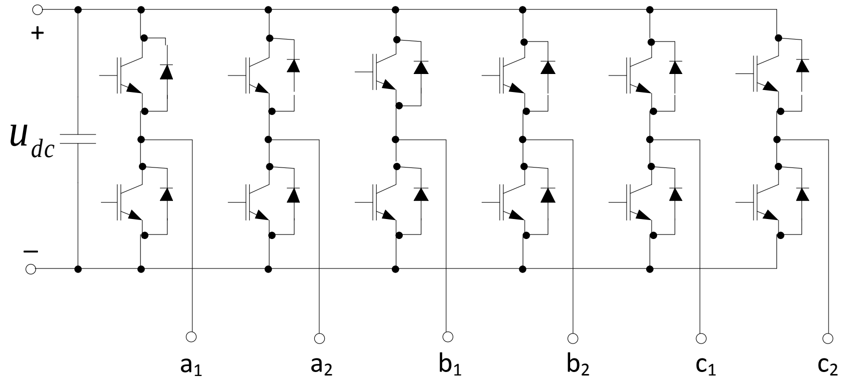

Figure 3.1: Six-phase 2-level voltage source inverter

In each leg of a six-phase inverter only one switch can be ON at a time to avoid short circuiting the DC link. The switching of the six legs can be taken as independent form one another. This gives 64 possible switching states in the complete inverter. Different digital PWM techniques can be used to control the inverter including conventional space vector modulation, vector space decomposition, vector classification, double zero-sequence injection and sinusoidal PWM [6]. However, the six-phase 2-level inverter will not be discussed anymore because it has not been used in this thesis.

3.3 Three-phase Inverters with Split DC Link

A six-phase machine can also be supplied from two three-phase inverters with separate DC links as shown in Figure 3.2. The terminals from the two inverters are connected to the corresponding terminals of the six-phase machine. This configuration is preferred to the six-phase inverter or two three-phase inverters with common DC link in this thesis. This is because it offers redundancy and better reliability. If one DC link fails or one of the inverters trips, the machine can continue to run from the remaining DC link and inverter. However, the control becomes more complicated because of the need to ensure fault tolerance of the drive in the event of low DC link voltage or trip of one inverter.

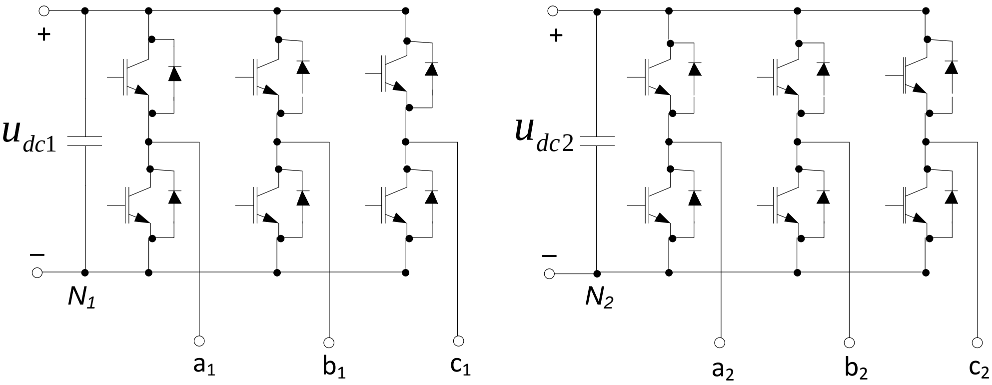

Figure 3.2: Two 3-phase inverters with split DC link

To apply appropriate control to the inverters, a relationship between inverter voltages and the motor voltages must be established. Let N_1 and N_2 represent the negative terminals of DC link 1 and DC link 2, respectively, as shown in Figure 3.2, and let n_1 and n_2 represent the neutral points of phase group 1 and phase group 2, respectively. In the following analysis, only inverter 1 and phase group 1 will be used. Then it is later generalized for the other inverter and phase group. The analysis is mainly based on the derivation in [9].

The inverter line-to-line voltages can be obtained from the bridge leg phase voltages as

$$\begin{aligned} U_{a_1b_1}(t) &= U_{a_1N_1}(t) - U_{b_1N_1}(t) \\ U_{b_1c_1}(t) &= U_{b_1N_1}(t) - U_{c_1N_1}(t) \\ U_{c_1a_1}(t) &= U_{c_1N_1}(t) - U_{a_1N_1}(t) \end{aligned} \tag{3.1}$$

The inverter line-to-line and machine line-to-line voltages are equal. This gives

$$\begin{aligned}
&U_{a_1N_1}(t)-U_{b_1N_1}(t)=U_{a_1n_1}(t)-U_{b_1n_1}(t)\\
&U_{b_1N_1}(t)-U_{c_1N_1}(t)=U_{b_1n_1}(t)-U_{c_1n_1}(t)\\
&U_{c_1N_1}(t)-U_{a_1N_1}(t)=U_{c_1n_1}(t)-U_{a_1n_1}(t)
\end{aligned} \tag{3.2}$$

The zero system voltage *U₀* in phase group 1 can be expressed as function of the phase voltages of the machine as follows:

$$U_0(t)=\frac{U_{a_1}(t)+U_{b_1}(t)+U_{c_1}(t)}{3} \tag{3.3}$$

From equations (3.2) and (3.3),

$$\begin{aligned}
&U_{a_1}(t)=\frac{1}{3}\cdot\left(2\cdot U_{a_1N_1}(t)-U_{b_1N_1}(t)-U_{c_1N_1}(t)\right)+U_0\\
&U_{b_1}(t)=\frac{1}{3}\cdot\left(2\cdot U_{b_1N_1}(t)-U_{c_1N_1}(t)-U_{a_1N_1}(t)\right)+U_0\\
&U_{c_1}(t)=\frac{1}{3}\cdot\left(2\cdot U_{c_1N_1}(t)-U_{a_1N_1}(t)-U_{b_1N_1}(t)\right)+U_0
\end{aligned} \tag{3.4}$$

It can be assumed that there is no zero system voltage as long as the sum of stator currents is zero. Then the following relationship between bridge leg voltages and motor phase voltages is obtained:

$$\begin{aligned}
&U_{a_1}(t)=\frac{1}{3}\cdot\left(2\cdot U_{a_1N_1}(t)-U_{b_1N_1}(t)-U_{c_1N_1}(t)\right)\\
&U_{b_1}(t)=\frac{1}{3}\cdot\left(2\cdot U_{b_1N_1}(t)-U_{c_1N_1}(t)-U_{a_1N_1}(t)\right)\\
&U_{c_1}(t)=\frac{1}{3}\cdot\left(2\cdot U_{c_1N_1}(t)-U_{a_1N_1}(t)-U_{b_1N_1}(t)\right)
\end{aligned} \tag{3.5}$$

This implies that by controlling the inverter bridge leg voltages, the phase voltages of the machine can be controlled.

The average representation of a bridge leg can be used to analyse and control a switch model three-phase inverter [33]. The duty ratio of each bridge leg is the ratio of the pulse width (the time interval the upper switch in the leg is 'on' within a switching period) to the switching period. Considering sinusoidal PWM, which is explained in more detail in the next section, the duty ratios of the three bridge legs of inverter 1 can be expressed in terms of the control voltage as

$$
\begin{aligned}
d_{a1}(t) &= \frac{1}{2}\left(1+\frac{u_{sta1}(t)}{\hat{u}_{tri}}\right) = \frac{1}{2}\left(1+u_{st1}\cdot\cos(\zeta_1)\right) = \frac{1}{2}\left(1+u_{st1}\cdot\cos(\omega_{s1}t)\right) \\
d_{b1}(t) &= \frac{1}{2}\left(1+\frac{u_{stb1}(t)}{\hat{u}_{tri}}\right) = \frac{1}{2}\left(1+u_{st1}\cdot\cos(\zeta_1-120^0)\right) = \frac{1}{2}\left(1+u_{st1}\cdot\cos(\omega_{s1}t-120^0)\right) \\
d_{c1}(t) &= \frac{1}{2}\left(1+\frac{u_{stc1}(t)}{\hat{u}_{tri}}\right) = \frac{1}{2}\left(1+u_{st1}\cdot\cos(\zeta_1-240^0)\right) = \frac{1}{2}\left(1+u_{st1}\cdot\cos(\omega_{s1}t-240^0)\right)
\end{aligned} \tag{3.6}
$$

where u_{st1} and ω_{s1} are the amplitude and frequency of the control voltage for inverter 1 obtained from the current controller. The amplitude of the triangular carrier signal $\hat{u}_{tri}$ is taken as unity, so left out of the subsequent formulas.

The average values of the inverter leg voltages during a switching period can be obtained from the DC link voltage and the duty ratios [33].

$$
\begin{aligned}
\overline{U}_{a_1N_1}(t) &= U_{dc1}\cdot d_{a1}(t) \\
\overline{U}_{b_1N_1}(t) &= U_{dc1}\cdot d_{b1}(t) \\
\overline{U}_{c_1N_1}(t) &= U_{dc1}\cdot d_{c1}(t)
\end{aligned} \tag{3.7}
$$

From equations (3.5) and (3.7) the motor phase voltages can be expressed as

$$
\begin{aligned}
U_{a_1}(t) &= \frac{U_{dc1}}{3}\cdot\left(2\cdot d_{a1}(t)-d_{b1}(t)-d_{c1}(t)\right) \\
U_{b_1}(t) &= \frac{U_{dc1}}{3}\cdot\left(2\cdot d_{b1}(t)-d_{a1}(t)-d_{c1}(t)\right) \\
U_{c_1}(t) &= \frac{U_{dc1}}{3}\cdot\left(2\cdot d_{c1}(t)-d_{a1}(t)-d_{b1}(t)\right)
\end{aligned} \tag{3.8}
$$

Combining equations (3.6) and (3.8), and using trigonometric identities, the following average motor phase voltages are obtained within a switching period:

$$
\begin{aligned}
U_{a_1}(t) &= \frac{U_{dc1}}{2}\cdot u_{st1}\cdot\cos(\zeta_1) \\
U_{b_1}(t) &= \frac{U_{dc1}}{2}\cdot u_{st1}\cdot\cos(\zeta_1-120^0) \\
U_{c_1}(t) &= \frac{U_{dc1}}{2}\cdot u_{st1}\cdot\cos(\zeta_1-240^0)
\end{aligned} \tag{3.9}
$$

The control of the six-phase machine is done in synchronous rotor field oriented reference frame. Therefore, it is important to establish the relationship between the control voltage and the motor voltages in this frame of reference. Using the amplitude invariant Clarke transform, the motor voltages in stationary orthogonal coordinates can be obtained as

$$\begin{bmatrix} U_{d1}^s \\ U_{q1}^s \\ U_{01} \end{bmatrix} = \frac{1}{3} \cdot \begin{bmatrix} 2 & -1 & -1 \\ 0 & \sqrt{3} & -\sqrt{3} \\ 1 & 1 & 1 \end{bmatrix} \cdot \begin{bmatrix} U_{a_1} \\ U_{b_1} \\ U_{c_1} \end{bmatrix} = \frac{1}{3} \cdot \cdot \begin{bmatrix} 2 & -1 & -1 \\ 0 & \sqrt{3} & -\sqrt{3} \\ 1 & 1 & 1 \end{bmatrix} \cdot \frac{U_{dc1}}{2} \cdot u_{st1} \cdot \begin{bmatrix} \cos(\zeta_1) \\ \cos(\zeta_1 - 120^0) \\ \cos(\zeta_1 - 240^0) \end{bmatrix} \tag{3.10}$$

This can be simplified to

$$\begin{bmatrix} U_{d1}^s \\ U_{q1}^s \\ U_{01} \end{bmatrix} = \frac{U_{dc1}}{2} \cdot u_{st1} \cdot \begin{bmatrix} \cos(\zeta_1) \\ \sin(\zeta_1) \\ 0 \end{bmatrix} \tag{3.11}$$

Park's transform can be used to transform quantities in equation (3.11) to a rotor field oriented reference frame. The transform used is

$$\begin{bmatrix} U_{d1} \\ U_{q1} \\ U_{01} \end{bmatrix} = \begin{bmatrix} \cos\theta_k & \sin\theta_k & 0 \\ -\sin\theta_k & \cos\theta_k & 0 \\ 0 & 0 & 1 \end{bmatrix} \begin{bmatrix} U_{d1}^s \\ U_{q1}^s \\ U_{01} \end{bmatrix} \tag{3.12}$$

A relationship between the stator voltages in synchronous frame and the control voltage is obtained from equations (3.11) and (3.12).

$$\begin{aligned} U_{d1} &= \frac{U_{dc1}}{2} \cdot u_{st1} \cdot \cos(\zeta_1 - \theta_k) \\ U_{q1} &= \frac{U_{dc1}}{2} \cdot u_{st1} \cdot \sin(\zeta_1 - \theta_k) \end{aligned} \tag{3.13}$$

Similar analysis can be carried out for inverter 2 and phase group 2 by replacing corresponding values and taking the phase shift into account. This gives

$$\begin{aligned} U_{d2} &= \frac{U_{dc2}}{2} \cdot u_{st2} \cdot \cos(\zeta_2 - (\theta_k - 30^0)) \\ U_{q2} &= \frac{U_{dc2}}{2} \cdot u_{st2} \cdot \sin(\zeta_2 - (\theta_k - 30^0)) \end{aligned} \tag{3.14}$$

Scaling (3.13) and (3.14) by the per unit system defined in Appendix Six-phase Induction Machine Nameplate Data & Circuit Parameters, the relationship between pu stator voltages and control voltages is given as

$$
\begin{aligned}
u_{d1} &= u_{dc1} \cdot u_{st1} \cdot \cos(\zeta_1 - \theta_k) \\
u_{q1} &= u_{dc1} \cdot u_{st1} \cdot \sin(\zeta_1 - \theta_k) \\
u_{d2} &= u_{dc2} \cdot u_{st2} \cdot \cos(\zeta_2 - (\theta_k - 30^0)) \\
u_{q2} &= u_{dc2} \cdot u_{st2} \cdot \sin(\zeta_2 - (\theta_k - 30^0))
\end{aligned}
\tag{3.15}
$$

This relationship is used to obtain the amplitude and angle of the control voltage used in the PWM modulation of the inverters from the outputs of the current controllers as discussed in chapter 4.1.

3.4 Pulse Width Modulation Techniques

The main goal of the PWM control strategy is to impose the reference stator voltage vector generated by the current controller. There are different types of PWM techniques that can be used for controlling inverters for six-phase operation [6]. In this thesis, only sinusoidal PWM and sinusoidal PWM with third harmonic injection are considered.

Considering inverter 1, the control voltages in sinusoidal PWM are given as

$$
\begin{aligned}
u_{sta1}(t) &= u_{st1} \cdot \cos(\omega_{s1} \cdot t) \\
u_{stb1}(t) &= u_{st1} \cdot \cos(\omega_{s1} \cdot t - 120^0) \\
u_{stc1}(t) &= u_{st1} \cdot \cos(\omega_{s1} \cdot t - 240^0)
\end{aligned}
\tag{3.16}
$$

These are compared with a triangular signal of a given frequency (the switching frequency) to generate the gate pulses that control the inverter switches [34]. This is shown in Figure 3.3 for the upper switch of the first bridge leg in inverter 1 (a_1).

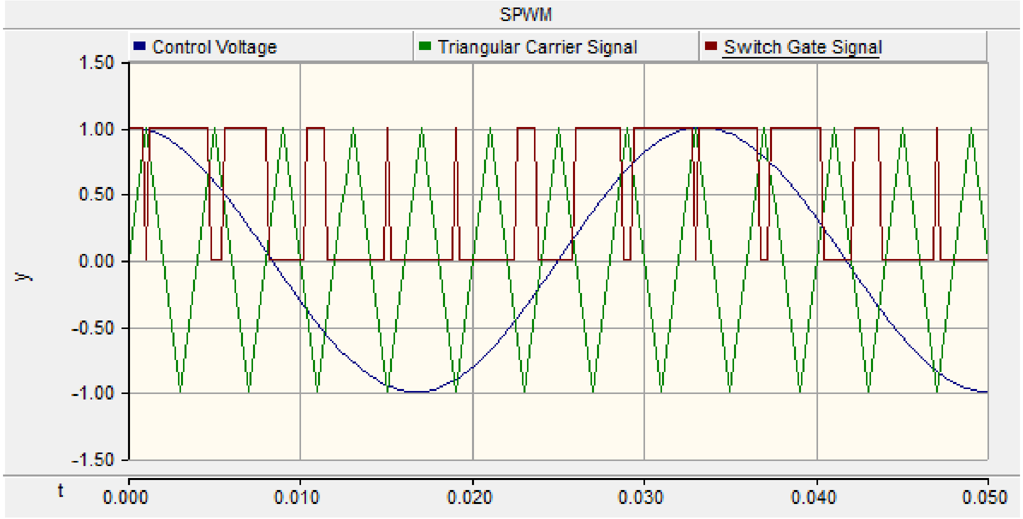

Figure 3.3: Sinusoidal PWM

The maximum line-to-line rms voltage that can be obtained using sinusoidal PWM in the linear range can be obtained as [35]

$$U_{LL,\max,rms}=\frac{\sqrt{3}}{\sqrt{2}}\cdot\frac{U_{dc}}{2}\approx 0.612U_{dc} \tag{3.17}$$

Harmonic distortion can be used to improve the linear modulation range of a three-phase voltage-source inverter. The harmonics introduced appear in the bridge leg voltages but cancel out in the motor phase voltages. This can be achieved by adding a third harmonic with certain amplitude to the fundamental. The maximum improvement in linear range is obtained when the amplitude of the third harmonic is one-sixth that of the fundamental [36]. Taking inverter 1, the control voltages for sinusoidal PWM with third harmonic injection are

$$\begin{aligned} u_{sta1}(t)&=u_{st1}\cdot\left[\cos(\omega_{s1}\cdot t)-\frac{1}{6}\cdot\cos(3\cdot\omega_{s1}\cdot t)\right]\\ u_{stb1}(t)&=u_{st1}\cdot\left[\cos(\omega_{s1}\cdot t-120^0)-\frac{1}{6}\cdot\cos(3\cdot\omega_{s1}\cdot t)\right]\\ u_{stc1}(t)&=u_{st1}\cdot\left[\cos(\omega_{s1}\cdot t-240^0)-\frac{1}{6}\cdot\cos(3\cdot\omega_{s1}\cdot t)\right]\end{aligned} \tag{3.18}$$

This is shown in Figure 3.4 for the upper switch of the first bridge leg in inverter 1 (a_1). The value of u_{st} in the figure is equal to one. The maximum possible value of u_{st} for linear modulation is obtained when the amplitude of the control voltage and the triangular signal are equal. This is the case for

$$u_{st,\max} = \frac{2}{\sqrt{3}} \tag{3.19}$$

From equations (3.9) and (3.19), the maximum value of peak phase voltage in the machine is obtained as

$$\hat{U}_{phase,\max} = \frac{U_{dc}}{2} \cdot u_{st,\max} = \frac{U_{dc}}{\sqrt{3}} \tag{3.20}$$

Thus the maximum line-to-line rms voltage that can be obtained using sinusoidal PWM with 3rd harmonic injection in the linear range is

$$U_{LL,\max,rms} = \frac{\sqrt{3}}{\sqrt{2}} \cdot \frac{U_{dc}}{\sqrt{3}} \approx 0.707 U_{dc} \tag{3.21}$$

From this, it can be concluded that sinusoidal PWM with 3rd harmonic injection provides better utilization of the DC link voltage as compared to pure sinusoidal PWM. The improvement is approximately by 15%. For this reason, sinusoidal PWM with 3rd harmonic injection is used in this thesis.

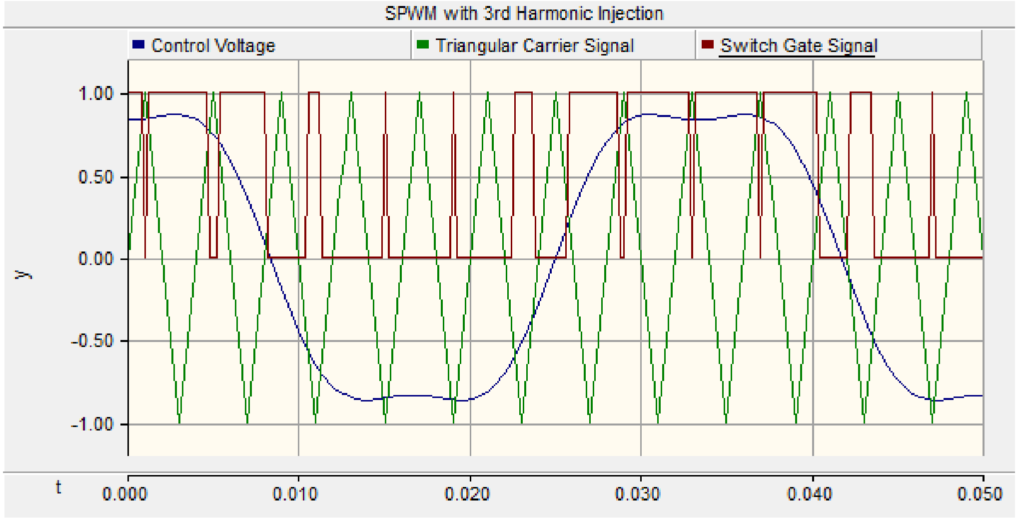

Figure 3.4: Sinusoidal PWM with third harmonic injection

The control signals for both inverters of the six phase machine are

$$
\begin{aligned}
u_{sta1}(t) &= u_{st1}\cdot\left[\cos(\zeta_1(t)-\frac{1}{6}\cdot\cos(3\cdot\zeta_1(t))\right]\\
u_{stb1}(t) &= u_{st1}\cdot\left[\cos(\zeta_1(t)-120^0)-\frac{1}{6}\cdot\cos(3\cdot\zeta_1(t))\right]\\
u_{stc1}(t) &= u_{st1}\cdot\left[\cos(\zeta_1(t)-240^0)-\frac{1}{6}\cdot\cos(3\cdot\zeta_1(t))\right]\\
u_{sta2}(t) &= u_{st2}\cdot\left[\cos(\zeta_2(t)-30^0)-\frac{1}{6}\cdot\cos(3\cdot\left(\zeta_2(t)-30^0\right))\right]\\
u_{stb2}(t) &= u_{st2}\cdot\left[\cos(\zeta_2(t)-150^0)-\frac{1}{6}\cdot\cos(3\cdot\left(\zeta_2(t)-30^0\right))\right]\\
u_{stc2}(t) &= u_{st2}\cdot\left[\cos(\zeta_2(t)-270^0)-\frac{1}{6}\cdot\cos(3\cdot\left(\zeta_2(t)-30^0\right))\right]
\end{aligned}
\tag{3.22}
$$

The average voltages, which are equal to the reference voltages that should be generated, are given as

$$
\begin{aligned}
\underline{U}_s^s &= \begin{bmatrix} U_d^s \\ U_q^s \end{bmatrix} = \frac{\underline{U}_{s1}^s}{2}+\frac{\underline{U}_{s2}^s}{2} = \frac{1}{2}\cdot\left(U_{s1}\cdot e^{j\varsigma_1(t)}+U_{s2}\cdot e^{j\varsigma_2(t)}\right)\\
&= \frac{U_{dc1}}{4}\cdot u_{st1}\cdot\begin{bmatrix}\cos(\zeta_1(t))\\ \sin(\zeta_1(t))\end{bmatrix}+\frac{U_{dc2}}{4}\cdot u_{st2}\cdot\begin{bmatrix}\cos(\zeta_2(t))\\ \sin(\zeta_2(t))\end{bmatrix}
\end{aligned}
\tag{3.23}
$$

In general the angles ζ_1 and ζ_2 would be equal in steady state; however, during transient conditions they may be different. For the (z_1, z_2) system

$$
\begin{aligned}
\underline{U}_z &= \begin{bmatrix} U_{z1} \\ U_{z2} \end{bmatrix} = \left(\frac{\underline{U}_{s1}^s}{2}\right)^* - \left(\frac{\underline{U}_{s2}^s}{2}\right)^* = \frac{1}{2}\cdot\left(U_{s1}\cdot e^{-j\varsigma_1(t)}-U_{s2}\cdot e^{-j\varsigma_2(t)}\right)\\
&= \frac{U_{dc1}}{4}\cdot u_{st1}\cdot\begin{bmatrix}\cos(\zeta_1(t))\\ -\sin(\zeta_1(t))\end{bmatrix}-\frac{U_{dc2}}{4}\cdot u_{st2}\cdot\begin{bmatrix}\cos(\zeta_2(t))\\ -\sin(\zeta_2(t))\end{bmatrix}
\end{aligned}
\tag{3.24}
$$

If the system had common dc-link and common control signals, the average voltage in the (z_1, z_2) system would be zero. However, with separate dc-links and separate current controllers, both u_{st1} and u_{st2}, as well as ζ_1 and ζ_2 , may differ during transient states. Non-linear effects in the inverters may give harmonics in "average"-voltages in the (z_1, z_2) system. The z-vector is the difference between the stator voltage vectors for the two three-phase groups, however, rotating in the opposite direction. The conclusion is that when the two stator voltage vectors are different, the z-system will be excited [9].

4 Control of Six-Phase Induction Machine

4.1 Introduction

Scalar control and vector control are two commonly used methods in the operation of induction motor drives. In scalar control, the motor speed can be controlled by controlling the frequency and magnitude of the stator voltages applied to the motor. The control method is also known as volts-per-Hertz (V/Hz) control because the amplitude and frequency of the applied voltages have a linear relationship in order to maintain rated flux in the machine [33].

Vector control works with vector quantities, where the voltages and currents in the machine as represented by space phasors. It is also known as field oriented control (FOC). The magnitude, frequency and phase of these quantities are controlled in this method. The ability to produce a step change in torque on command is necessary for high performance drive systems. This can be achieved using vector control, which enables the torque and flux of the machine to be controlled independently. As an alternative to FOC, direct torque control (DTC) can also be used. In DTC, the torque and flux are directly controlled by applying the appropriate stator voltage vector [33], [35]. Compared to FOC, DTC is less commonly used.

Vector control can be divided into direct and indirect. Direct vector control uses flux measurement using sensors, while indirect vector control computes the flux from the stator currents and/or voltages. Indirect vector control is considered in this thesis.

The modelling of six-phase induction machine was presented in chapter 2. Two different approaches were considered: modelling in single synchronous reference frame and modelling in double synchronous reference frame. These leads to two different vector control methods, termed as single synchronous frame control (SSFC) and double synchronous frame control (DSFC). In this chapter, control of the six-phase induction motor drive using these methods is presented. Theoretical basis and design of both inner and outer controllers is included.

The control of six-phase induction motor drive is shown in the block diagram of figure 4.1. The outer controllers in the system are speed controller and flux controller. The rotor speed is measured using a sensor, while the flux is computed using the flux model. Various limiter variables are included in the control system to operate the drive in desired operating limits and to ensure appropriate response to fault conditions [12]. The current control method depends on whether SSFC or DSFC is chosen. This is described in the next two sections.

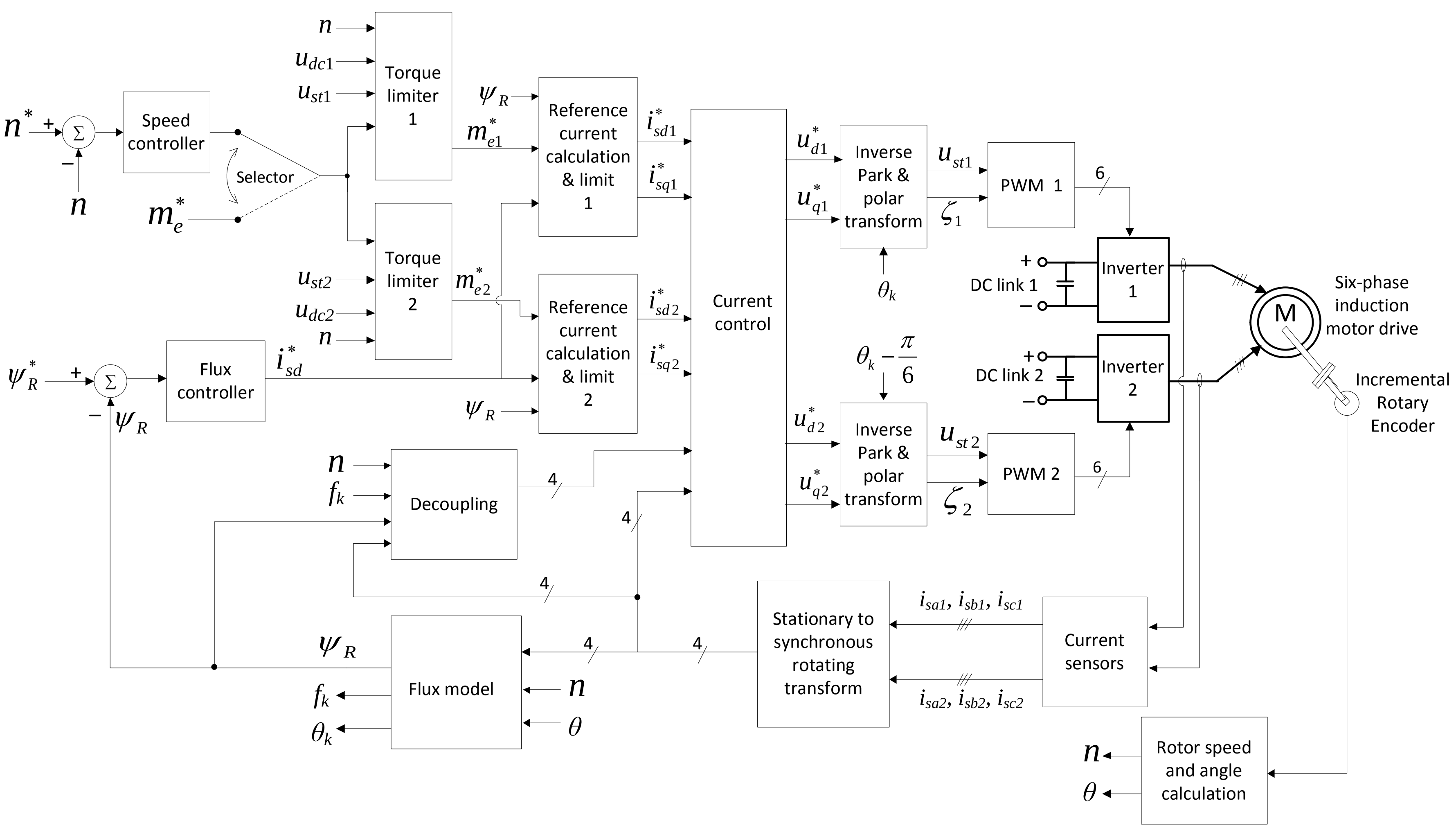

Figure 4.1: Indirect vector control of six-phase induction machine

4.2 Single Synchronous Frame Control

4.2.1 Introduction

The model of six-phase induction machine in single synchronous reference frame was developed in chapter 2.2. In this section, control of the machine based on this model is presented. The flux model, current (torque) control, flux control and speed control of the machine are discussed.

The per unit equations of the model were obtained in chapter 2.2 as follows:

$$\begin{aligned}
u_{sd} &= r_s \cdot i_{sd} + \frac{1}{\omega_n}\cdot\frac{d\psi_{sd}}{dt} - f_k \cdot \psi_{sq} & u_{sq} &= r_s \cdot i_{sq} + \frac{1}{\omega_n}\cdot\frac{d\psi_{sq}}{dt} + f_k \cdot \psi_{sd} \\
u_{sz1} &= r_s \cdot i_{sz1} + \frac{1}{\omega_n}\cdot\frac{d\psi_{sz1}}{dt} + f_k \cdot \psi_{sz2} & u_{sz2} &= r_s \cdot i_{sz2} + \frac{1}{\omega_n}\cdot\frac{d\psi_{sz2}}{dt} - f_k \cdot \psi_{sz1} \\
0 &= r_r \cdot i_{rd} + \frac{1}{\omega_n}\cdot\frac{d\psi_{rd}}{dt} - f_r\, \psi_{rq} & 0 &= r_r \cdot i_{rq} + \frac{1}{\omega_n}\cdot\frac{d\psi_{rq}}{dt} + f_r\, \psi_{rd} \\
\\
\psi_{sd} &= x_s \cdot i_{sd} + x_h \cdot i_{rd} & \psi_{sq} &= x_s \cdot i_{sq} + x_h \cdot i_{rq} \\
\psi_{sz1} &= x_{s\sigma} \cdot i_{sz1} & \psi_{sz2} &= x_{s\sigma} \cdot i_{sz2} \\
\psi_{rd} &= x_r \cdot i_{rd} + x_h \cdot i_{sd} & \psi_{rq} &= x_r \cdot i_{rq} + x_h \cdot i_{sq} \\
\\
m_e &= \psi_{rq} \cdot i_{sd} - \psi_{rd} \cdot i_{rq} \\
T_m \cdot \frac{dn}{dt} &= m_e - m_L
\end{aligned} \tag{4.1}$$

Since rotor field oriented control is used, the d-axis is aligned with the rotor flux linkage space vector. This implies

$$\psi_{rd} = \psi_r \qquad \psi_{rq} = 0 \qquad \frac{d\psi_{rq}}{dt} = 0 \tag{4.2}$$

Substituting these values in the rotor flux linkage equations of (4.1), and solving for the rotor currents gives

$$i_{rd} = \frac{\psi_r - x_h \cdot i_{sd}}{x_r}, \qquad i_{rq} = \frac{-x_h \cdot i_{sq}}{x_r} \tag{4.3}$$

The stator flux linkages can then be expressed as

$$\psi_{sd} = x_\sigma \cdot i_{sd} + \psi_R \qquad \psi_{sq} = x_\sigma \cdot i_{sq}$$

$$\text{where} \quad x_\sigma = \left(x_s - \frac{x_h^2}{x_r} \right), \qquad \psi_R = \frac{x_h}{x_r}\cdot\psi_r = \frac{\psi_r}{1+\sigma_r}, \qquad \sigma_r = \frac{x_{r\sigma}}{x_h} \tag{4.4}$$

Since indirect vector control is used, a flux model is needed to determine the rotor flux linkage vector magnitude and position. There are various models that can be used for this purpose. Two commonly used types of flux model are current model and voltage model. The current model uses only the measured stator currents for calculating the rotor flux vector. In the voltage model, the rotor flux linkage space vector is calculated as an integration of the stator voltage difference. The voltage model works well at high stator frequencies, whereas the current model is better for low frequencies. In addition, the voltage model is unsatisfactory for low stator frequencies [37]. Thus, the current model is the preferred choice for the application considered in this thesis.

The equations of the current model can be obtained from the rotor voltage equations in (4.1) by substituting for the rotor currents and rearranging the terms. This gives

$$\frac{d\psi_R}{dt} = -\frac{\psi_R}{T_r} + \frac{x_H}{T_r} \cdot i_{sd}$$

$$f_r = \frac{x_H \cdot i_{sq}}{T_r \cdot \omega_n \cdot \psi_R} \tag{4.5}$$

where $x_H = \frac{x_h}{1+\sigma_r} \qquad T_r = \frac{x_r}{\omega_n \cdot r_r}$

In the following sections, the design of controllers based on the above equations is covered. Design of inner (current) controllers is described first. Then the outer controllers (speed controller & flux controller) are designed.

4.2.2 Design of Inner Controllers

The inner control structure in SSFC is shown in Figure 4.2 . The measured currents and the current references obtained from the outer controllers and limiters are converted to the (d, q, z_1, z_2) reference frame. The current control and decoupling are implemented in this reference frame. Then the computed voltage references are converted to the (d_1, q_1) and (d_2, q_2) frames in order to compute the control voltages for the PWM operation of the two separate inverters.

The d-axis current is used to control the flux in the machine, and the q-axis current controls the torque. To control the unbalance in the currents of the two stator phase groups, the z_1 and z_2 currents are used. The unbalance may be due to different references, limiters, supply asymmetries or supply faults.

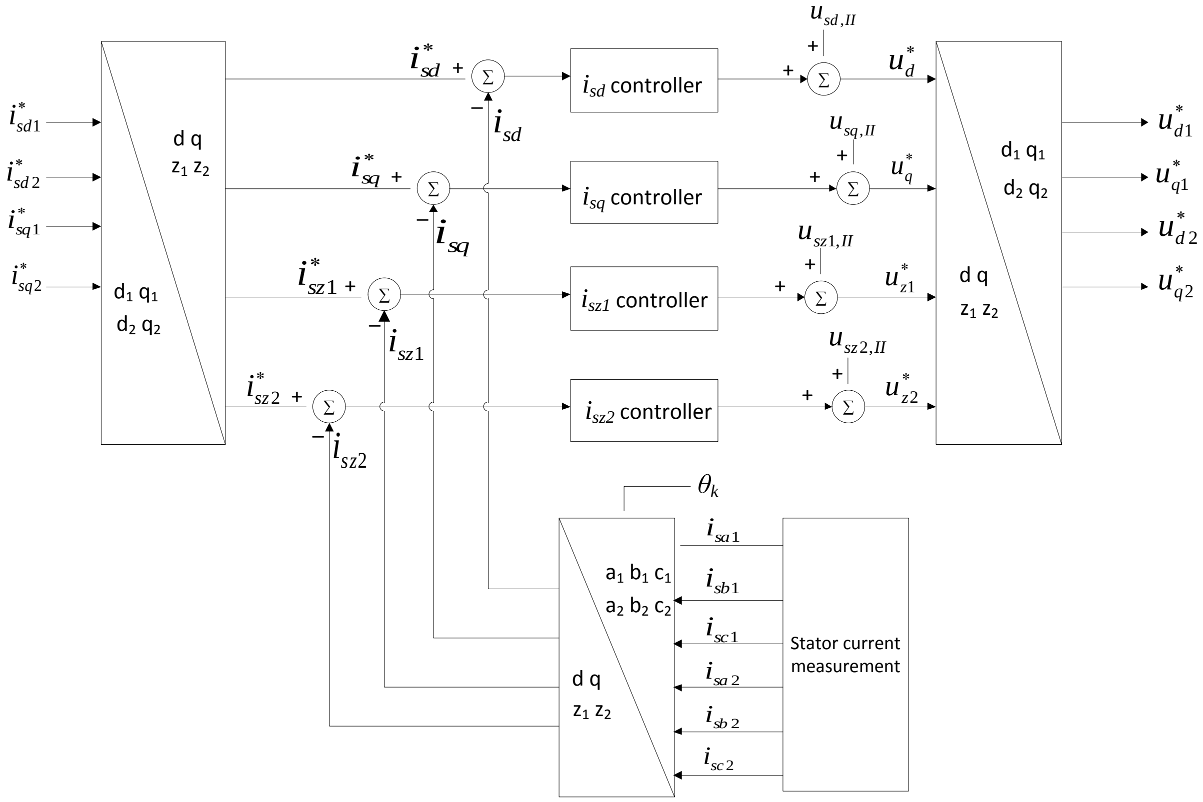

Figure 4.2: Single synchronous frame current control

The control equations needed for the current controllers can be obtained from the stator voltage equations in (4.1) by substituting for the stator flux linkages. This gives

$$\begin{aligned}
u_{sd} &= r_s \cdot i_{sd} + \frac{x_\sigma}{\omega_n} \cdot \frac{di_{sd}}{dt} - f_k \cdot x_\sigma \cdot i_{sq} + \frac{1}{\omega_n} \cdot \frac{d\psi_R}{dt} \\
u_{sq} &= r_s \cdot i_{sq} + \frac{x_\sigma}{\omega_n} \cdot \frac{di_{sq}}{dt} + f_k \cdot x_\sigma \cdot i_{sd} + f_k \cdot \psi_R \\
u_{sz1} &= r_s \cdot i_{sz1} + \frac{x_{s\sigma}}{\omega_n} \cdot \frac{di_{sz1}}{dt} + f_k \cdot x_{s\sigma} \cdot i_{sz2} \\
u_{sz2} &= r_s \cdot i_{sz2} + \frac{x_{s\sigma}}{\omega_n} \cdot \frac{di_{sz2}}{dt} - f_k \cdot x_{s\sigma} \cdot i_{sz1}
\end{aligned} \tag{4.6}$$

The d- and q-axis equations in (4.6) can be further modified using the following substitutions from the flux model:

$$\frac{d\psi_R}{dt} = -\frac{\psi_R}{T_r} + \frac{x_H}{T_r} \cdot i_{sd}$$
$$f_k \cdot \psi_R = (f_r + n) \cdot \psi_R = \left(\frac{x_H \cdot i_{sq}}{T_r \cdot \omega_n \cdot \psi_R} + n \right) \cdot \psi_R = \frac{x_H \cdot i_{sq}}{T_r \cdot \omega_n} + n \cdot \psi_R \tag{4.7}$$

This gives

$$u_{sd} = r_s' \cdot i_{sd} + \frac{x_\sigma}{\omega_n} \cdot \frac{di_{sd}}{dt} - f_k \cdot x_\sigma \cdot i_{sq} - \frac{\psi_R}{T_r \cdot \omega_n}$$
$$u_{sq} = r_s' \cdot i_{sq} + \frac{x_\sigma}{\omega_n} \cdot \frac{di_{sq}}{dt} + f_k \cdot x_\sigma \cdot i_{sd} + n \cdot \psi_R$$
$$u_{sz1} = r_s \cdot i_{sz1} + \frac{x_{s\sigma}}{\omega_n} \cdot \frac{di_{sz1}}{dt} + f_k \cdot x_{s\sigma} \cdot i_{sz2} \tag{4.8}$$
$$u_{sz2} = r_s \cdot i_{sz2} + \frac{x_{s\sigma}}{\omega_n} \cdot \frac{di_{sz2}}{dt} - f_k \cdot x_{s\sigma} \cdot i_{sz1}$$

where $r_s' = r_s + r_R$ and $r_R = \frac{x_H}{\omega_n \cdot T_r} = \frac{r_r}{(1+\sigma_r)^2}$

The control terms are thus obtained as

$$u_{sd,I} = r_s' \cdot i_{sd} + \frac{x_\sigma}{\omega_n} \cdot \frac{di_{sd}}{dt} \qquad u_{sq,I} = r_s' \cdot i_{sq} + \frac{x_\sigma}{\omega_n} \cdot \frac{di_{sq}}{dt}$$
$$u_{sz1,I} = r_s \cdot i_{sz1} + \frac{x_{s\sigma}}{\omega_n} \cdot \frac{di_{sz1}}{dt} \qquad u_{sz2,I} = r_s \cdot i_{sz2} + \frac{x_{s\sigma}}{\omega_n} \cdot \frac{di_{sz2}}{dt} \tag{4.9}$$

whereas the decoupling (feed-forward) terms are

$$u_{sd,II} = -f_k \cdot x_\sigma \cdot i_{sq} - \frac{\psi_R}{T_r \cdot \omega_n} \qquad u_{sq,II} = f_k \cdot x_\sigma \cdot i_{sd} + n \cdot \psi_R$$
$$u_{sz1,II} = f_k \cdot x_{s\sigma} \cdot i_{sz2} \qquad u_{sz2,II} = -f_k \cdot x_{s\sigma} \cdot i_{sz1} \tag{4.10}$$

To explain the design procedure of the current controllers, the d-axis current control loop is considered. Using Laplace transform on the d-axis equation in (4.9) gives

$$\frac{i_{sd}(s)}{u_{sd}(s)} = \frac{1/r_s'}{1 + T_s'' \cdot s} \tag{4.11}$$

where $T_s'' = \frac{x_\sigma}{\omega_n \cdot r_s'}$

The d-axis current control loop considering analog control system is shown in Figure 4.3. The time delay in the controller is taken into account in the control loop. The time delay introduced by the current filter is also included; it is equal to the filter time constant. The decoupling term can be considered as a disturbance in the control system design [38]. The type of controller used is of PI type.

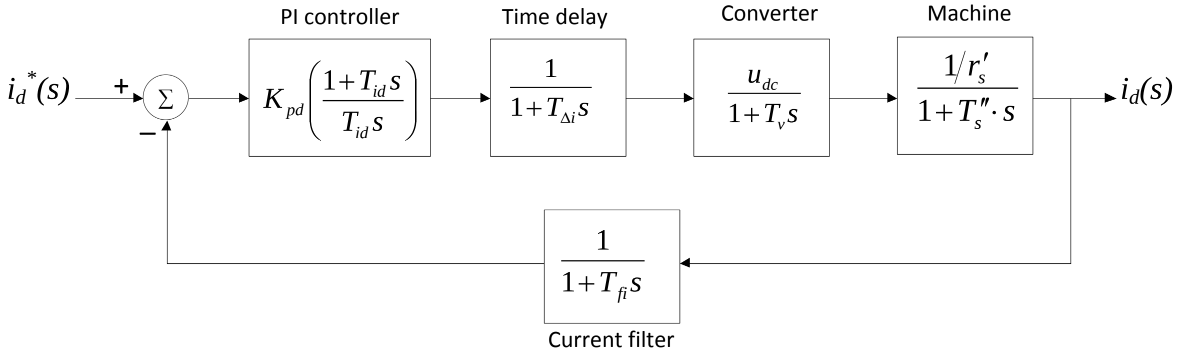

Figure 4.3: d-axis current control loop in SSFC

The plant transfer function is given as

$$G_p(s)=\frac{u_{dc}}{1+T_v\cdot s}\cdot\frac{1/r_s'}{1+T_s''\cdot s}\cdot\frac{1}{1+T_{f,i}s}\cdot\frac{1}{1+T_{\Delta,i}\cdot s}$$

$$G_p(s)\approx\frac{1/r_s'}{\left(1+T_s''\cdot s\right)\cdot\left(1+T_{sum,i}\cdot s\right)} \qquad \text{where } T_{sum,i}=T_v+T_{f,i}+T_{\Delta,i} \tag{4.12}$$

To avoid the dependence of the control parameters on the DC link voltage u_{dc}, a serial gain equal to the inverse of u_{dc} can be used at the output of the PI controller [39]. This is equivalent to disregarding the term u_{dc} in the plant transfer function when a conventional PI controller is used.

Digital control is used in the actual implementation of the system. Hence, the control is done in discrete time whereas the plant is a continuous time system. Such a system can be represented by the block diagram in Figure 4.4 [40]. For discrete-time analysis of the system considered in this thesis, the PWM of the inverter is assumed to have the function of a zero order hold [41]. The analog-to-digital converter (ADC) is the sampler in the system.

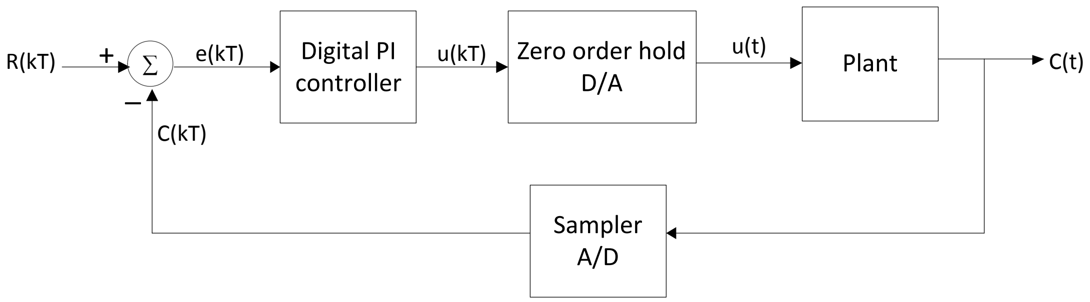

Figure 4.4: Discrete-time control of a continuous system

The frequency domain representation of the discrete-time system can be obtained using the Z-transform, resulting in the block diagram in Figure 4.5: Frequency domain equivalent of digital controller and continuous plant.

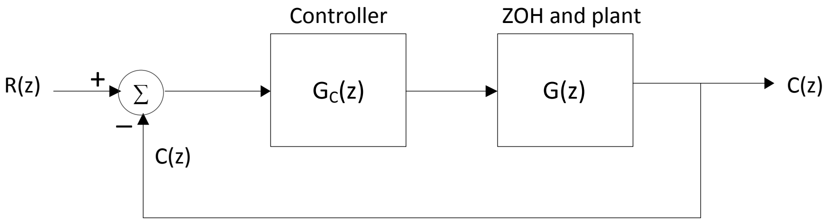

Figure 4.5: Frequency domain equivalent of digital controller and continuous plant

The pulse transfer function of the digital PI controller in *z*-domain is given by

$$G_C(z) = K_p + \frac{K_i}{1 - z^{-1}} \qquad \text{where } K_i = \frac{K_p}{T_i} \tag{4.13}$$

The pulse transfer function of the plant is the Z-transform of the plant preceded by a zero order hold [40].

$$G(z) = \mathcal{Z}\left(\frac{1 - e^{-Ts}}{s} \cdot G_p(s) \right) \tag{4.14}$$

In order to apply conventional frequency response design methods, the transfer function in the *z* plane is transformed into that in the *w* plane. The *w* transformation is a bilinear transformation defined by

$$z = \frac{1 + (T/2) \cdot w}{1 - (T/2) \cdot w} \tag{4.15}$$

where *T* is the sampling time of the discrete-time control system under consideration. Once the transfer function is transformed into *w* plane, it may be treated as a conventional transfer function in *w*. Conventional frequency response design techniques, including Bode diagrams, can then be used to design the discrete-time control system [40].

From (4.12), (4.14) and (4.15), the plant transfer function for the d-axis current can be obtained. This results in the following transfer function in *w* plane [39]:

$$G(w) = \frac{\frac{1}{r_s'} \cdot \left(1 - \frac{T_{samp,i}}{2} \cdot w\right) \cdot \left(1 + \frac{T_s'' \cdot T_{sum}}{T_s'' - T_{sum}} \cdot (\gamma_{sum} - \gamma_s') \cdot w\right)}{(1 + \gamma_s' \cdot T_s'' \cdot w) \cdot (1 + \gamma_{sum} \cdot T_{sum} \cdot w)} \tag{4.16}$$

$$\text{where } \gamma_{sum} \approx 1 - \frac{T_{samp,i}}{2 \cdot T_{sum}}, \qquad \gamma_s' \approx 1 - \frac{T_{samp,i}}{2 \cdot T_s''}$$

The PI controller using *w* transformation is obtained as

$$G_C(w) = K_p \cdot \left(\frac{1 + T_i \cdot w}{T_i \cdot w}\right) \tag{4.17}$$

Thus the transfer function of the PI controller in *w* plane is the same as in the *s* plane [39].

The open loop transfer function of the d-axis current control loop is then given by combining (4.16) and (4.17).

$$h_{od}(w) = K_{p,d} \cdot \left(\frac{1 + T_{i,d} \cdot w}{T_{i,d} \cdot w}\right) \cdot \frac{\frac{1}{r_s'} \cdot \left(1 - \frac{T_{samp,i}}{2} \cdot w\right) \cdot \left(1 + \frac{T_s'' \cdot T_{sum}}{T_s' - T_{sum}} \cdot (\gamma_{sum} - \gamma_s') \cdot w\right)}{(1 + \gamma_s' \cdot T_s'' \cdot w) \cdot (1 + \gamma_{sum} \cdot T_{sum} \cdot w)} \tag{4.18}$$

The *s* domain plant transfer function in (4.12) has two time constants in the denominator: a very small $T_{sum,i}$ and a relatively large T_s''. Therefore, the modulus optimum technique can be used to design the controller for this system [42], [43]. Using modulus optimum criterion for a digital control system in (4.18), the parameters of the digital PI controller are determined as follows [39]:

$$K_{p,d} = \frac{T_s'' - \frac{T_{samp,i}}{2}}{\frac{1}{r_s'} \cdot (2T_{sum} + T_{samp,i})} \qquad T_{i,d} = T_s'' - \frac{T_{samp,i}}{2} \tag{4.19}$$

Using similar procedure, the parameters of the *q*- , z_1- and z_2-axis current controllers are obtained as

$$K_{p,q} = \frac{T_s'' - \frac{T_{samp,i}}{2}}{\frac{1}{r_s'} \cdot \left(2T_{sum} + T_{samp,i}\right)} \qquad T_{i,q} = T_s'' - \frac{T_{samp,i}}{2}$$

$$K_{p,z1} = \frac{T_z - \frac{T_{samp,i}}{2}}{\frac{1}{r_s} \cdot \left(2T_{sum} + T_{samp,i}\right)} \qquad T_{i,z1} = T_z - \frac{T_{samp,i}}{2} \tag{4.20}$$

$$K_{p,z2} = \frac{T_z - \frac{T_{samp,i}}{2}}{\frac{1}{r_s} \cdot \left(2T_{sum} + T_{samp,i}\right)} \qquad T_{i,z2} = T_z - \frac{T_{samp,i}}{2}$$

$$\text{where} \quad T_z = \frac{x_{s\sigma}}{\omega_n \cdot r_s}$$

As mentioned earlier, torque control of the machine is achieved using control of the q-axis current. From the torque equation of the machine in (4.1) and the stator flux expressions in (4.4), it can be shown that

$$m_e = \psi_R \cdot i_{sq} \tag{4.21}$$

The flux in the machine is normally kept constant at its rated value, i.e. when the machine is not in flux weakening mode. Thus the torque is proportional to the q-axis current, and torque control is achieved using this relationship.

The simplified transfer function for the closed control loop of q-axis current is given in *s* domain as

$$i_{sq}(s) = \frac{1}{\left(1 + T_{eq,i} \cdot s\right)} \cdot i_{sq}^*(s) \tag{4.22}$$
$$\text{where} \quad T_{eq,i} = 2 \cdot T_{sum,i}$$

Hence, the transfer function for the torque control is [39]

$$m_e(s) = \psi_R \cdot i_{sq}(s) = \psi_R \cdot \frac{1}{\left(1 + T_{eq,i} \cdot s\right)} \cdot i_{sq}^*(s) = \psi_R \cdot \frac{1}{\left(1 + T_{eq,i} \cdot s\right)} \cdot \frac{m_e^*(s)}{\psi_R}$$
$$m_e(s) = \frac{1}{\left(1 + T_{eq,i} \cdot s\right)} \cdot m_e^*(s) \tag{4.23}$$

which can be transformed to *w* domain using the procedure explained earlier. For digital implementation, the time constant in the transfer function is [41]

$$T_{eq,i} = 2 \cdot \left(T_{sum,i} + \frac{T_{samp,i}}{2}\right) \tag{4.24}$$

4.2.3 Design of Flux Controller

The flux model is used to derive the transfer function of the flux control loop. Using Laplace transform on the rotor flux magnitude equation in (4.5) gives

$$\frac{\psi_R(s)}{i_{sd}(s)} = \frac{x_H}{1+T_r \cdot s} \tag{4.25}$$

The continuous time equivalent of the flux control loop is given in Figure 4.6. The inner d-axis current control loop has been represented by an equivalent time constant.

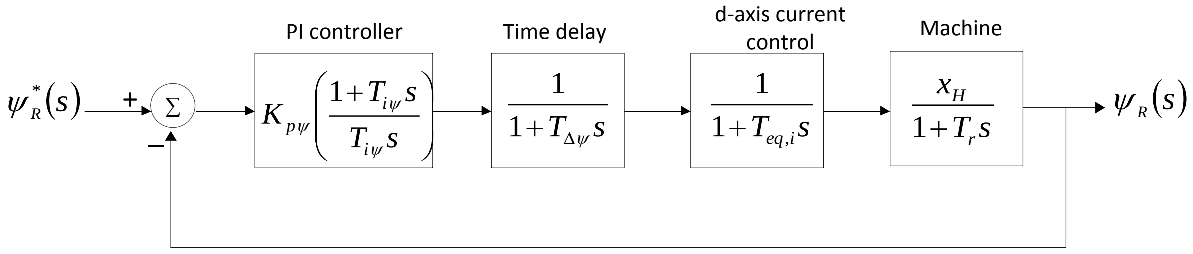

Figure 4.6: Flux control loop

The open loop transfer of the plant in continuous domain is

$$\begin{aligned} G_{p,\psi}(s) &= \frac{x_H}{(1+T_r \cdot s)} \cdot \frac{1}{(1+T_{eq,i} \cdot s)} \cdot \frac{1}{(1+T_{\Delta,\psi} \cdot s)} \\ G_{p,\psi}(s) &\approx \frac{x_H}{(1+T_s \cdot s)\cdot(1+T_{sum,\psi} \cdot s)} \\ &\text{where} \quad T_{sum,\psi} = T_{eq,i} + T_{\Delta,\psi} \end{aligned} \tag{4.26}$$

The plant transfer function has one large and one small time constant. Thus it is suited for modulus optimum design technique [42], [43]. Using a similar design technique in *w*-domain as in section 4.2.2, the digital PI controller parameters are obtained as

$$K_{p,\psi} = \frac{T_r - \frac{T_{samp,\psi}}{2}}{2 \cdot x_H \left(T_{sum,\psi} + \frac{T_{samp,\psi}}{2}\right)} \qquad T_{id} = T_r - \frac{T_{samp,\psi}}{2} \tag{4.27}$$

4.2.4 Design of Speed Controller

The speed control loop in *s* domain can be represented by the block diagram in Figure 4.7. The inner torque (q-axis current) control loop can be taken as almost ideal, but with a small time delay, since it is designed with a bandwidth ten times that of the outer (speed) control loop. It is represented by the transfer function in (4.23). The time delays in digital speed controller and speed filter are taken into account. The load torque is considered as a disturbance and disregarded in the controller design. The mechanical system equation in (4.1) is used to derive the relation between the electromagnetic torque and the speed.

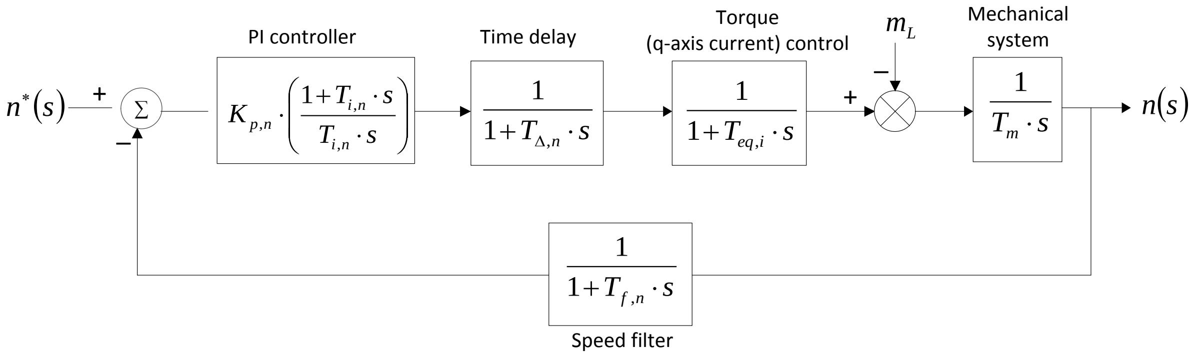

Figure 4.7: Speed control loop

The open loop transfer of the plant in *s* domain is

$$
\begin{aligned}
G_{p,n}(s) &= \frac{1}{T_m\cdot s}\cdot\frac{1}{\left(1+T_{eq,i}\cdot s\right)}\cdot\frac{1}{\left(1+T_{f,n}\cdot s\right)}\cdot\frac{1}{\left(1+T_{\Delta,n}\cdot s\right)} \\
G_{p,n}(s) &\approx \frac{1}{T_m\cdot s\cdot\left(1+T_{sum,n}\cdot s\right)} \qquad (4.28) \\
\text{where}\quad T_{sum,n} &= T_{eq,i}+T_{f,n}+T_{\Delta,\psi}
\end{aligned}
$$

Using the *w* transform on the continuous system preceded by a ZOH and adding a digital PI controller gives the open loop transfer function of the speed control loop as follows [39]:

$$
\begin{aligned}
h_{o,n}(w) &= K_{p,n}\cdot\left(\frac{1+T_{i,n}\cdot w}{T_{i,n}\cdot w}\right)\cdot\frac{\left(1-\frac{T_{samp,n}}{2}\cdot w\right)\cdot\left(1+\left(\gamma_{sum,n}-1\right)\cdot T_{sum,n}\cdot w\right)}{T_m\cdot w\cdot\left(1+\gamma_{sum,n}\cdot T_{sum,n}\cdot w\right)} \qquad (4.29) \\
\text{where}\quad \gamma_{sum,n} &= 1-\frac{T_{samp,n}}{2\cdot T_{sum,n}}
\end{aligned}
$$

The plant transfer function in (4.28) implies that symmetric optimum technique can be used to design the controller [42], [43]. For a digital controller, the parameters are based on the transfer function in (4.29) [39]. ~~check~~

$$
K_{pd} = \frac{T_m}{\left(2T_{sum,n}+T_{samp,n}\right)} \qquad T_{i,n} = 4\cdot\left(T_{sum,n}+\frac{T_{samp,n}}{2}\right) \qquad (4.30)
$$

Note: Tm here is variable cuz variable load, hence Jtot varies … online estimation can be used…

4.3 Double Synchronous Frame Control

4.3.1 Introduction

The model of six-phase induction machine in double synchronous frame was developed in chapter 2.3. Double synchronous frame control of the machine can be achieved based on this model. The per-unit equations describing the model were obtained as follows:

$$\begin{aligned}
u_{sd1} &= r_s \cdot i_{sd1} + \frac{1}{\omega_n} \cdot \frac{d\psi_{sd1}}{dt} - f_k \cdot \psi_{sq1} & \qquad u_{sq1} &= r_s \cdot i_{sq1} + \frac{1}{\omega_n} \cdot \frac{d\psi_{sq1}}{dt} + f_k \cdot \psi_{sd1} \\
u_{sd2} &= r_s \cdot i_{sd2} + \frac{1}{\omega_n} \cdot \frac{d\psi_{sd2}}{dt} - f_k \cdot \psi_{sq2} & u_{sq2} &= r_s \cdot i_{sq2} + \frac{1}{\omega_n} \cdot \frac{d\psi_{sq2}}{dt} + f_k \cdot \psi_{sd2} \\
0 &= r_r \cdot i_{rd} + \frac{1}{\omega_n} \cdot \frac{d\psi_{rd}}{dt} - f_r \cdot \psi_{rq} & 0 &= r_r \cdot i_{rq} + \frac{1}{\omega_n} \cdot \frac{d\psi_{rq}}{dt} + f_r \cdot \psi_{rd} \\
\psi_{sd1} &= x_s \cdot i_{sd1} + x_h \cdot i_{sd2} + x_h \cdot i_{rd} & \psi_{sq1} &= x_s \cdot i_{sq1} + x_h \cdot i_{sq2} + x_h \cdot i_{rq} \\
\psi_{sd2} &= x_s \cdot i_{sd2} + x_h \cdot i_{sd1} + x_h \cdot i_{rd} & \psi_{sq2} &= x_s \cdot i_{sq2} + x_h \cdot i_{sq1} + x_h \cdot i_{rq} \\
\psi_{rd} &= x_r \cdot i_{rd} + x_h \cdot i_{sd1} + x_h \cdot i_{sd2} & \psi_{rq} &= x_r \cdot i_{rq} + x_h \cdot i_{sq1} + x_h \cdot i_{sq2} \\
m_e &= \psi_{sd1} \cdot i_{sq1} - \psi_{sq1} \cdot i_{sd1} + \psi_{sd2} \cdot i_{sq2} - \psi_{sq2} \cdot i_{sd2} \\
T_m \cdot \frac{dn}{dt} &= m_e - m_L
\end{aligned} \tag{4.31}$$

Rotor field oriented control is used, and thus the d-axis is aligned with the rotor flux linkage space vector. This gives

$$\psi_{rd} = \psi_r \,, \qquad \psi_{rq} = 0, \qquad \frac{d\psi_{rq}}{dt} = 0 \tag{4.32}$$

Using these substitutions in the rotor flux linkage equations and solving for the rotor currents yields

$$i_{rd} = \frac{\psi_r - x_h \cdot i_{sd1} - x_h \cdot i_{sd2}}{x_r}, \qquad i_{rq} = \frac{-x_h \cdot i_{sq1} - x_h \cdot i_{sq2}}{x_r} \tag{4.33}$$

The stator flux linkages can then be expressed as

$$\begin{aligned}
\psi_{sd1} &= x_\sigma \cdot i_{sd1} + (x_\sigma - x_{s\sigma}) \cdot i_{sd2} + \psi_R & \qquad \psi_{sq1} &= x_\sigma \cdot i_{sq1} + (x_\sigma - x_{s\sigma}) \cdot i_{sq2} \\
\psi_{sd2} &= x_\sigma \cdot i_{sd2} + (x_\sigma - x_{s\sigma}) \cdot i_{sd1} + \psi_R & \psi_{sq2} &= x_\sigma \cdot i_{sq2} + (x_\sigma - x_{s\sigma}) \cdot i_{sq1}
\end{aligned} \tag{4.34}$$

where $x_\sigma = x_s - \dfrac{x_h^2}{x_r}$ $\qquad \psi_R = \dfrac{x_h}{x_r} \cdot \psi_r = \dfrac{\psi_r}{1 + \sigma_r}$

The current model is used to determine the rotor flux vector magnitude and position as explained in chapter 4.2.1. For DSFC, the equations of this model are obtained as

$$\begin{aligned} \frac{d\psi_R}{dt} &= -\frac{\psi_R}{T_r} + \frac{x_H}{T_r} \cdot \left(i_{sd1} + i_{sd2}\right) \\ f_r &= \frac{x_H \cdot \left(i_{sq1} + i_{sq2}\right)}{T_r \cdot \omega_n \cdot \psi_R} \end{aligned} \tag{4.35}$$

where $x_H = \frac{x_h}{1+\sigma_r}$ $\quad T_r = \frac{x_r}{\omega_n \cdot r_r}$ $\quad \sigma_r = \frac{x_{r\sigma}}{x_h}$

4.3.2 Design of Inner Controllers

The inner control structure in DSFC is shown in Figure 4.8. The measured stator currents are converted to the (d_1, q_1) and (d_2, q_2) reference frame. The current control and decoupling are implemented in this reference frames, giving voltage references in (d_1, q_1) and (d_2, q_2) frames. Using inverse Park transform, the voltage references in (d_1, q_1) and (d_2, q_2) frames are used to compute the control voltages for the PWM operation of the two inverters.

The d_1- and d_2-axis currents are used to control the flux in the machine, and the q_1- and q_2-axis currents control the torque.

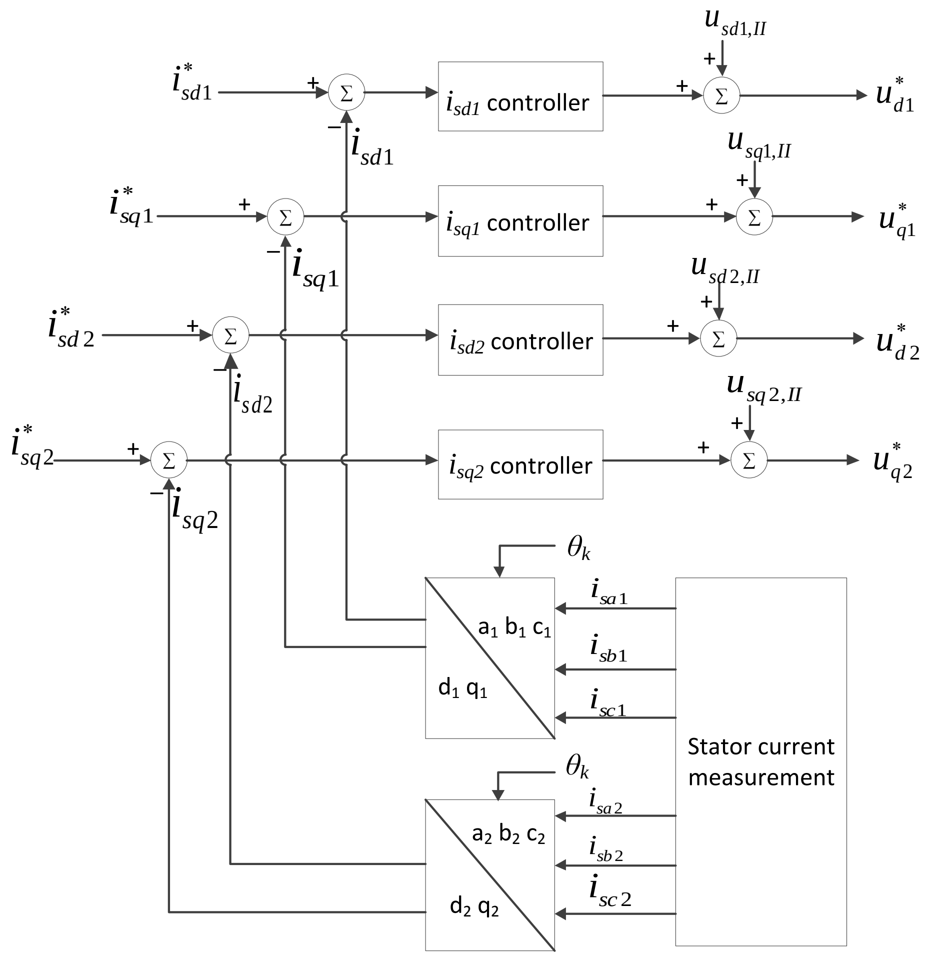

Figure 4.8: Double synchronous frame current control

The stator voltage equations are used to develop the transfer function used in the control of currents. In the derivation here, the equations of the stator d_1 and q_1 axes are developed first. Taking the u_{sd1} equation in (4.31) and replacing ψ_{sd1} and ψ_{sq1} from (4.34) gives

$$\begin{aligned} u_{sd1} &= r_s \cdot i_{sd1} + \frac{x_\sigma}{\omega_n} \cdot \frac{di_{sd1}}{dt} + \frac{(x_\sigma - x_{s\sigma})}{\omega_n} \cdot \frac{di_{sd2}}{dt} \\ &+ \frac{1}{\omega_n} \cdot \frac{d\psi_R}{dt} - f_k \cdot x_\sigma \cdot i_{sq1} - f_k \cdot (x_\sigma - x_{s\sigma}) \cdot i_{sq2} \end{aligned} \qquad (4.36)$$

To control the current i_{sd1} using u_{sd1}, the dynamic term containing i_{sd2} in (4.36) is replaced using other suitable terms. This can be done by replacing i_{sd2} using the ψ_{sd2} equation in (4.34), replacing ψ_{sd2} using the u_{sd2} equation in (4.31), and then replacing ψ_{sq2} from (4.34). The derivation results in

$$
\begin{aligned}
u_{sd1} = {} & r_s \cdot i_{sd1} + \frac{x_\sigma}{\omega_n} \cdot \left(1 - \left(\frac{x_\sigma - x_{s\sigma}}{x_\sigma} \right)^2 \right) \frac{di_{sd1}}{dt} + \frac{(x_\sigma - x_{s\sigma})}{x_\sigma} \cdot u_{sd2} - \frac{(x_\sigma - x_{s\sigma})}{x_\sigma} \cdot r_s \cdot i_{sd2} \\
& + \frac{x_{s\sigma}}{x_\sigma \cdot \omega_n} \cdot \frac{d\psi_R}{dt} - f_k \cdot x_\sigma \cdot \left(1 - \left(\frac{x_\sigma - x_{s\sigma}}{x_\sigma} \right)^2 \right) \cdot i_{sq1}
\end{aligned}
\tag{4.37}
$$

Substitution of $\frac{d\psi_R}{dt}$ from the flux model in (4.35), and introduction of some new terms gives

$$
u_{sd1} = r_s' \cdot i_{sd1} + \frac{x_s'}{\omega_n} \cdot \frac{di_{sd1}}{dt} + \frac{u_{sd2}}{1+\sigma_s'} - \frac{r_s''}{1+\sigma_s'} \cdot i_{sd2} - \frac{\sigma_s'}{1+\sigma_s'} \cdot \frac{\psi_R}{\omega_n \cdot T_r} - f_k \cdot x_s' \cdot i_{sq1}
$$

$$
\begin{aligned}
\text{where} \quad & \sigma_s' = \frac{x_{s\sigma}}{x_\sigma - x_{s\sigma}} \qquad x_s' = x_\sigma \cdot \left(1 - \left(\frac{x_\sigma - x_{s\sigma}}{x_\sigma} \right)^2 \right) = x_\sigma \cdot \left(1 - \frac{1}{(1+\sigma_s')^2} \right) \\
& r_s' = r_s + \frac{x_{s\sigma}}{x_\sigma} \cdot r_R = r_s + \frac{\sigma_s'}{1+\sigma_s'} \cdot r_R \qquad r_s'' = r_s - \frac{x_{s\sigma}}{x_\sigma - x_{s\sigma}} \cdot r_R = r_s - \sigma_s' \cdot r_R \\
& r_R = \frac{x_H}{\omega_n \cdot T_r} = \frac{r_r}{(1+\sigma_r)^2}
\end{aligned}
\tag{4.38}
$$

Using a similar procedure, the u_{sq1} equation is obtained as

$$
u_{sq1} = r_s \cdot i_{sq1} + \frac{x_s'}{\omega_n} \cdot \frac{di_{sq1}}{dt} + \frac{u_{sq2}}{1+\sigma_s'} - \frac{r_s}{1+\sigma_s'} \cdot i_{sq2} + \frac{\sigma_s'}{1+\sigma_s'} \cdot f_k \cdot \psi_R + f_k \cdot x_s' \cdot i_{sd1} \tag{4.39}
$$

The first f_k in (4.39) can be replaced by $(f_r + n)$, and f_r is again substituted from the flux model given in (4.35). This gives

$$
u_{sq1} = r_s' \cdot i_{sq1} + \frac{x_s'}{\omega_n} \cdot \frac{di_{sq1}}{dt} + \frac{u_{sq2}}{1+\sigma_s'} - \frac{r_s''}{1+\sigma_s'} \cdot i_{sq2} + \frac{\sigma_s'}{1+\sigma_s'} \cdot n \cdot \psi_R + f_k \cdot x_s' \cdot i_{sd1} \tag{4.40}
$$

The equations for the stator d_2 and q_2 axes are obtained using similar derivations. The derived equations are

$$
u_{sd2} = r_s' \cdot i_{sd2} + \frac{x_s'}{\omega_n} \cdot \frac{di_{sd2}}{dt} + \frac{u_{sd1}}{1+\sigma_s'} - \frac{r_s''}{1+\sigma_s'} \cdot i_{sd1} - \frac{\sigma_s'}{1+\sigma_s'} \cdot \frac{\psi_R}{\omega_n \cdot T_r} - f_k \cdot x_s' \cdot i_{sq2} \tag{4.41}
$$

$$
u_{sq2} = r_s' \cdot i_{sq2} + \frac{x_s'}{\omega_n} \cdot \frac{di_{sq2}}{dt} + \frac{u_{sq1}}{1+\sigma_s'} - \frac{r_s''}{1+\sigma_s'} \cdot i_{sq1} + \frac{\sigma_s'}{1+\sigma_s'} \cdot n \cdot \psi_R + f_k \cdot x_s' \cdot i_{sd2} \tag{4.42}
$$

From (4.38), (4.40), (4.41) and (4.42), the control equations can be identified as

$$
\begin{aligned}
u_{sd1,I} &= r_s' \cdot i_{sd1} + \frac{x_s'}{\omega_n} \cdot \frac{di_{sd1}}{dt} \\
u_{sd2,I} &= r_s' \cdot i_{sd2} + \frac{x_s'}{\omega_n} \cdot \frac{di_{sd2}}{dt} \\
u_{sq1,I} &= r_s' \cdot i_{sq1} + \frac{x_s'}{\omega_n} \cdot \frac{di_{sq1}}{dt} \\
u_{sq2,I} &= r_s' \cdot i_{sq2} + \frac{x_s'}{\omega_n} \cdot \frac{di_{sq2}}{dt}
\end{aligned}
\tag{4.43}
$$

And the decoupling terms are

$$
\begin{aligned}
u_{sd1,II} &= \frac{u_{sd2}}{1+\sigma_s'} - \frac{r_s''}{1+\sigma_s'} \cdot i_{sd2} - \frac{\sigma_s'}{1+\sigma_s'} \cdot \frac{\psi_R}{\omega_n \cdot T_r} - f_k \cdot x_s' \cdot i_{sq1} \\
u_{sd2,II} &= \frac{u_{sd1}}{1+\sigma_s'} - \frac{r_s''}{1+\sigma_s'} \cdot i_{sd1} - \frac{\sigma_s'}{1+\sigma_s'} \cdot \frac{\psi_R}{\omega_n \cdot T_r} - f_k \cdot x_s' \cdot i_{sq2} \\
u_{sq1,II} &= \frac{u_{sq2}}{1+\sigma_s'} - \frac{r_s}{1+\sigma_s'} \cdot i_{sq2} + \frac{\sigma_s'}{1+\sigma_s'} \cdot f_k \cdot \psi_R + f_k \cdot x_s' \cdot i_{sd1} \\
u_{sq2,II} &= \frac{u_{sq1}}{1+\sigma_s'} - \frac{r_s''}{1+\sigma_s'} \cdot i_{sq1} + \frac{\sigma_s'}{1+\sigma_s'} \cdot n \cdot \psi_R + f_k \cdot x_s' \cdot i_{sd2}
\end{aligned}
\tag{4.44}
$$

The equations in (4.43) are used to derive the transfer functions of the control loops and design the PI controllers. The d_1-axis current control loop in s domain can be represented as in Figure 4.9.

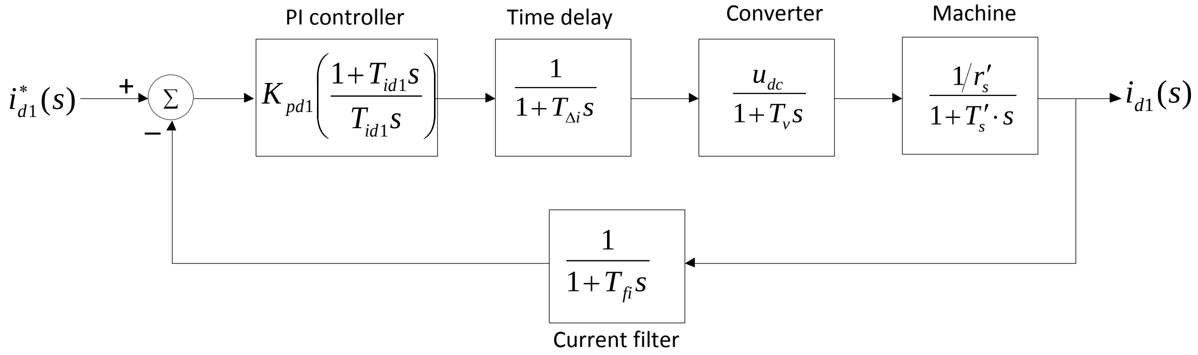

Figure 4.9: d_1-axis current control loop in DSFC

The plant transfer function for d_1-axis current control is

$$
\begin{aligned}
G_p(s) &= \frac{u_{dc}}{1+T_v \cdot s} \cdot \frac{1/r_s'}{1+T_s' \cdot s} \cdot \frac{1}{1+T_{f,i}s} \cdot \frac{1}{1+T_{\Delta,i} \cdot s} \qquad \text{where } T_s' = \frac{x_s'}{\omega_n \cdot r_s'} \\
G_p(s) &\approx \frac{1/r_s'}{(1+T_s'' \cdot s) \cdot (1+T_{sum,i} \cdot s)} \qquad \text{where } T_{sum,i} = T_v + T_{f,i} + T_{\Delta,i}
\end{aligned}
\tag{4.45}
$$

It is evident that the d_1- axis current control loop in DSFC is similar to the d-axis loop of SSFC in Figure 4.3, except for the difference in the stator time constant. Thus the same design technique used in chapter 4.2.2 applies here. The same goes for the other current controllers.

Using similar procedure, the parameters of the q- , z_1- and z_2-axis current controllers are obtained as

$$
\begin{aligned}
K_{p,d1} &= \frac{T_s' - \frac{T_{samp,i}}{2}}{\frac{1}{r_s'} \cdot \left(2T_{sum} + T_{samp,i}\right)} & \qquad T_{i,d1} &= T_s' - \frac{T_{samp,i}}{2} \\
K_{p,q1} &= \frac{T_s' - \frac{T_{samp,i}}{2}}{\frac{1}{r_s'} \cdot \left(2T_{sum} + T_{samp,i}\right)} & \qquad T_{i,q1} &= T_s' - \frac{T_{samp,i}}{2} \\
K_{p,d2} &= \frac{T_s' - \frac{T_{samp,i}}{2}}{\frac{1}{r_s'} \cdot \left(2T_{sum} + T_{samp,i}\right)} & \qquad T_{i,d2} &= T_s' - \frac{T_{samp,i}}{2} \\
K_{p,q2} &= \frac{T_s' - \frac{T_{samp,i}}{2}}{\frac{1}{r_s'} \cdot \left(2T_{sum} + T_{samp,i}\right)} & \qquad T_{i,q2} &= T_s' - \frac{T_{samp,i}}{2}
\end{aligned}
\tag{4.46}
$$

Calculated parameters

From the torque equation and flux linkage equations in (4.31), the torque can be expressed in terms of rotor quantities as

$$
m_e = \frac{\psi_{rq} \cdot i_{rd} - \psi_{rd} \cdot i_{rq}}{2} \tag{4.47}
$$

Substituting for the rotor currents from (4.33) into (4.47), replacing for the rotor flux linkages from (4.32),

$$
\begin{gathered}
m_e = \psi_R \cdot \left(\frac{i_{sq1} + i_{sq2}}{2}\right) = \left(\psi_R \cdot \frac{i_{sq1}}{2}\right) + \left(\psi_R \cdot \frac{i_{sq2}}{2}\right) \\
\text{where} \quad \psi_R = \frac{x_h}{x_r} \cdot \psi_r
\end{gathered}
\tag{4.48}
$$

Therefore, torque control can be achieved by controlling the q_1- and q_2-axis currents, and similar design method used in torque control of SSFC applies here. This can also be verified using the equivalence relation between the two different models resulting in

$$m_e = \psi_R \cdot i_{sq}$$

$$\text{where} \quad i_{sq} = \frac{i_{sq1} + i_{sq2}}{2} \tag{4.49}$$

which is exactly the same equation as in equation (4.21) of the SSFC method.

4.3.3 Design of Flux Controller

Taking the equation for the rotor flux linkage magnitude from the flux model equations in (4.35), and applying Laplace transform gives

$$\psi_R(s) = \frac{x_H \cdot \left(i_{sd1}(s) + i_{sd2}(s)\right)}{1 + T_r \cdot s}$$

$$\psi_R(s) = \frac{x_H \cdot i_{sd1}(s)}{1 + T_r \cdot s} + \frac{x_H \cdot i_{sd2}(s)}{1 + T_r \cdot s} \tag{4.50}$$

implying that the flux can be controlled using the d$_1$- and d$_2$-axis currents.

From the equivalence relations between the two models, it can be shown that

$$\frac{\psi_R(s)}{i_{sd}(s)} = \frac{x_H}{1 + T_r \cdot s}$$

$$\text{where} \quad i_{sd} = \frac{i_{sd1} + i_{sd2}}{2} \quad \textit{and} \quad x_H = x_H^I = 2 \cdot x_H^{II} \quad \text{or use} \quad x_{H,I} \tag{4.51}$$

This is the same as the *s* domain flux equation of SSFC. In addition, both d$_1$-axis and d$_2$-axis current references are kept equal in normal conditions, also making them equal to the equivalent d-axis reference. Thus the flux control can be designed by replacing both d$_1$-axis and d$_2$-axis inner control loops by one equivalent time constant. The parameters of the flux controller are found to be the same as that of SSFC designed in chapter 4.2.3.

4.3.4 Design of Speed Controller

Speed control of the machine is achieved by using the torque (inner) controller. The torque control in DSFC, as seen from outer control, is the same as that of SSFC. This was discussed in section 4.3.2. Both modelling methods have the same mechanical system equations relating the speed and torque of the machine. Therefore, it can be concluded that the speed controllers in DSFC and SSFC are exactly the same.

5 Experimental Setup of Six-Phase Motor Drive

5.1 Hardware Setup

In this chapter the experimental setup of a six-phase induction motor drive used in the thesis is presented. The setup consists of various hardware and software components. The hardware setup and components are discussed in this section. The software implementation, including the software environment and program structure, is explained in chapter 5.2.

5.1.1 Setup Overview

The high-level schematic of the laboratory setup is shown in Figure 5.1. The setup is the same as the one used in [11]. The main hardware components are a six-phase induction machine, a DC machine connected to load resistors, two 3-phase inverters, two diode rectifiers, a three-phase variable transformer, an FPGA (Field Programmable Gate Array) control card, current and voltage sensors, rotary pulse encoder, and a PC.

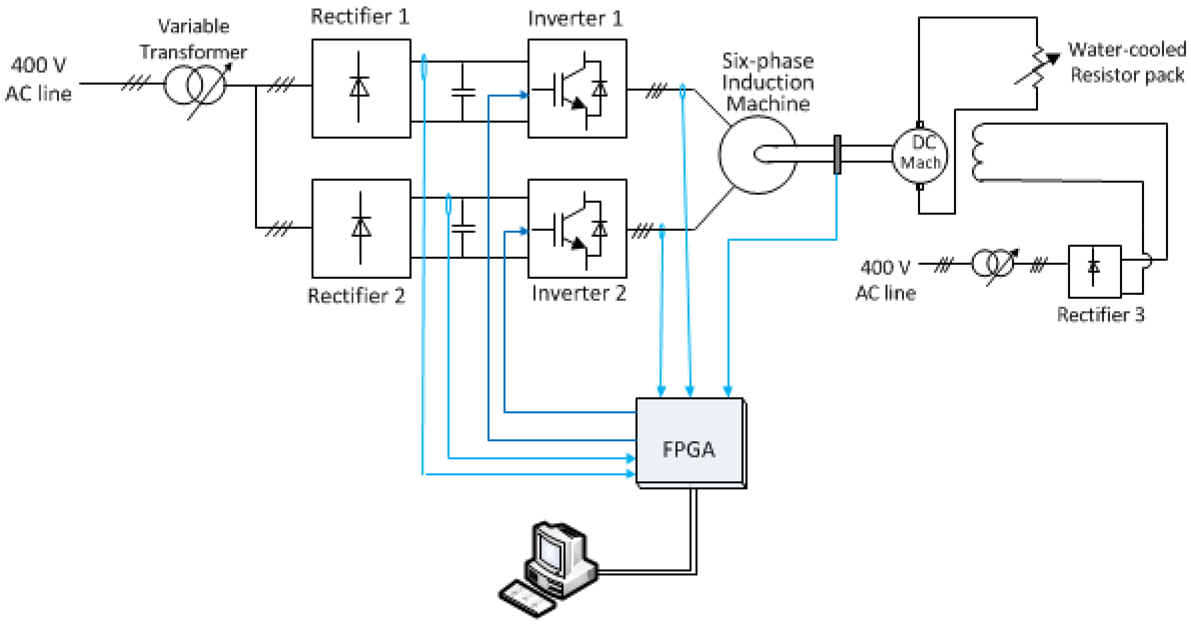

Figure 5.1: Schematic of six-phase motor drive lab setup

The six-phase induction machine is supplied from two switch-mode inverters with separate DC link voltages. Two diode rectifiers are used to obtain the DC link voltages. The AC input to the rectifiers can be varied using the three-phase transformer, thus varying the DC link voltage as needed. The DC machine is directly connected on the same shaft to the six-phase induction machine. Water-cooled resistors are connected to the DC machine armature. The PC is used to program the control system into the FPGA control board. Real-time monitoring is also done using software in the PC. The assembled drive is shown in Figure 5.2.

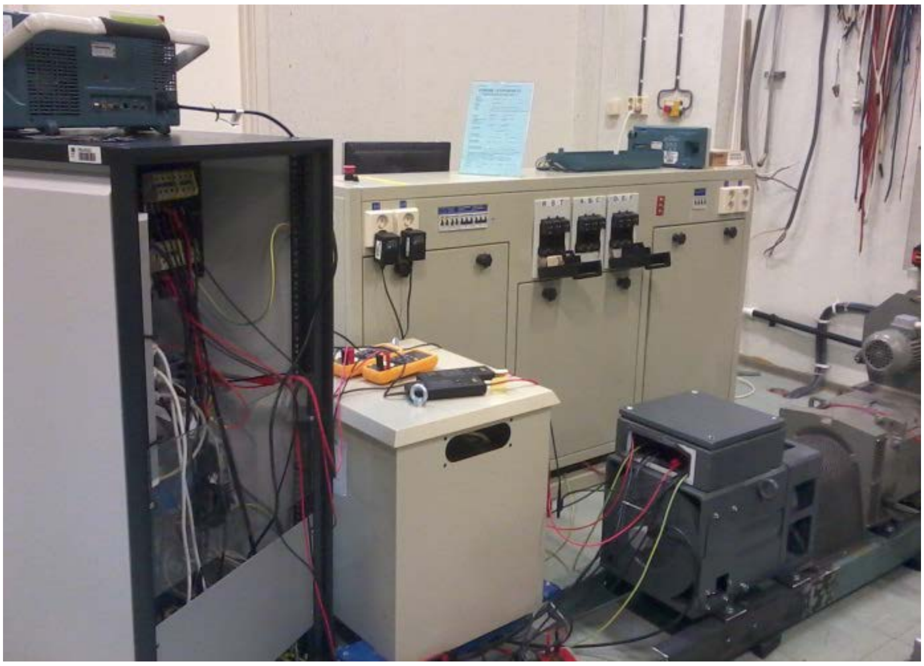

Figure 5.2: Assembly of six-phase motor drive

5.1.2 Six-Phase Induction Machine

The six-phase induction machine used in the experiment has two 3-phase stator winding groups, separated by 30 electrical degrees in space. The machine has a squirrel-cage rotor. Figure 5.3 shows the external view and terminals of the machine.

Figure 5.3: Six-phase induction machine (a) external view, (b) stator terminals

The rated power output of the machine is 11.7 kW. The nameplate data and parameters of the machine are given in Appendix A.

5.1.3 DC Machine

A separately excited DC machine is mounted on the same shaft as the six-phase induction machine. The armature of the DC machine is connected to load resistors.

In the experimental setup the DC machine with the load resistors is used as a load, and thus operates as a DC generator. The load can be varied either by changing the value of the load resistors or by varying the field voltage (excitation) of the DC machine. The six-phase induction machine is operated as a motor, and acts as prime mover as viewed from the DC machine.

5.1.4 Converters

Two three-phase diode rectifiers are used to convert the AC line voltage into DC. The rectifiers can take voltage input of 0 – 400 V rms. The current rating is 63 A. The DC voltage output range is 0 – 540 V. The front view of one rectifier is shown in Figure 5.4.

Figure 5.4: Rectifier module

Two three-phase IGBT inverters connected to the two rectifier modules are used to supply the six-phase induction machine. The power rating of the inverters is 20 kW. The DC voltage input can be 0 – 650 V, and switching frequency in the range of 0 – 25 kHz can be used. The allowable current depends on the DC input and switching frequency. At 500 V DC and 10 kHz switching frequency, the maximum allowable current is 50 A. The capacitor bank inside the modules is 3300 µF. The control signal for the gate drivers is 5 V CMOS. The inverter modules have capacitive and RC snubbers [45].

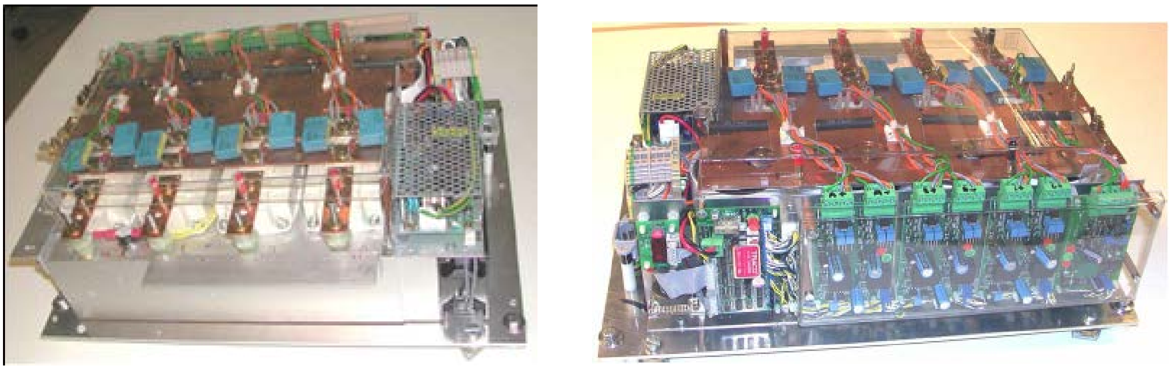
(a) (b)

Figure 5.5: Inverter module (a) output side, (b) driver card side [45]

5.1.5 FPGA Control Board

The processor board is designed for use in converter control system based on Xilinx Virtex 5 FXT FPGA. The main parts of the board are shown in Figure 5.6. The main features of the processor board can be summarized as follows [46]:

- Based on Xilinx Virtex5: XC5V FX30T. FPGA with PowerPC processor.
- Memory: 256 MB DRAM (DDR2), 128 MB Flash and 64 kB EEPROM.
- Analog to Digital Converter (ADC): 8 × 12 bit, 40 MSPS
- Digital to Analog Converter (DAC): 4 × 12 bit, 20 MSPS
- Digital Input-Output: 3 × 16 bit TTL, 3 × 2 LVDS signal pair
- Communication ports: RS232, USB, Ethernet and CAN.
- Contains circuitry of IP (Intellectual Property) modules, including interface modules and signal processing modules.
- Interface for LEM current transducers, pulse encoder and converter drivers.

The IP modules are developed using Xilinx Embedded Development Kit (EDK). Time critical operations are handled by these IP modules. The interface IP modules consist of AD converter serial signal interface, DA converter interface, pulse encoder interface and inverter interface. The signal processing modules are accumulator filter block, PI regulator, angle transformation, pulse width modulator and comparator limiter. The IP modules for PI regulator and angle transformation are not used in this implementation. These are implemented as software in the PowerPC processor.

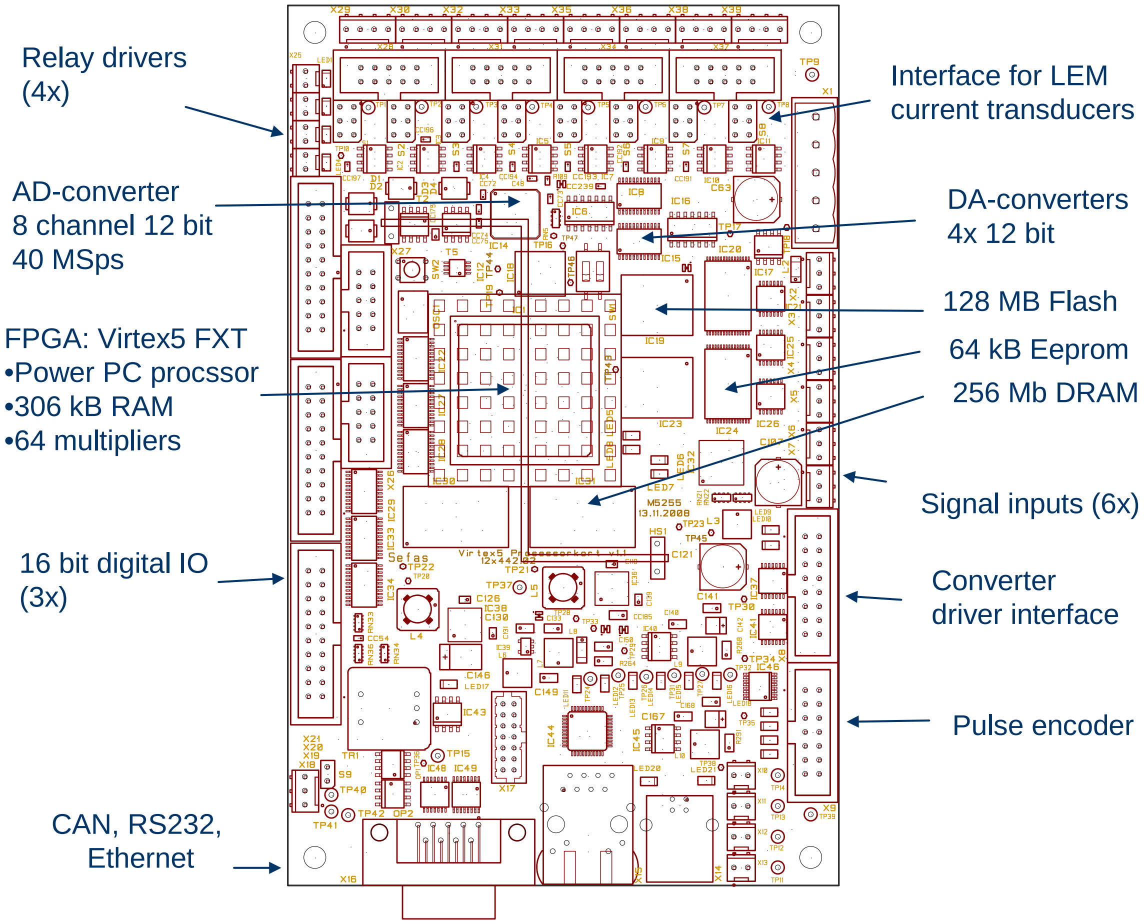

Figure 5.6: Main parts of the FPGA processor board [47]

5.1.6 Current, Voltage and Speed Measurements

The measurement of stator line currents is done using LEM Current Transducer LA 205-S. It is a closed loop current transducer using the Hall Effect. It has a primary nominal rms current of 200 A, and a secondary nominal rms current of 100 mA. Thus, the conversion ratio is 1:2000 [48].

The DC link voltages are measured using LEM Voltage Transducer LV 25-600, which is based on the Hall Effect. The primary nominal rms voltage of the transducer is 600 V, and the secondary nominal rms current is 25 mA. The conversion ratio is 600 V / 25 mA [49].

Rotor position measurement is done using Heidenhain ERN-420 rotary encoder. It is an incremental pulse encoder providing TTL signals that give information about the angular position of the rotor. Initial angle detection and counting of the pulses is necessary to determine the absolute position of the rotor. The rotor speed is computed as the rate of change of the angular position [50].

5.2 Software Implementation

In this section the software implementation of six-phase motor drive control is described concisely. The software environment used and the program flow are discussed.

5.2.1 Software Environment

The software environment used to implement the control system is Xilinx C/C++ Software Development Kit (SDK). A screenshot of the SDK is shown in Figure 5.7. The programming language used in this implementation is C++.

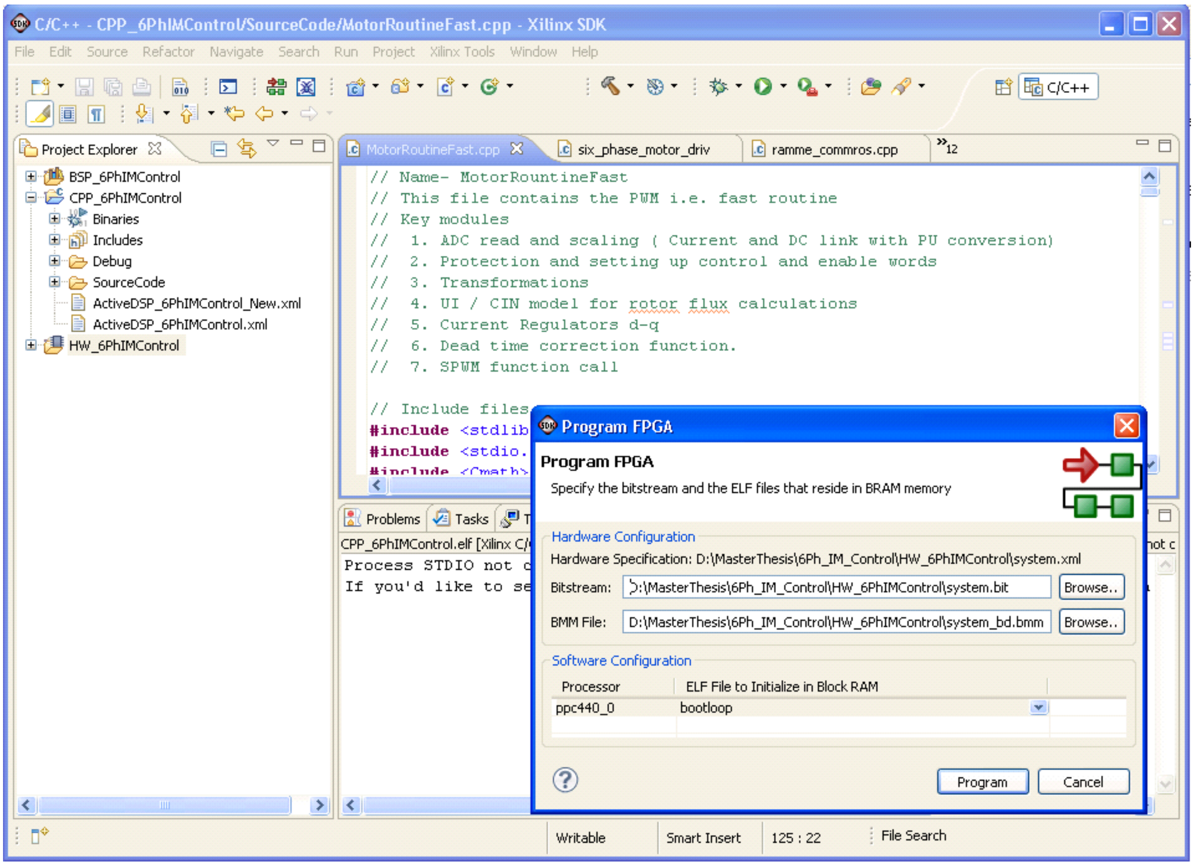

```
// Name- MotorRountineFast
// This file contains the PWM i.e. fast routine
// Key modules
//   1. ADC read and scaling ( Current and DC link with PU conversion)
//   2. Protection and setting up control and enable words
//   3. Transformations
//   4. UI / CIN model for rotor flux calculations
//   5. Current Regulators d-q
//   6. Dead time correction function.
//   7. SPWM function call

// Include files
#include <stdlib
#include <stdio.
#include <Cmath>
```

CPP_6PhIMControl.elf [Xilinx C/

```
Process STDIO not c
If you'd like to se
```

Program FPGA

Specify the bitstream and the ELF files that reside in BRAM memory

Hardware Configuration

Hardware Specification: D:\MasterThesis\6Ph_IM_Control\HW_6PhIMControl\system.xml

Bitstream: D:\MasterThesis\6Ph_IM_Control\HW_6PhIMControl\system.bit

BMM File: D:\MasterThesis\6Ph_IM_Control\HW_6PhIMControl\system_bd.bmm

Software Configuration

Processor	ELF File to Initialize in Block RAM
ppc440_0	bootloop

Figure 5.7: Xilinx SDK

Computationally demanding but less time critical processes are written in the software and handled by the PowerPC processor in the FPGA. Time critical operations, on the other hand, are carried out using the dedicated IP modules as mentioned earlier. The control code together with the library of IP modules is programmed from the PC into the FPGA using a USB connection. The FPGA control system accepts measured inputs and control commands, giving control signals to the inverters as outputs.

Once the FPGA is programmed, real-time operation and monitoring of the drive is done using the ActiveDSP software on the PC. Figure 5.8 shows a screenshot of the software. The communication is done through the RS232 serial cable connected to the computer.

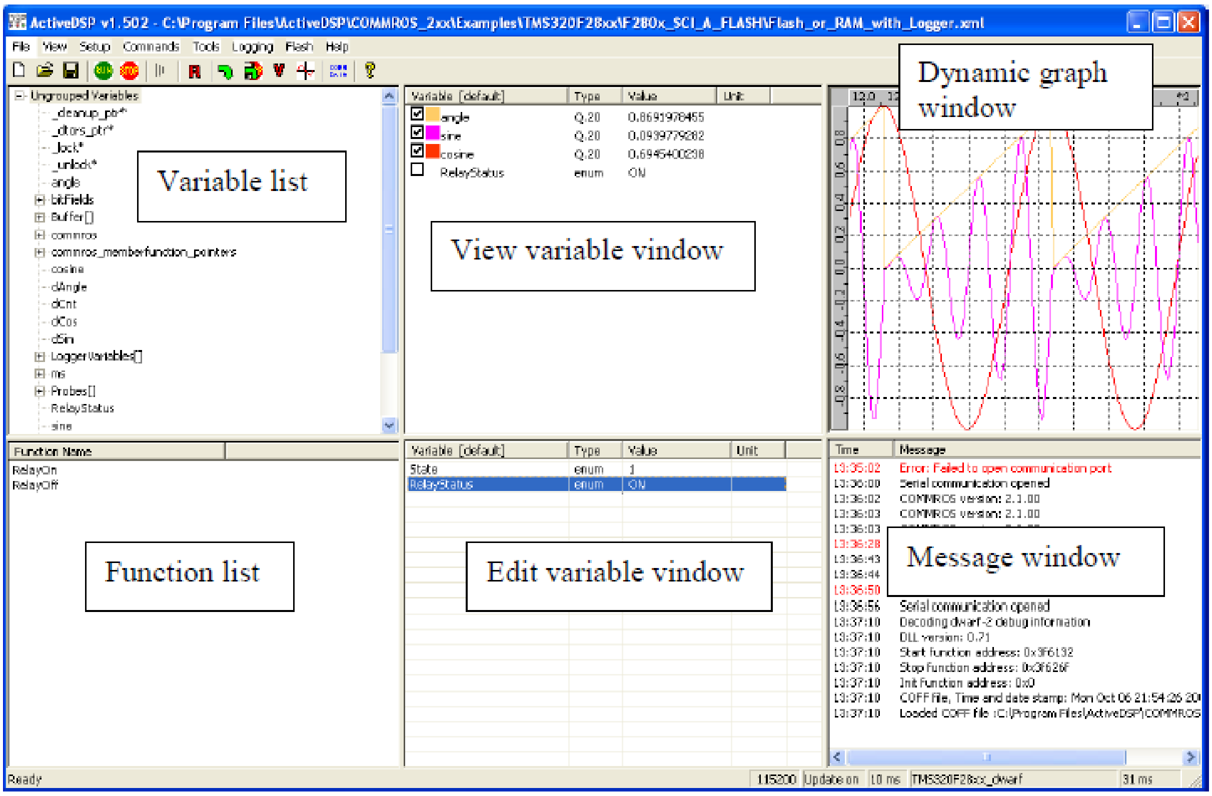

	Variable [default]	Type	Value	Unit
☑	🟧 angle	Q.20	0.8691978455	
☑	🟪 sine	Q.20	0.0939779282	
☑	🟥 cosine	Q.20	0.6945400238	
☐	RelayStatus	enum	ON	

Variable [default]	Type	Value	Unit
State	enum	1	
RelayStatus	enum	ON	

```
Time      Message
13:35:02  Error: Failed to open communication port
13:36:00  Serial communication opened
13:36:02  COMMROS version: 2.1.00
13:36:03  COMMROS version: 2.1.00
13:36:03
13:36:28
13:36:43
13:36:44
13:36:50
13:36:56  Serial communication opened
13:37:10  Decoding dwarf-2 debug information
13:37:10  DLL version: 0.71
13:37:10  Start function address: 0x3F6132
13:37:10  Stop function address: 0x3F626F
13:37:10  Init Function address: 0x0
13:37:10  COFF file, Time and date stamp: Mon Oct 06 21:54:26 20
13:37:10  Loaded COFF file :C:\Program Files\ActiveDSP\COMMROS
```

Figure 5.8: ActiveDSP main window [51]

Using the ActiveDSP interface, control commands can be sent to the FPGA and data can be read from the FPGA and displayed in the graph window. Moreover, the software enables the real-time logging of data [51]. This data can be saved and processed using other software tools such as Matlab.

5.2.2 Program Structure

The program flow and interrupt routines of the drive control system are shown in Figure 5.9. The start routine initializes the system and sets up the interrupt mechanisms. The control system is implemented in two main interrupt service routines: the fast interrupt routine and the slow interrupt routine.

The fast routine handles tasks that should be executed as fast as possible. It interrupts once at every PWM switching period. Measurement and protection, flux model calculations, current control loops and modulation are implemented in this routine.

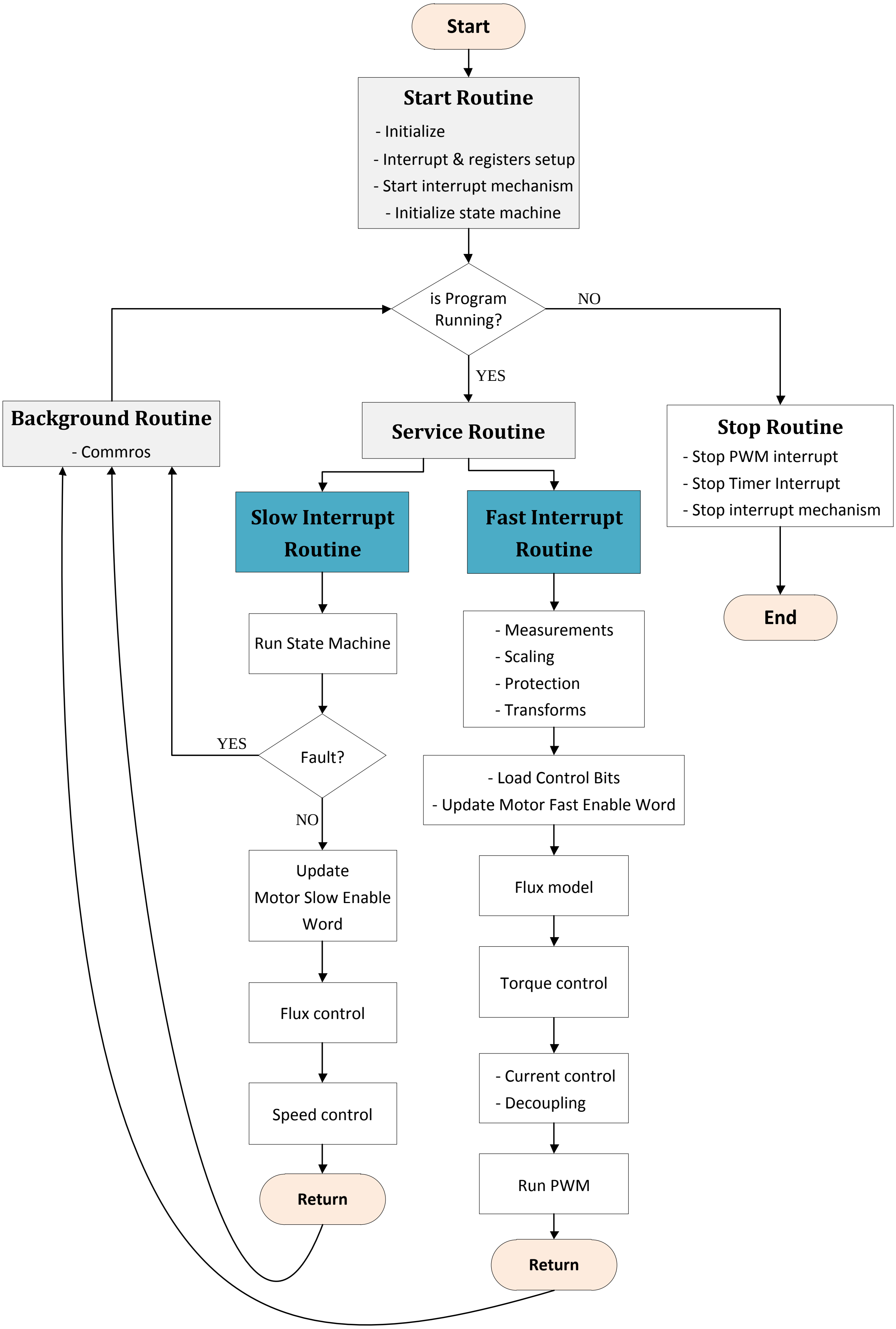

Figure 5.9: Program flow and Interrupts

In the slow routine, control tasks that are less time critical are executed. It uses a timer for the interrupt mechanism. The slow interrupt time is taken as ten times the fast interrupt time. Running of the state machine, and the outer flux and speed control are done in this routine.

5.2.3 State Machine

The state machine enables the program to accept commands and execute them when certain conditions are met. The drive system will be in a certain state determined by the operating conditions and status of the drive components. The sate machine, which is based on the DRIVECOM standard for drive controllers, is shown in Figure 5.10. This is basically the same state machine used in [11]. However, modification is made so that the drive can continue operation when there is fault in only one supply (DC link or inverter) while the other supply is healthy.

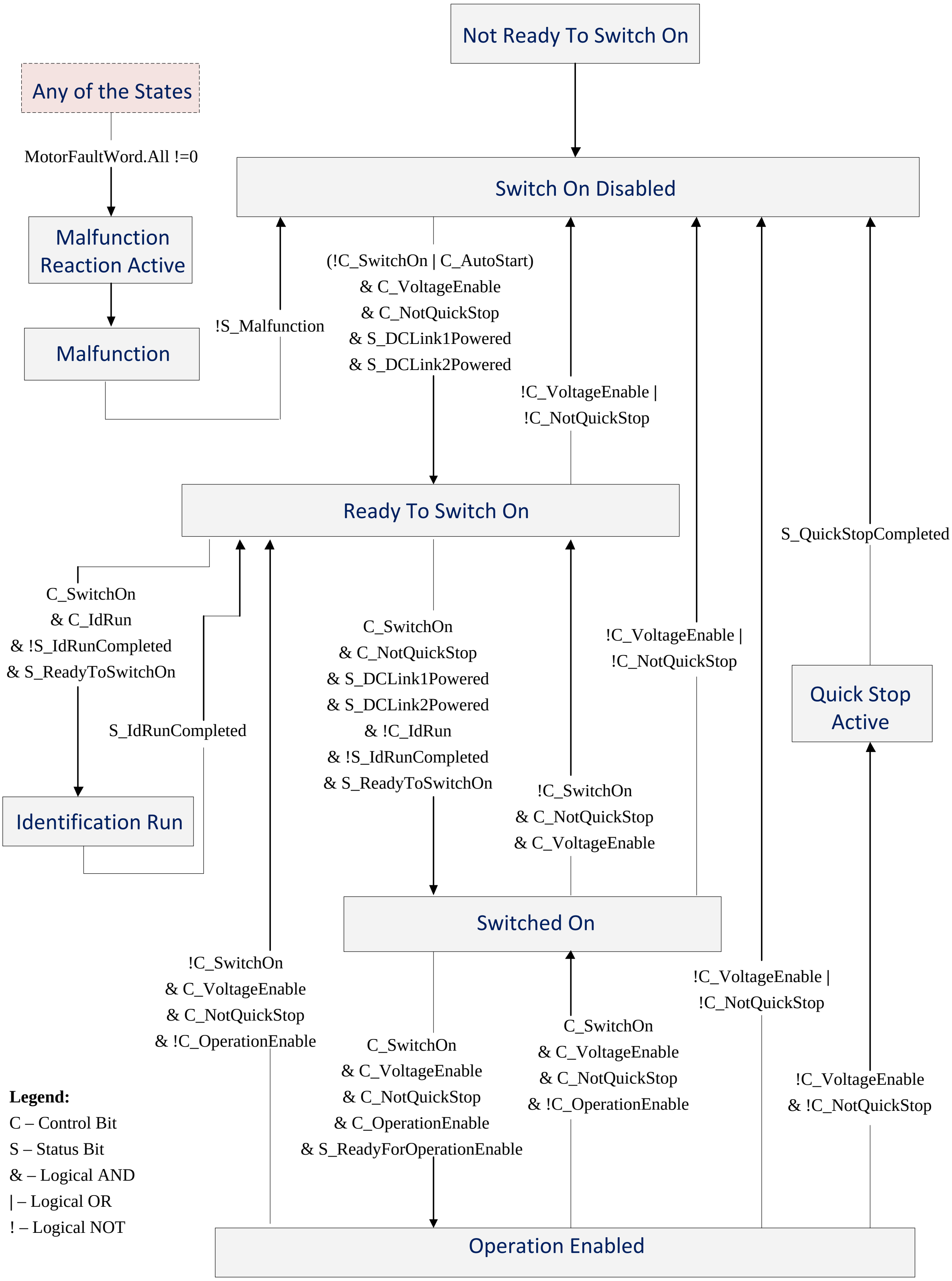

Figure 5.10: State machine of the six-phase motor drive

6 Simulation and Experimental Results

6.1 Introduction

In this chapter, the results of simulation and experimental work on the control of six-phase induction motor drive are presented. The aim of the work was to implement and test control of the drive during different operating conditions. Various normal and faulty cases can be considered to test the system. In this thesis, the following cases are of major interest:

1. Normal start-up and balanced operation,
2. Operation with current asymmetries between the two 3-phase groups of the machine,
3. Operation during supply asymmetries and faults, including low DC link voltage and loss of a DC link supply and/or an inverter.

After theoretical modelling and control design, simulations were carried out. Digital simulation was used in Matlab Simulink/SimPowerSystems. This was used initially to verify the control methods before laboratory testing. Then experimental testing was done in the laboratory setup described in chapter 5. The main results obtained in simulations and experiments match for the operation cases in normal conditions and current asymmetries. For the case of supply faults, desirable results were obtained in the experiments. However, the results in the simulations of six-phase induction machine were not as expected. It is also worth mentioning that desirable results were obtained in a simulation of six-phase permanent magnet machine for all operating conditions. But, the results are not included in this thesis due to limitation of the scope.

The parameters of the controllers in the system were determined in chapter 4. The theoretical values obtained have been tuned in the experiments to obtain better performance. The experimental values are given in appendix D.

The results presented in this chapter, except those designated as simulation result, are experimental results. Real-time data was obtained using trigger mechanism in ActiveDSP logger and plotted in Matlab. In the time axis of the plots, negative values show the data before triggering and positive values show the data after triggering. In this chapter, emphasis is given to the presentation of experimental results. Only few of the simulation results are included.

6.2 SSFC Results

6.2.1 Normal Operation

During normal operation of the drive, the two 3-phase groups in the machine are operated with equal current references and supply voltages. Thus the power and torque is equally shared between them. Due to the 30° displacement between the winding groups, quantities in phase 1 lead the corresponding quantities in phase 2 by 30°. The drive may be operated in either torque control mode or speed control mode.

Response of the inner controllers in simulation is shown in figure 6.1. Initially the magnetization of the machine is using a flux controller is simulated. Then, a step torque of 0.8 pu is applied at 0.5 sec.

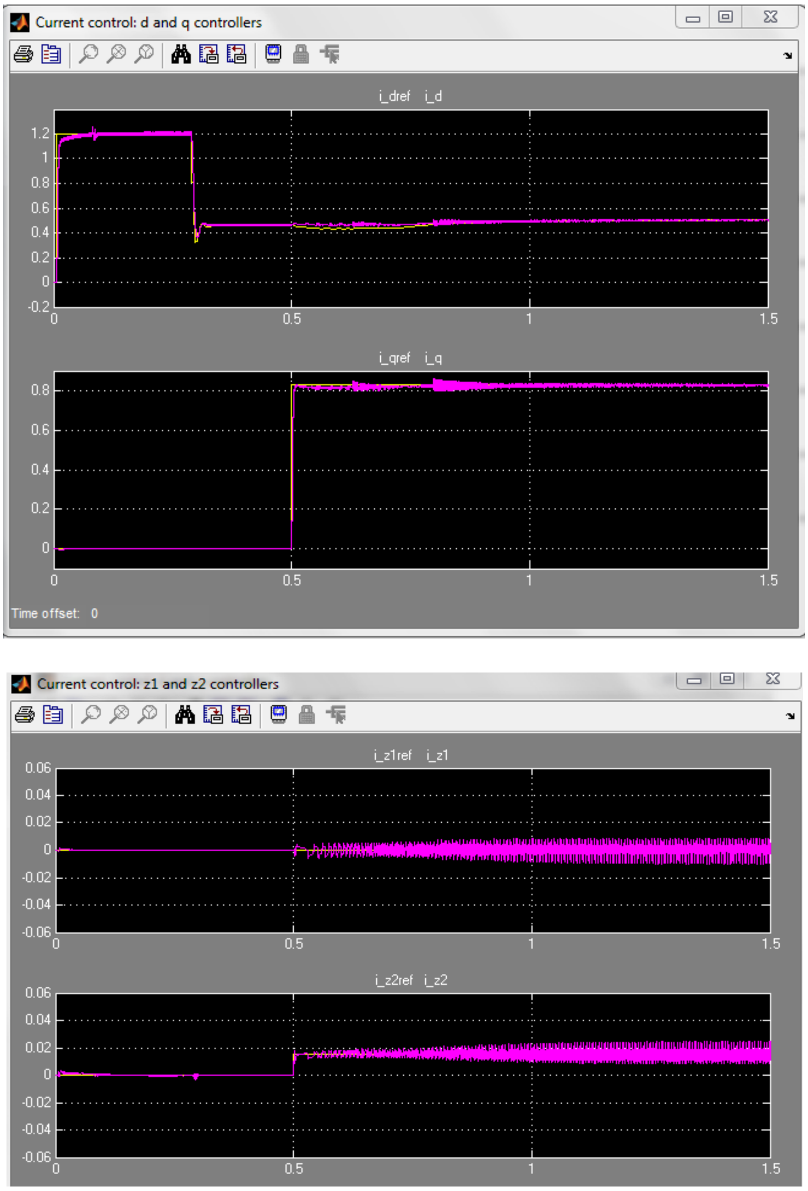

Figure 6.1: Simulation result: Response of current controllers during normal startup and operation

In the experimental test, the machine is initially magnetized along the stator a_1-axis by applying the rated flux reference. The flux control variable used is ψ_R as defined in equation (4.4) in chapter 4.2.1. Setting ψ_R to 0.95 pu gives a rated flux (ψ_r) of 1.0 pu. The response of the flux controller is shown Figure 6.2.

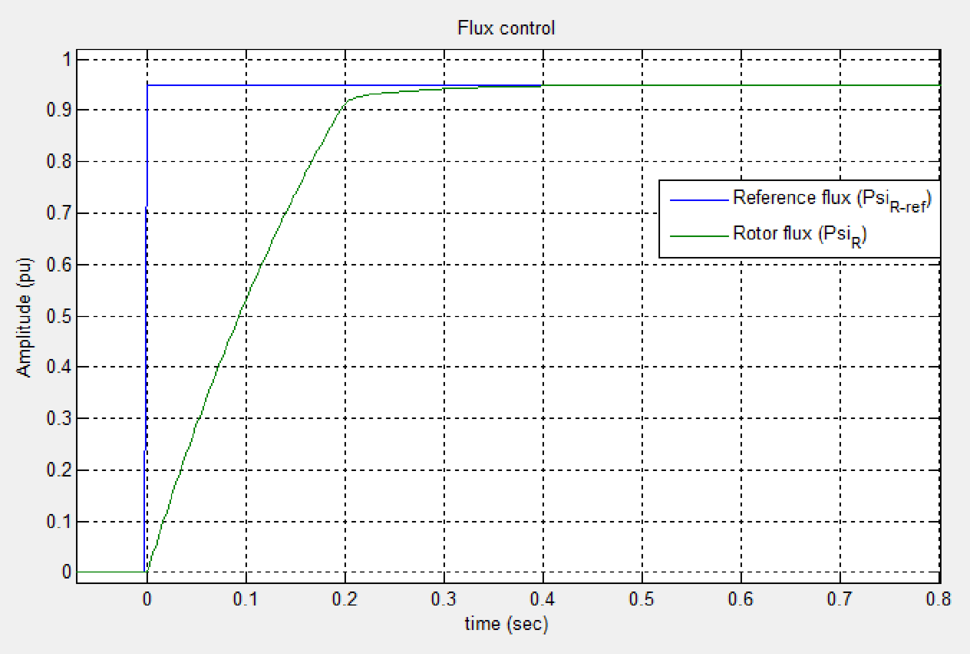

Figure 6.2: Flux controller response

Figure 6.3 shows the response of the inner d-axis current controller during the flux build-up in the machine. Until the flux reaches the rated value, the controller output is at the saturation limit, which is set to 1.02 pu. At steady state, the d-axis current needed to maintain the flux is approximately 0.508 pu. This is determined by the value of the mutual inductance as evident from the equations of the flux model.

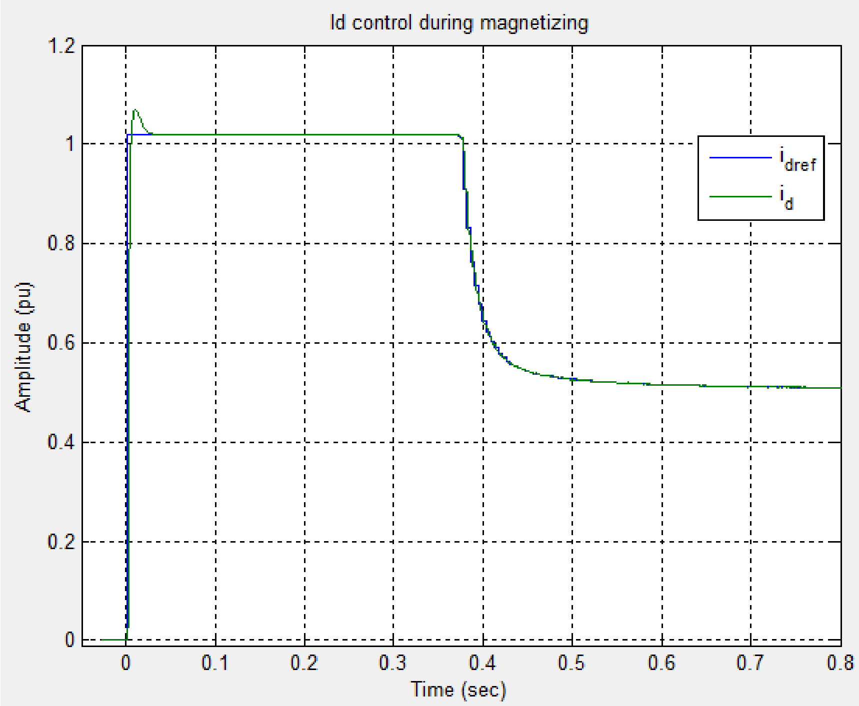

Figure 6.3: Inner d-axis current control during magnetization

After magnetizing, the machine can be started in either torque or speed control mode. Response of the inner controllers during start-up with a step torque reference of 0.6 pu is shown in Figure 6.4. The q-axis current reference is obtained as 0.6316 pu from the torque reference. The DC link voltage inputs of both inverters are equal with a value of 500 V.

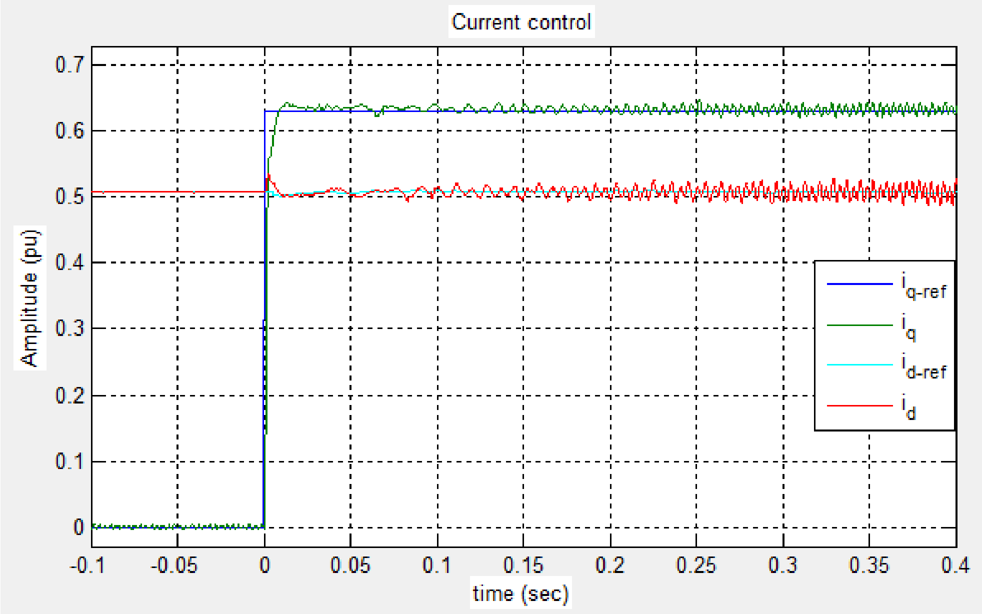

Figure 6.4: Start-up and torque control in SSFC

The machine stator phase currents during startup with 0.6 step torque are shown in Figure 6.4. The currents displayed in the figure are obtained after filtering using a two-point moving average filter, which is a low pass filter with cut-off frequency of ca. 1 kHz. From the magnitudes of the currents before start-up, it can be seen that the machine is magnetized along the stator a_1-axis.

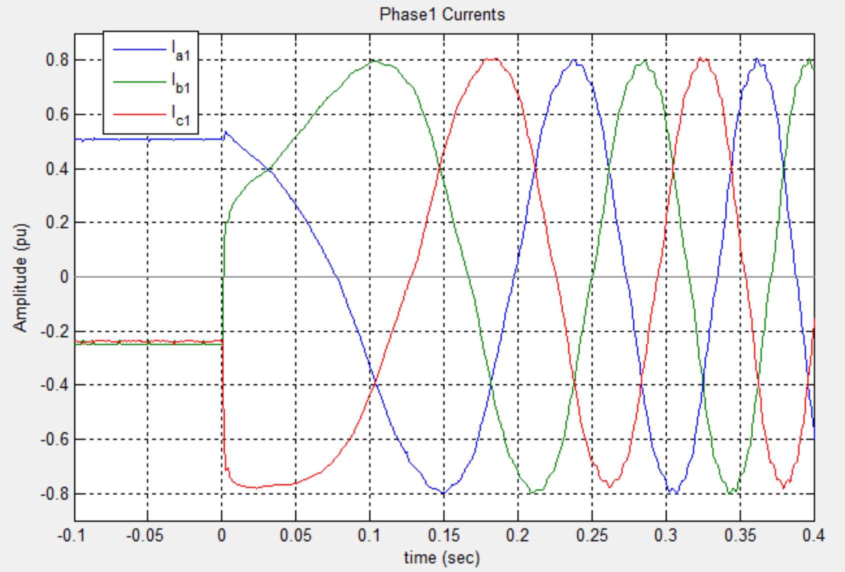

Figure 6.5: Phase group 1 currents during start-up

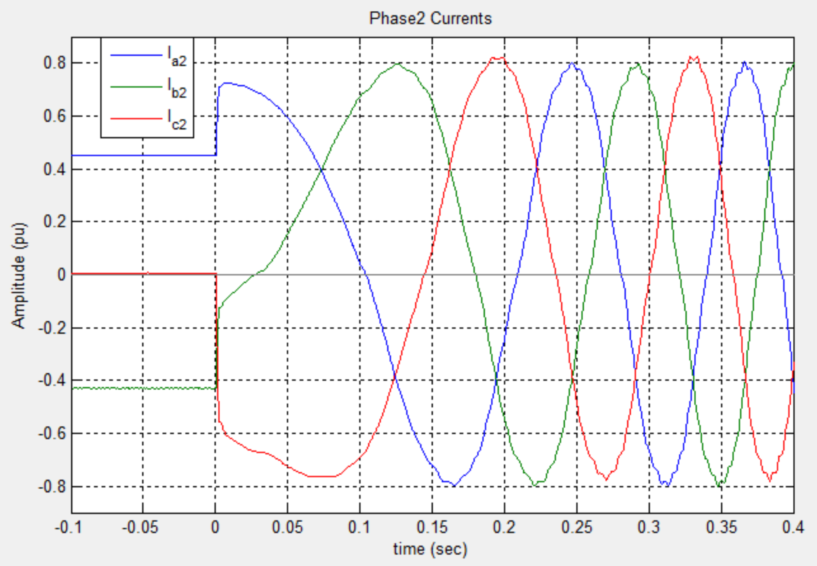

Figure 6.6: Phase group 2 currents during start-up

The measured stator currents are shown in the oscillogram in Figure 6.7. The currents of only phases a_1 and a_2 are shown. Both currents have the same amplitude and frequency, but i_{sa1} leads i_{sa2} by 30° as expected. The oscillograms of the inverter line voltages and the stator phase voltages are shown in Figure 6.8.

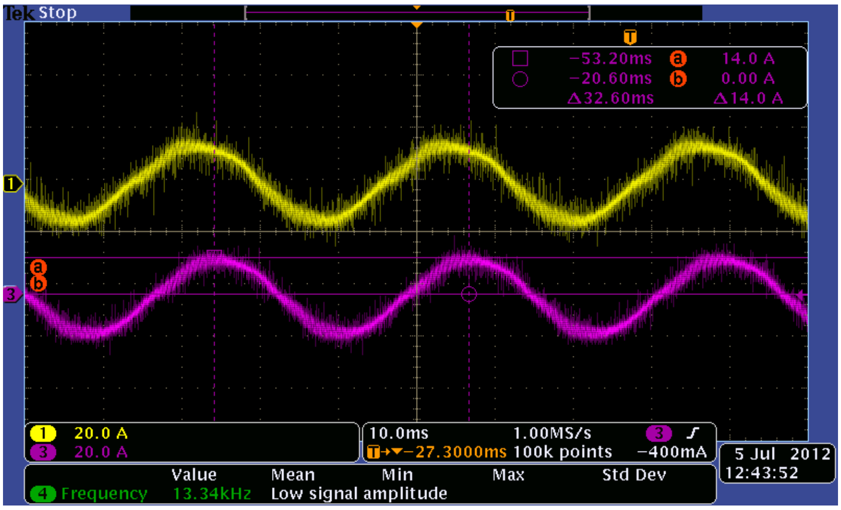

Figure 6.7: Oscillogram of stator currents [probe 1(yellow) - i_{sa1}, probe 3 (pink) - i_{sa2}]

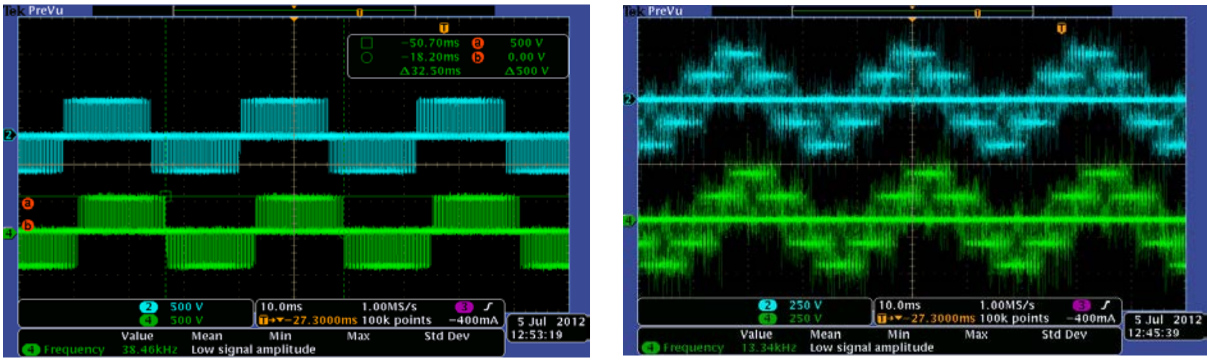

(a) **(b)**

Figure 6.8: Voltages (a) Line voltages – U_{sa1b1} and U_{sa2b2} , (b) Phase voltages – U_{sa1}, U_{sa2}

In another test case, the machine was started in speed control mode under no load. The field voltage of the DC machine was set to zero, thus the only load to the induction machine is the inertial mass of the shaft. A step input of 0.4 pu speed gave the response in Figure 6.9.

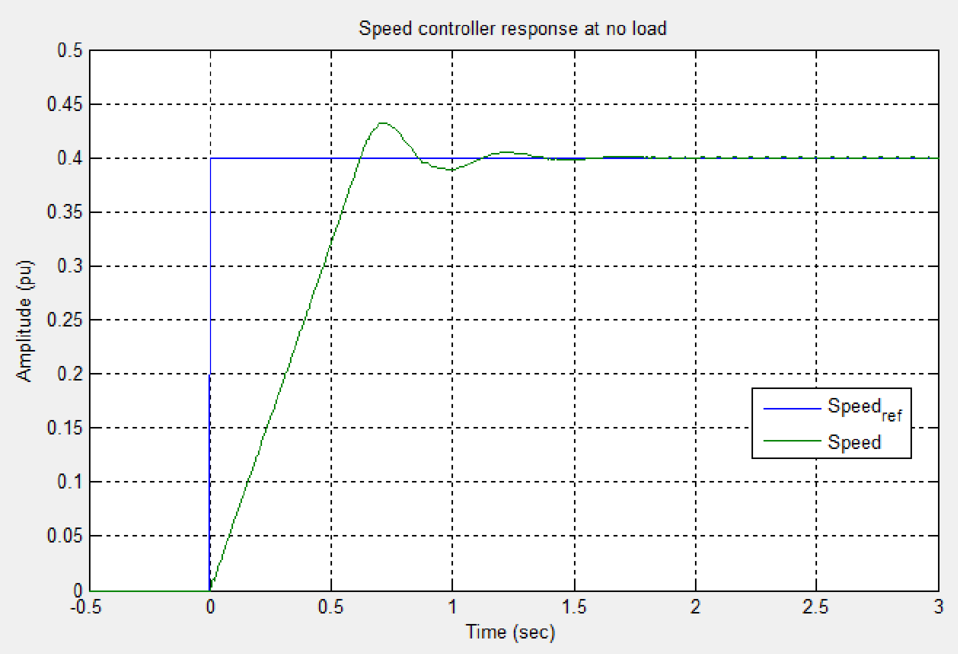

Figure 6.9: Speed controller response in no load

The response of the inner controllers during speed control is shown in Figure 6.10. It can be seen that the steady state electromagnetic torque and q-axis currents are small, just enough to rotate the rotor shaft and cover losses. The z_2-axis currents are also very small because both phase groups have the same currents.

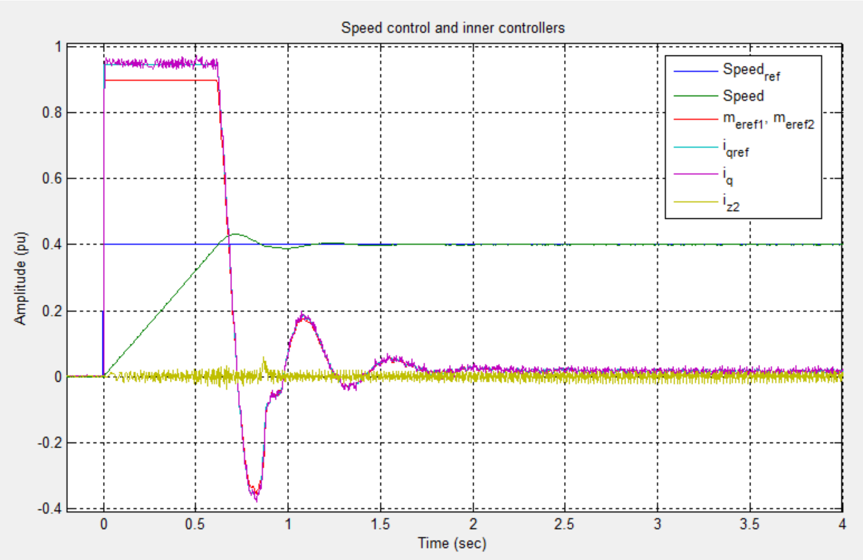

Figure 6.10: Inner controllers during speed control

6.2.2 Operation with Current asymmetries

In this operating condition, the two 3-phase groups of the machine have different currents. Thus, they do not share the power equally. This operation case can occur only in torque control mode.

To investigate the control response and operation of the drive during current asymmetries, different torque references are given to the two 3-phase groups. The torque reference $m_{e,ref1}$ is reduced from 0.8 pu to 0.4 pu, whereas $m_{e,ref2}$ is kept at a value of 0.8 pu. The DC link voltages are kept at a value of 500 V. The q-axis current controller response shows that i_q is controlled at a value determined by average of the two references. It is noted that the current i_{z2} increases from almost zero to 0.2 pu due to the imbalance in torque (q-axis currents) of the two phase groups. Since both phase groups share the magnetization equally (have the same d-axis currents), i_{z1} is very small. The ideal value would be zero.

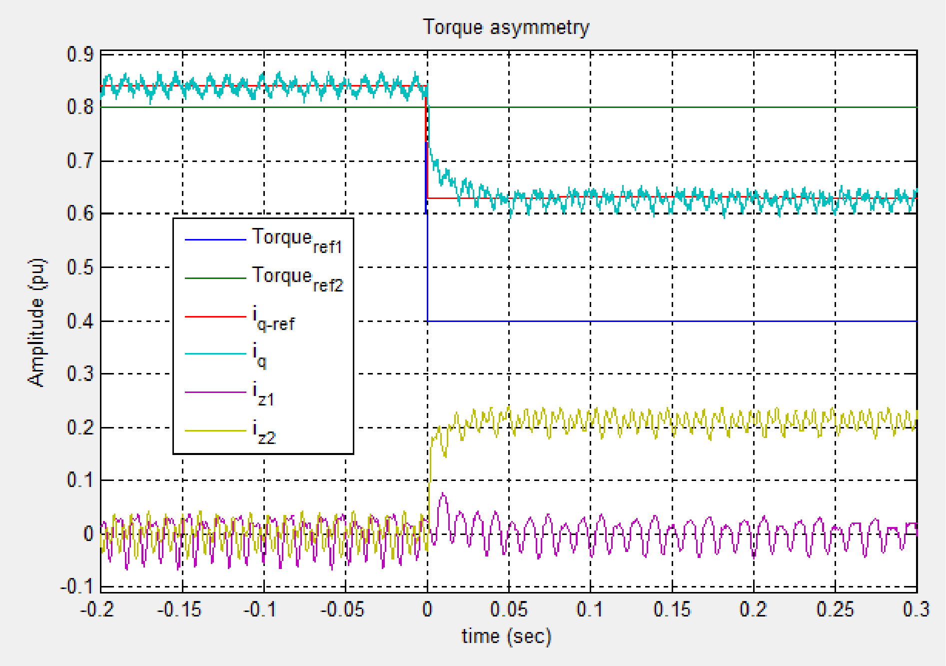

Figure 6.11: Response of controllers during torque asymmetry

The machine phase currents during asymmetrical operation are shown in Figure 6.12. The current magnitudes in phase group 1 are reduced, while current magnitudes in phase group 2 are unaffected.

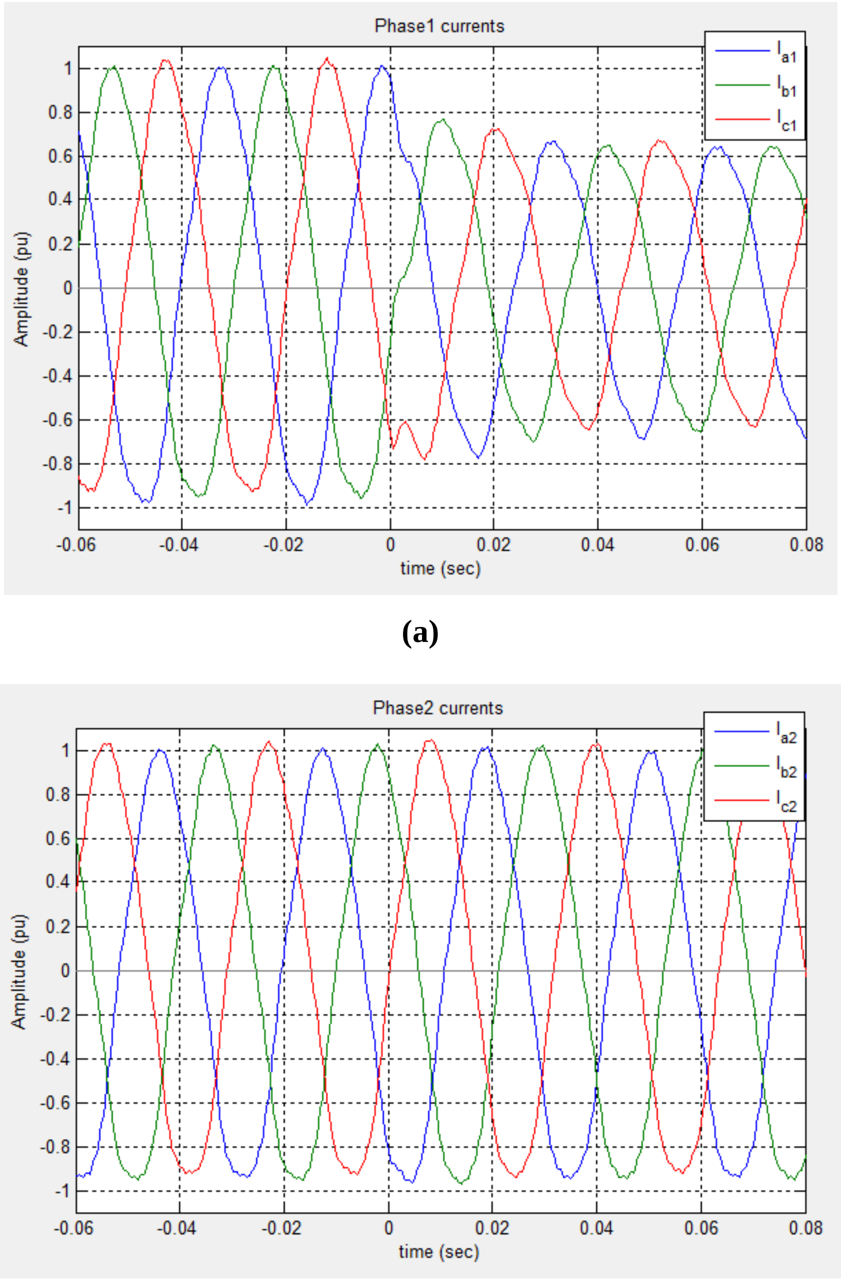

(a)

(b)

Figure 6.12: Currents during asymmetrical operation (a) phase group 1, (b) phase group 2

The oscillograms in Figure 6.13 show that amplitude of phase 1 currents is reduced from 18.0 A to 11.2 A. Phase 2 current amplitude remains constant at 18.0 A. The frequency of all stator currents is also reduced from 31.75 Hz to 22.94 Hz. This agrees with the reduction in rotor speed shown in Figure 6.14.

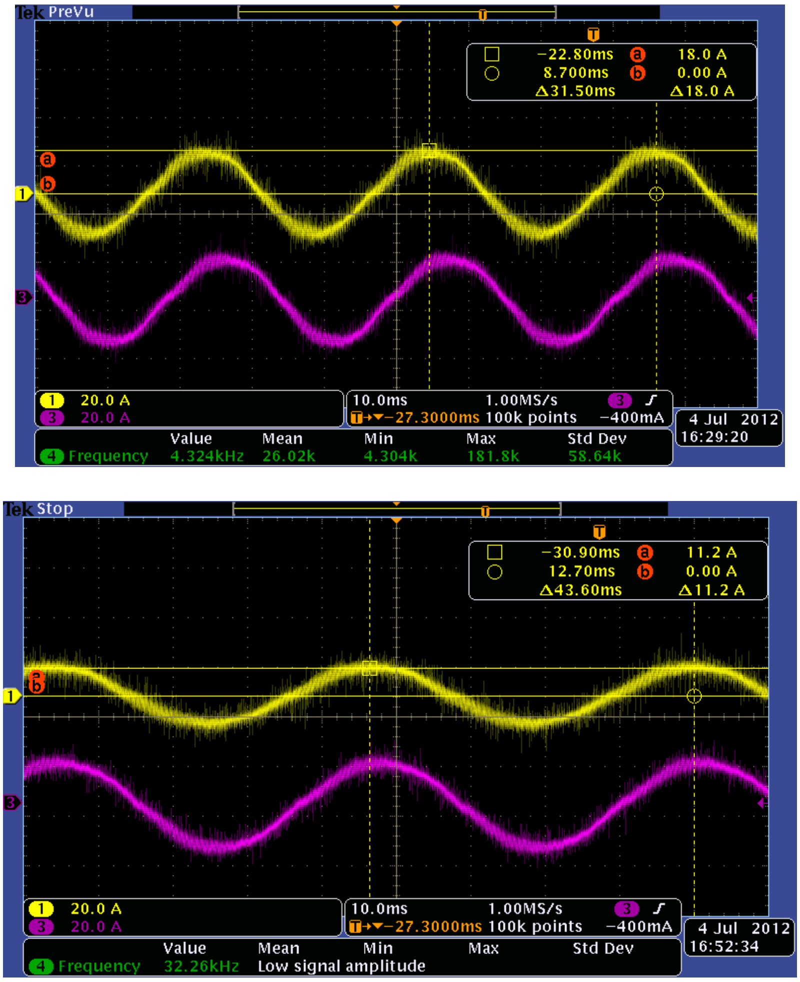

Figure 6.13: Currents isa1 and isa2 (a) before asymmetry, (b) after asymmetry

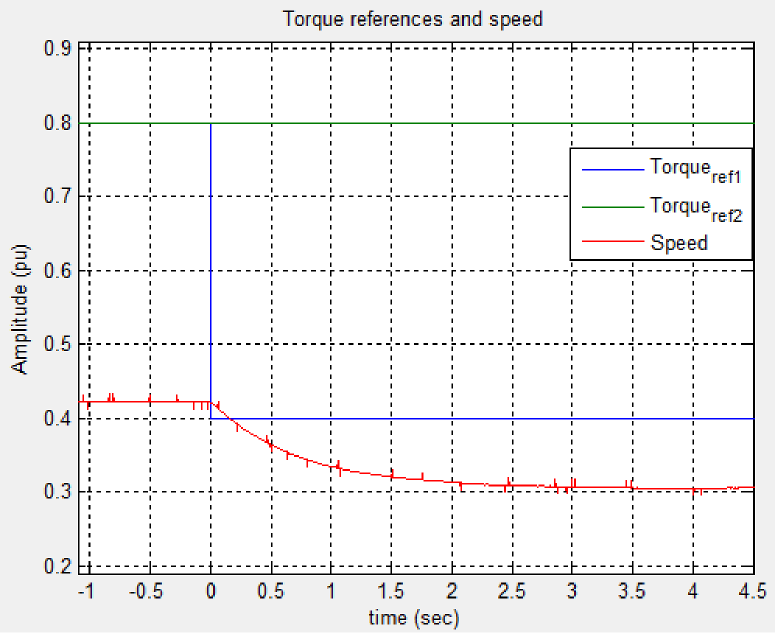

Figure 6.14: Rotor speed during asymmetrical torque operation

6.2.3 Operation during Supply Faults

The six-phase induction machine is normally supplied from two inverters with equal DC link voltage. However, variations and faults might occur, and it is important to ensure the system is robust to such faults. The cases studied in this work are differences in the DC link voltages, DC link under-voltage, trip of an inverter and turn off of a rectifier. These are taken into account in the system implementation and testing.

Figure 6.15 shows the experimental result for DC link under-voltage and variations. In the test case, the drive operates in torque control with a reference of 0.6 pu. Rectifier 1 is supplied from the variable three-phase transformer, whereas rectifier 2 gets direct line supply. DC link 2 is thus kept constant at 560 V. Initially DC link 1 is 450 V. Using the variable transformer, the supply for rectifier 1 is manually reduced to zero. This corresponds to approximately 0 – 5 seconds in the time axis of the figure. The minimum acceptable DC link voltage was set to 250 V. As soon as DC link 1 falls below this value, the torque limiter acts by reducing the torque reference me_{ref2} which reduces the power delivered to phase group 2 to almost zero. If the DC link continues falling, me_{ref1} takes on a negative value between (-0.1 pu and 0 based on the setting used here). This causes negative q-axis current (i_{sq1}) in phase group 1, and charging the DC link. Thus the DC link is kept charged. This avoids trip of inverter 1, which can continue supplying power to the machine after DC link 1 is restored. The references and currents of phase group1 (5 – 12 seconds) return to the pre-fault values when the supply of rectifier 1 increased back to normal.

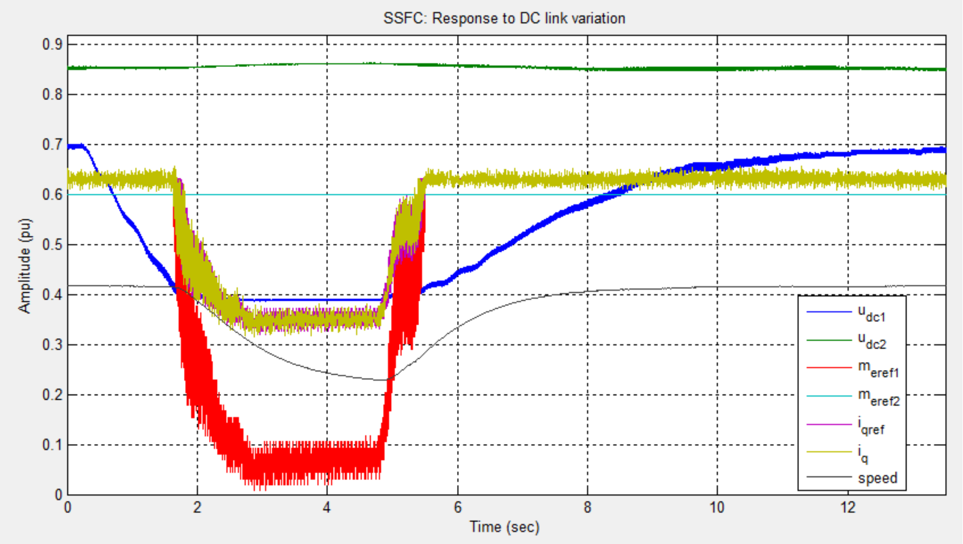

Figure 6.15: SSFC response to DC link variation and under-voltage

In another test case, the trip of one inverter during operation of the machine was investigated. Before the trip event, the machine is operated in torque control mode with a torque reference of 0.6 pu. Both DC link voltages have a value of 500 V. Inverter 2 is turned off, while inverter 1 is kept operational. The results obtained are shown in Figure 6.16 to Figure 6.20.

When inverter 2 is tripped, the current references and actual currents of phase group 2 go to zero. The machine continues to run, but with a reduced torque. The speed is also reduced given that the load stays the same before and after trip. The torque of the machine can be increased to a desired value as long as the current rating of phase group 1 is not exceeded. However, the torque capability is reduced by half since one of the phase groups is open. Current i_{z2} is induced because there is current asymmetry as a result of the trip.

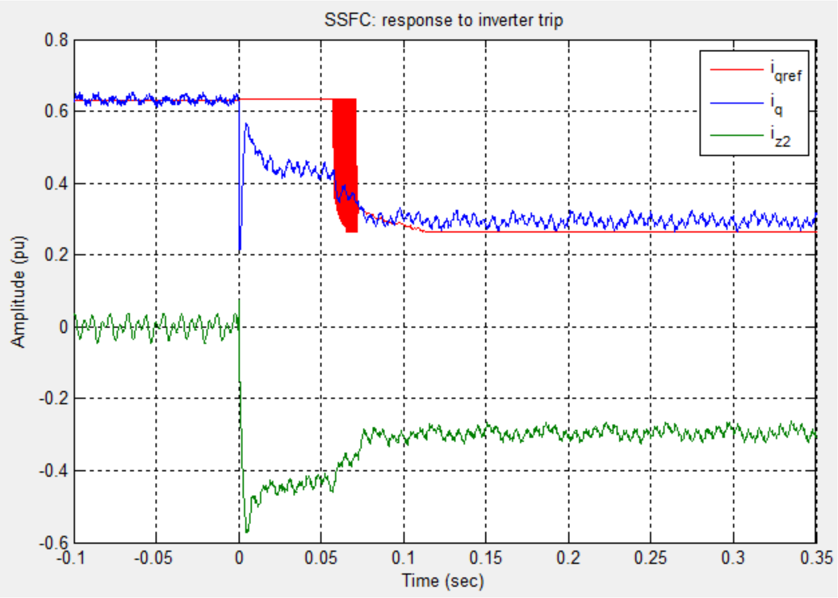

Figure 6.16: SSFC response during inverter trip, i_q and i_{z2}

The air gap flux in the machine should be kept at the rated value even after inverter trip. This is done by increasing the d-axis current in the operating phase group (i_{d1} in this case). Thus the total d-axis current i_d does not change due to the trip event. The i_{z1} is now induced because the d-axis currents of phase groups1 and 2 are different.

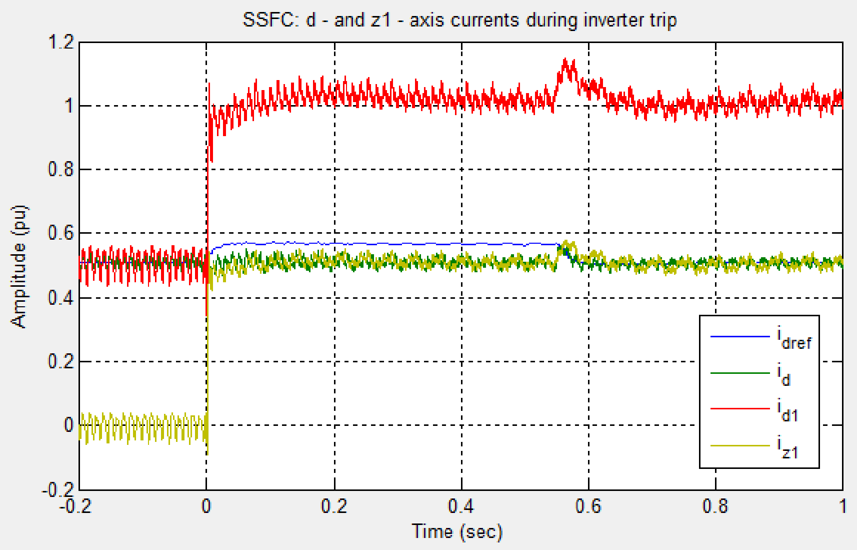

Figure 6.17: SSFC response during inverter trip: i_d and i_{z1}

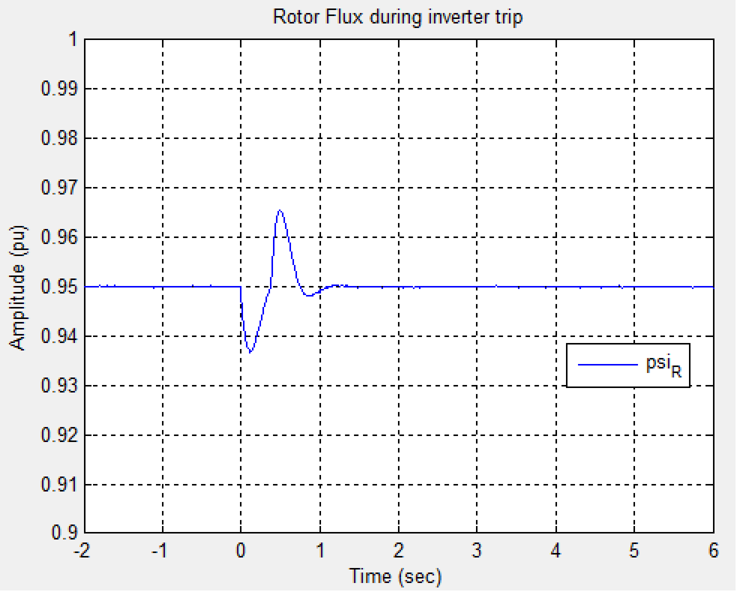

Figure 6.18: SSFC response to inverter trip, Rotor flux

Oscillograms of the i_{sa1} and i_{sa2} currents before and after the fault are given in Figure 6.19 and Figure 6.20 respectively. Currents in phase group 2 go to zero after trip, whereas phase group 1 currents increase in amplitude and decrease in frequency. The amplitude change is due to increase in i_{d1} to keep the rated flux. In this test case, i_{d1} increases from 0.508 pu to 1.016 pu while i_{q1} is constant at 0.6 pu. This causes the peak value of the stator current to increase from 0.786 pu to1.18 pu. The stator frequency reduction from 30.67 Hz to 11.0 Hz is in agreement with the decrease in torque and speed of the machine.

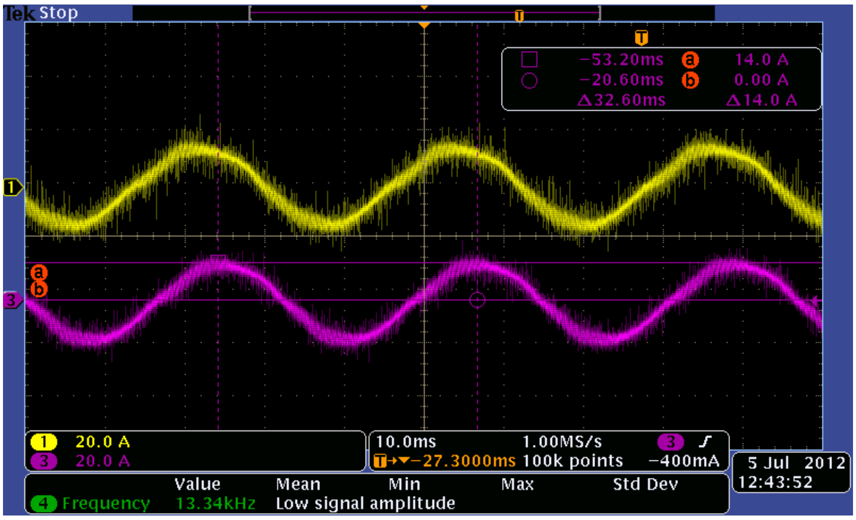

Figure 6.19: Stator currents before inverter trip

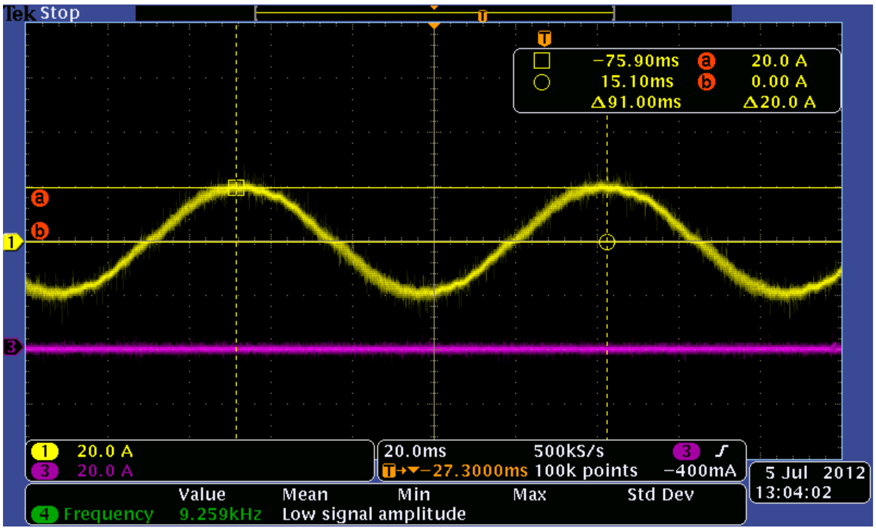

Figure 6.20: Stator currents after inverter trip

6.3 DSFC Results

In this section the results obtained using DSFC control are presented. The operating conditions and the test cases are the same as in the corresponding SSFC tests presented in the previous section. This is done in order to compare the two control methods.

6.3.1 Normal Operation

The simulation results of inner controllers are shown in figure 6.21. The initial magnetization of the machine is simulated. Then, a torque reference of 0.8 pu is applied at 0.5 sec.

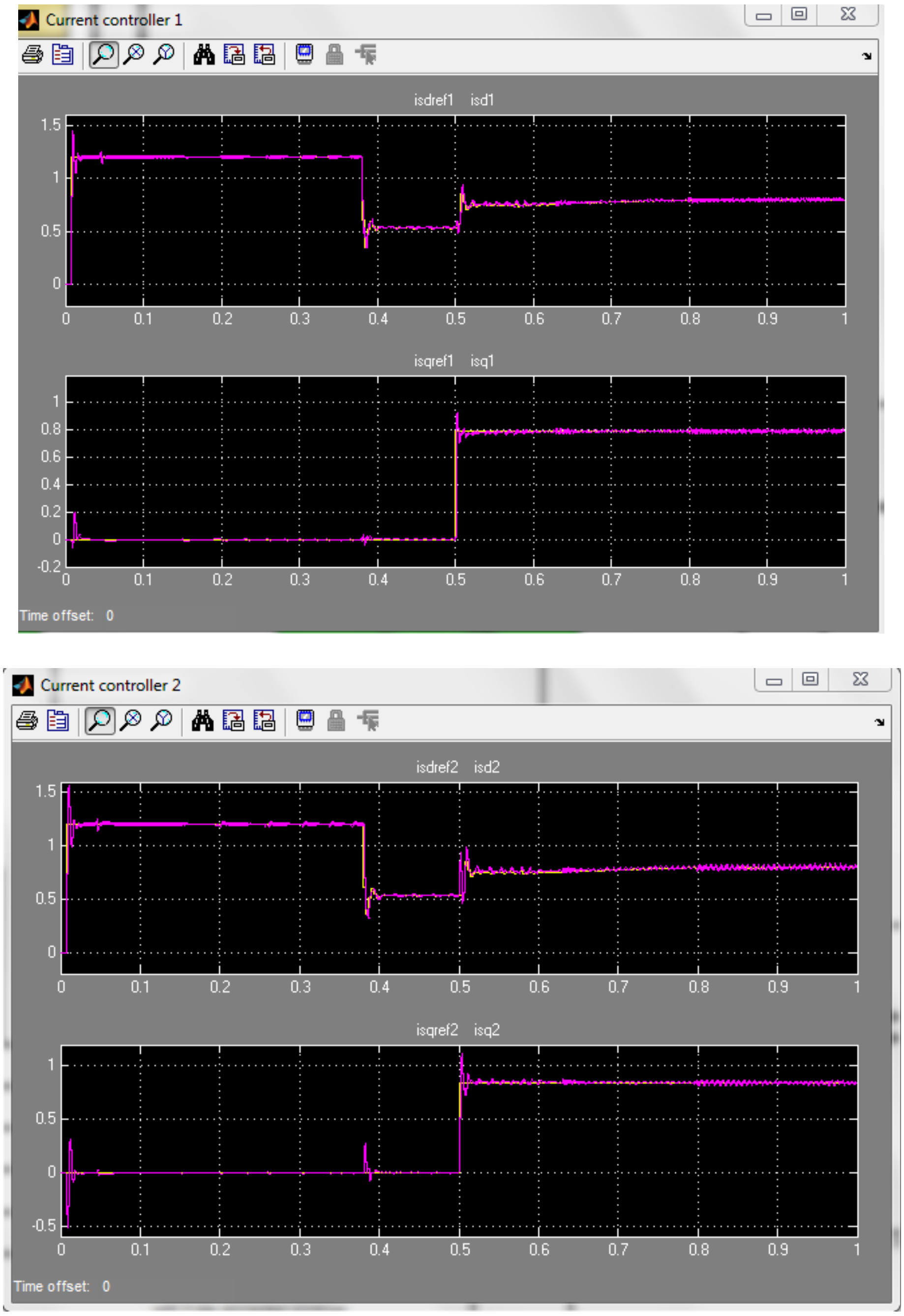

Figure 6.21: Simulation result: start-up and torque control in DSFCC

In the experiment, the machine is magnetized to rated flux before start-up. The response of the flux controller is the same as in SSFC. This agrees with the fact that the outer flux controller is the same in both methods as described in chapter 4.3.3. However, the inner controllers used here are i_{d1} and i_{d2}, instead of i_d.

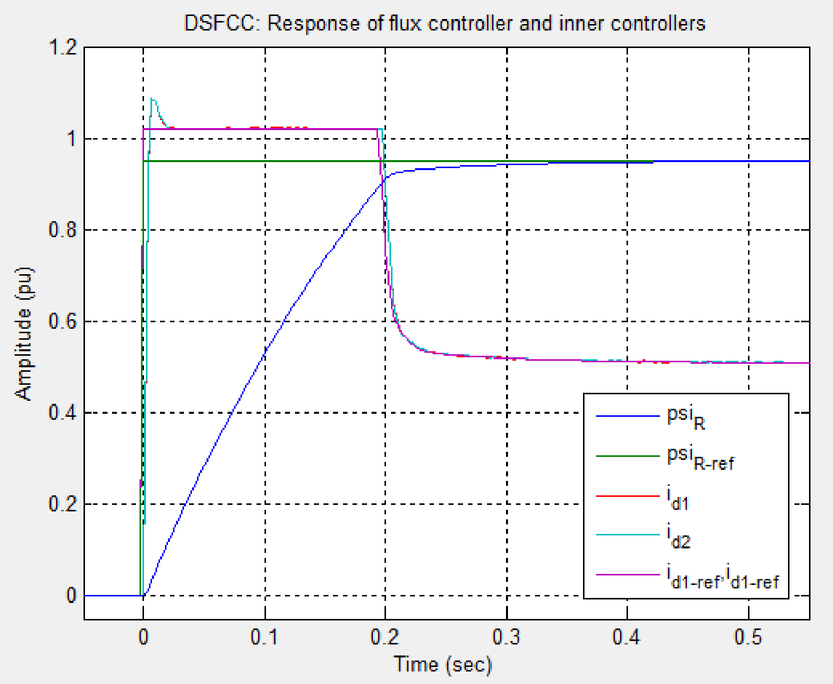

Figure 6.22: Flux and d-axis current control in DSFC

After magnetization, the drive was started in torque control mode. Applying a step torque reference of 0.8 pu gave the result shown in figure 6.23. The d-axis currents are also shown to indicate the effect on them by the torque control loop.

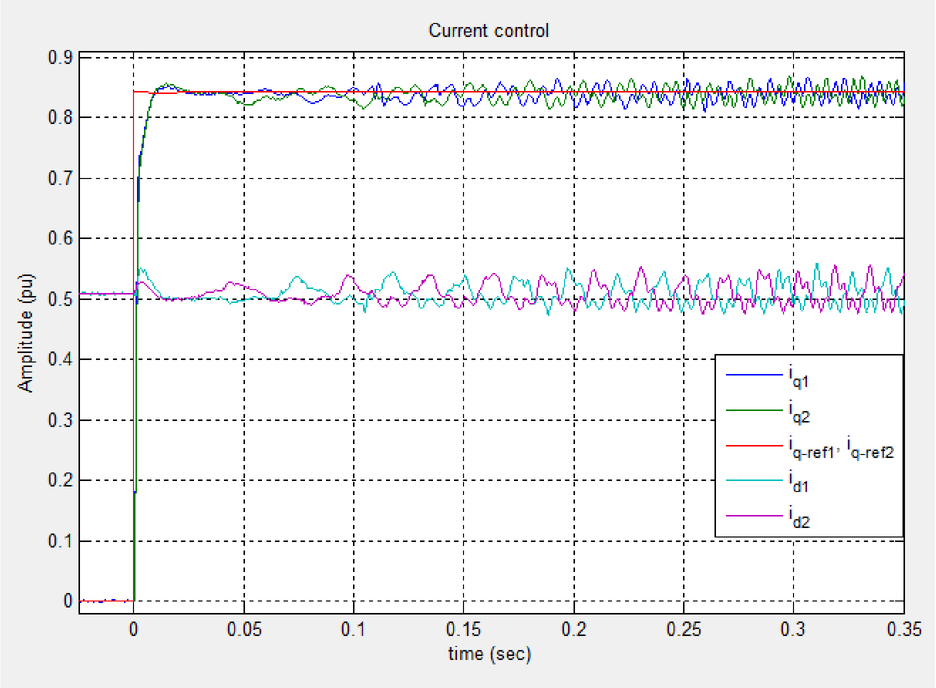

Figure 6.23: Startup and q-axis current control in DSFC

Operation of the drive in speed control mode was also tested. The speed controller response was found to be the same as in the SSFC result. This verifies that the speed control is the same in both control methods. The difference is that the DSFC uses the inner i_{q1} and i_{q2} controllers, whereas SSFC uses i_q controller.

6.3.2 Operation with Current Asymmetries

The case of current/torque asymmetry was tested in DSFC method. The drive is in torque control mode. Torque reference 1 is reduced from 0.8 pu to 0.4 pu while torque reference 2 remains constant at 0.8 pu. The responses of i_{sq1} and i_{sq2} controllers are shown in figure 6.24.

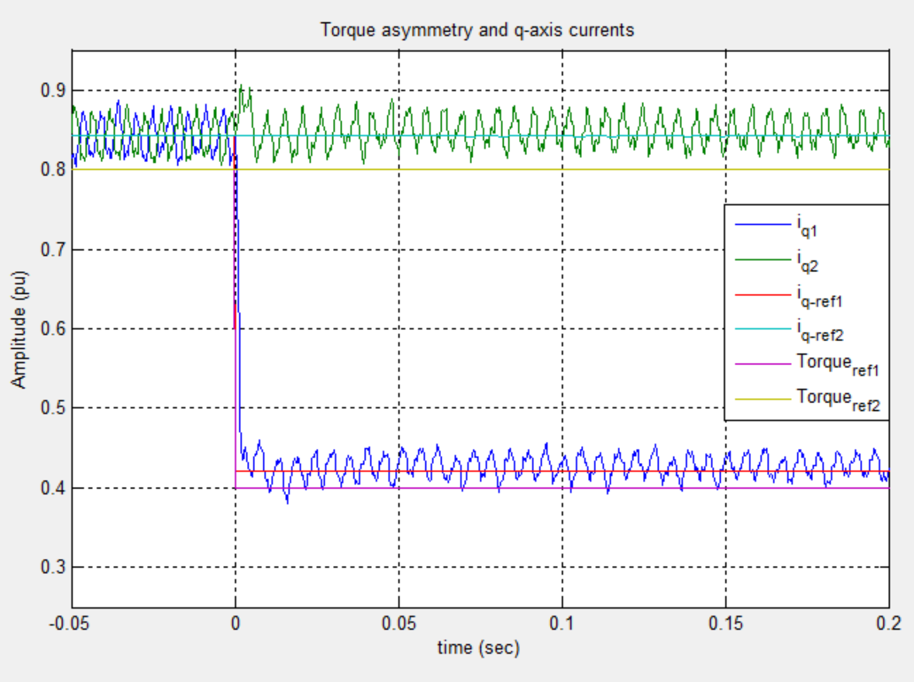

Figure 6.24: Torque and current asymmetry

Figure 6.25 shows the effect of the torque asymmetry on the i_{sd1}, i_{sd2}, i_{sz1} and i_{sz2} controllers. It can be seen that i_{sz2} is induced due to the asymmetry.

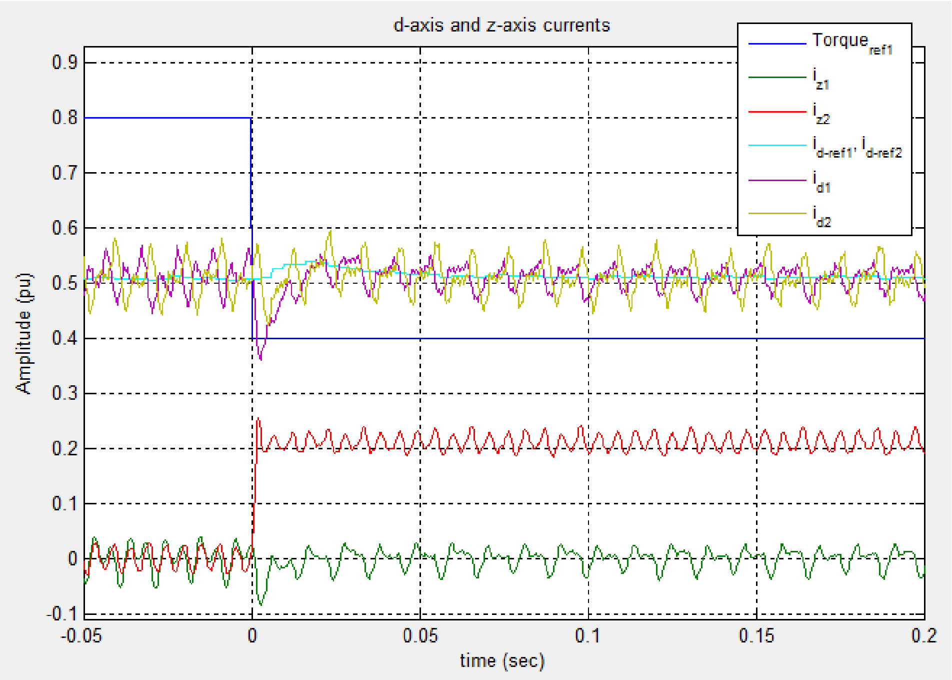

Figure 6.25: d-axis and z-axis currents during torque asymmetry

The rotor speed in the drive during torque asymmetry is shown in figure 6.26. The speed decreases as the total torque is reduced due to decrease in torque developed by phase group 1.

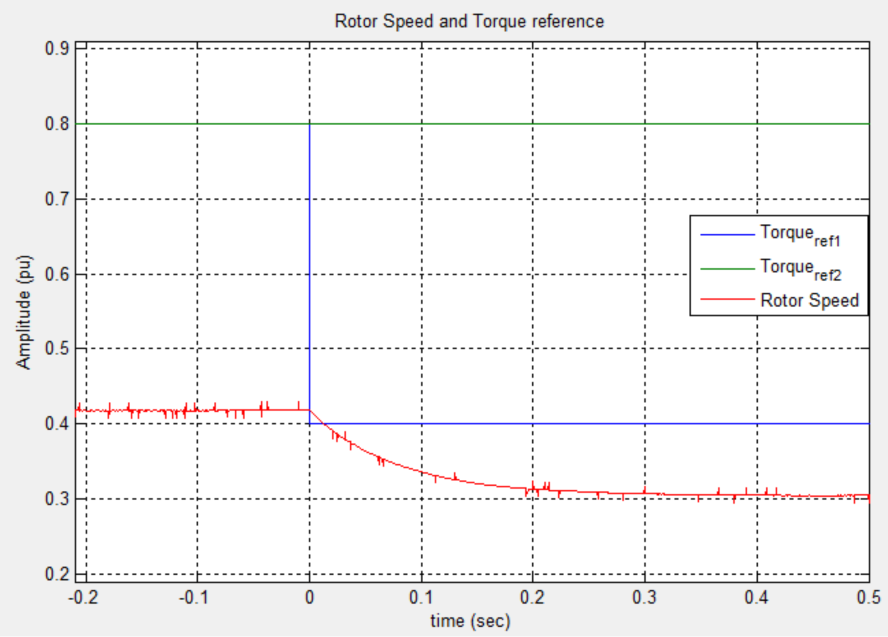

Figure 6.26: Rotor speed during torque asymmetry

6.3.3 Operation during Supply Faults

The effect of DC link voltage variations, rectifier turn off and inverter trip was investigated using similar test cases as in the SSFC tests of section 6.2.3.

The test case for DC link voltage variations gave the results in figures 6.27and 6.28. Rectifier 2 was supplied from ac line directly, keeping DC link voltage 2 constant at 560 V. Supply of rectifier 1 was reduced to zero and restored to normal after few seconds. Due to this DC link voltage 1 gets reduced from the pre-fault value (450 V). It does not go to zero because it is kept charged due to the control system. All quantities return to pre-fault values when the supply for rectifier 1 is increased back to normal.

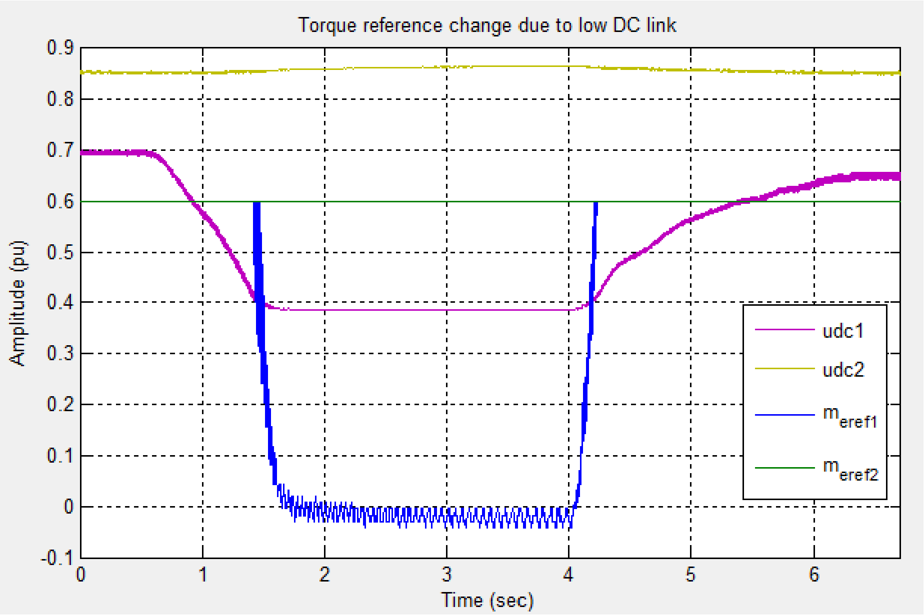

Figure 6.27: DC link under-voltage and change in torque references

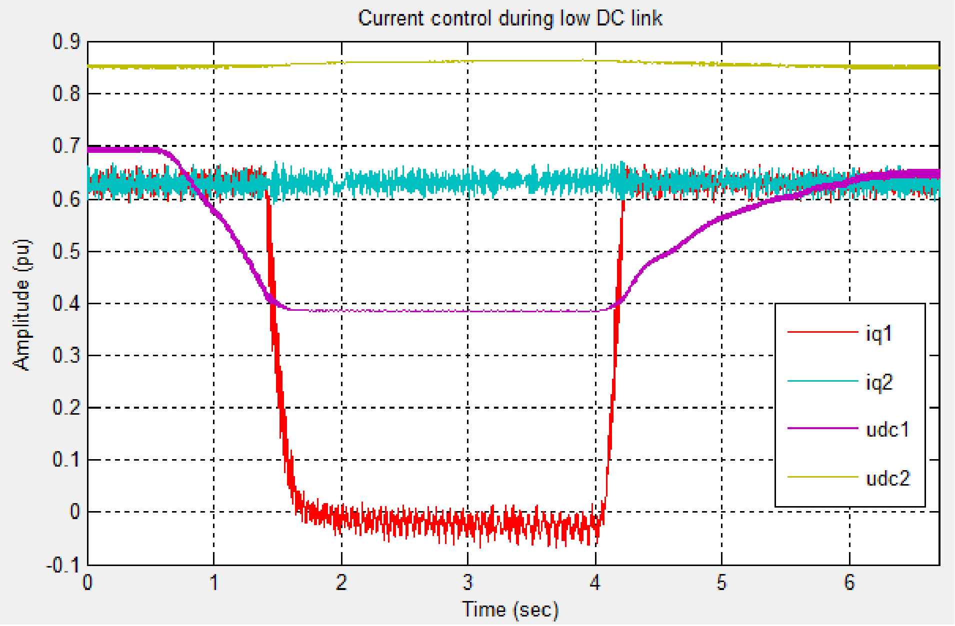

Figure 6.28: DC link under-voltage and q-axis currents

To test the effect of inverter failure on the system, inverter 2 was tripped while inverter 1was kept operational. The main results are shown in figures 6.29 and 6.30. The controller and phase currents in phase group 2 go to zero. The increase in the amplitude of phase group 1 currents is because the remaining phase has to keep the rotor flux linkage at rated value.

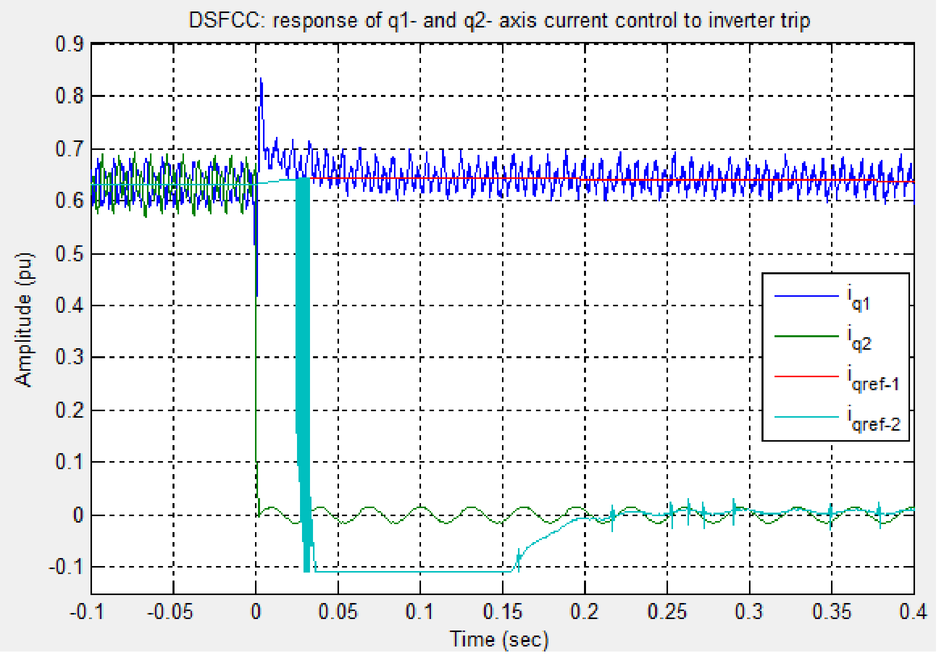

Figure 6.29: Response of current controllers to inverter trip

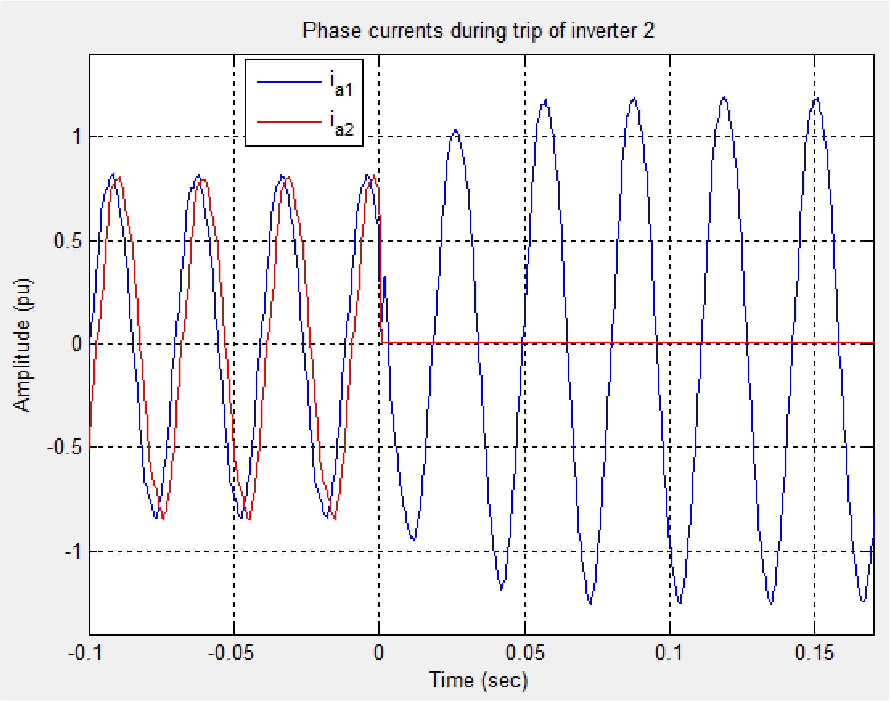

Figure 6.30: Phase currents (i_{sa1} and i_{sa2}) during inverter trip

7 Discussion of Results

7.1 Normal Drive Operation

In normal operating conditions of the drive, both SSFC and DSFC methods gave comparable results. The theoretically calculated control parameters were tuned to improve the transient response. The performance parameters used are rise time, percent overshoot, settling time and steady state error. The rise time is taken as the time taken by the response to increase to 90% of the reference step input. The settling time the time the response takes to remain within 2% error of the step input. Using the designed control system and tuned parameters, the inner current controllers gave fast response with small overshoot. The responses were found to be stable. The response of outer controllers was found to be the same in both control methods.

The response of the d-axis controllers in both control methods can be compared from figures figure 7.1 and 7.2. In both cases, the reference is increased as a step from 0.0 to 0.5 pu. Responses of the other controllers were compared in a similar way and found to be comparably good in both methods.

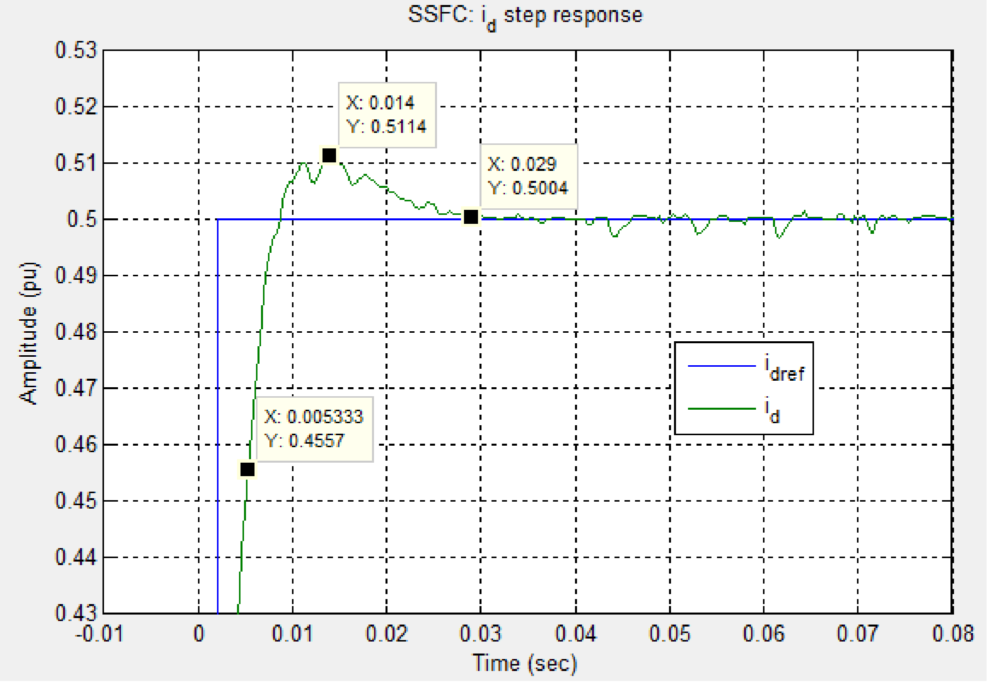

Figure 7.1: SSFC - Performance of i_{sd} controller

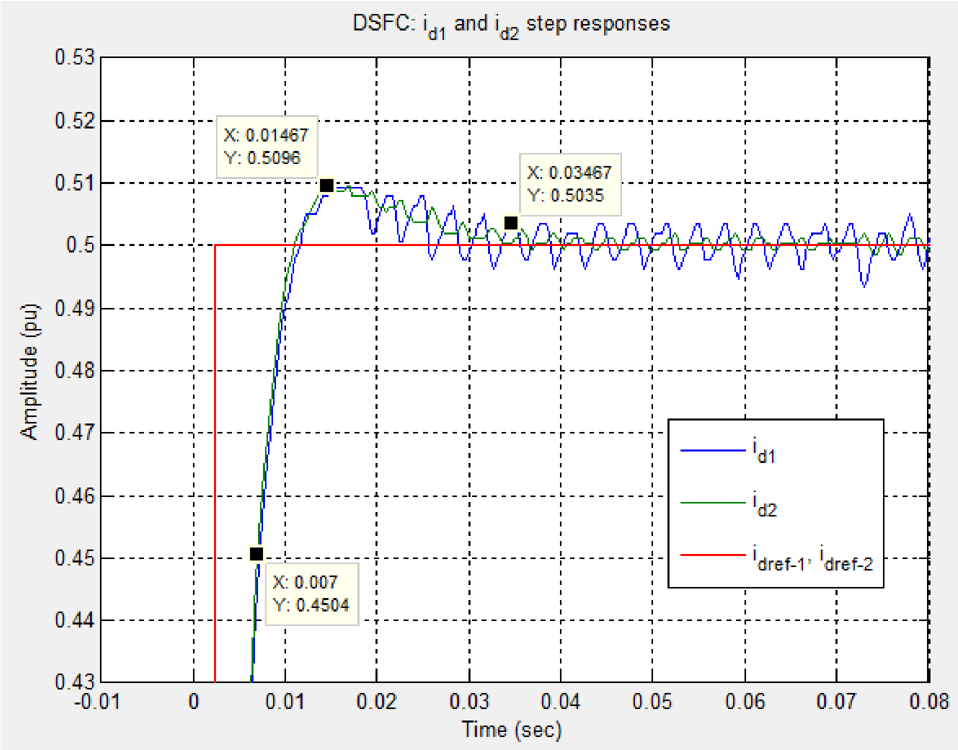

Figure 7.2: DSFC - Performance of i_{sd1} and i_{sd2} controllers

To compare the stator losses due to asymmetry between the two 3-phase groups, the currents in the (z_1, z_2) system were investigated. These currents are directly controlled in the SSFC method, whereas they can be obtained using transformations in DSFC. Ideally, these currents are zero in steady state during normal operation of the drive. These currents are, in reality, small but not zero since small imbalances between the phase groups can be expected. A comparison of the (z_1, z_2) system currents in the two control methods can be made from figures 7.3 and 7.4. The values in –ve time axis are for normal drive operation, whereas the +ve axis values are for asymmetrical torque operation. It is evident that the currents are similar in both control meth.ods

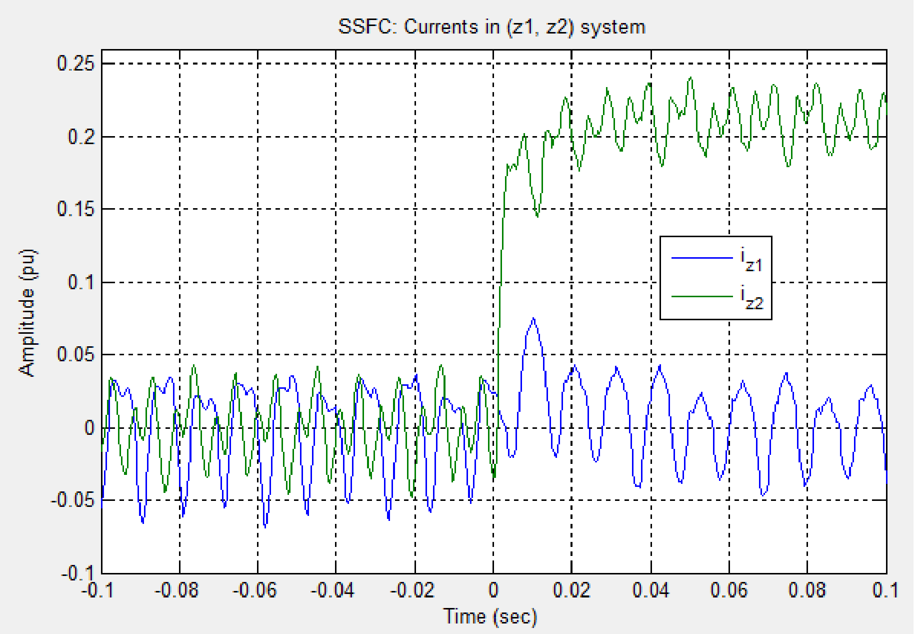

Figure 7.3: SSFC - (z_1, z_2) system currents

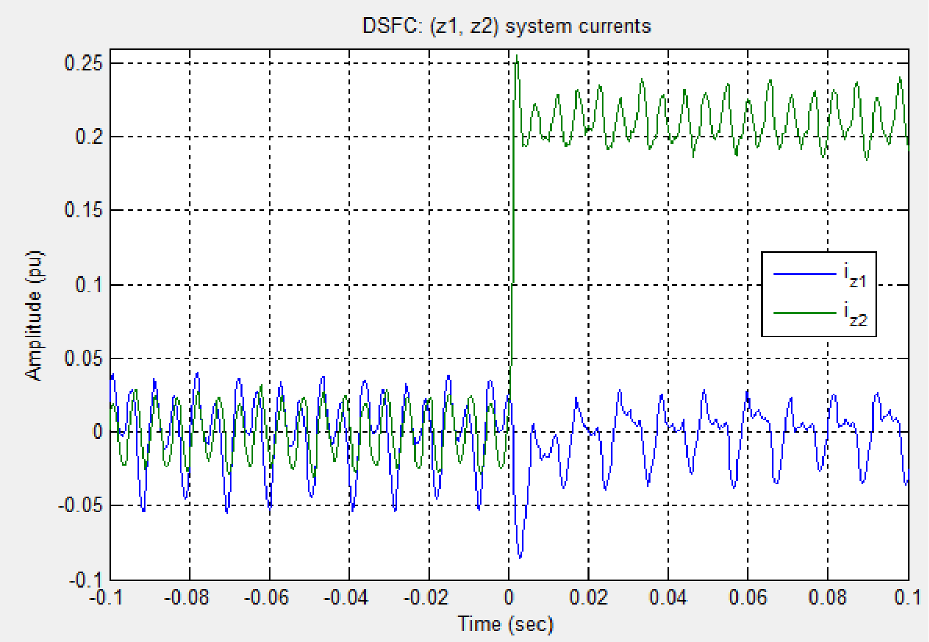

Figure 7.4: DSFC - (z_1, z_2) system currents

One main difference in the implementation of the two methods is the decoupling network. In SSFC, the full decoupling network based on the design equations is used. In DSFC, some of the decoupling terms are removed to minimize overshoot of the responses and improve control performance. However, the full decoupling in DSFC also gives stable response.

7.2 Operation during Asymmetries and Faults

A comparison can be made between the responses of SSFC and DSFC to various asymmetries and fault cases. Current asymmetries, DC link under-voltage and variations, and inverter trip have been investigated.

Both control methods work well and give comparable response during current asymmetries. The responses to DC link under-voltage and variations are also similar in both methods. This is the case both during speed and torque control modes.

When one inverter is tripped during torque control mode, both SSFC and DSFC respond in similar way. However, the response in DSFC was found to be faster as it can be seen from figures 7.5 and 7.6. In both cases, the drive is operated with a torque reference of 0.6 pu before the fault.

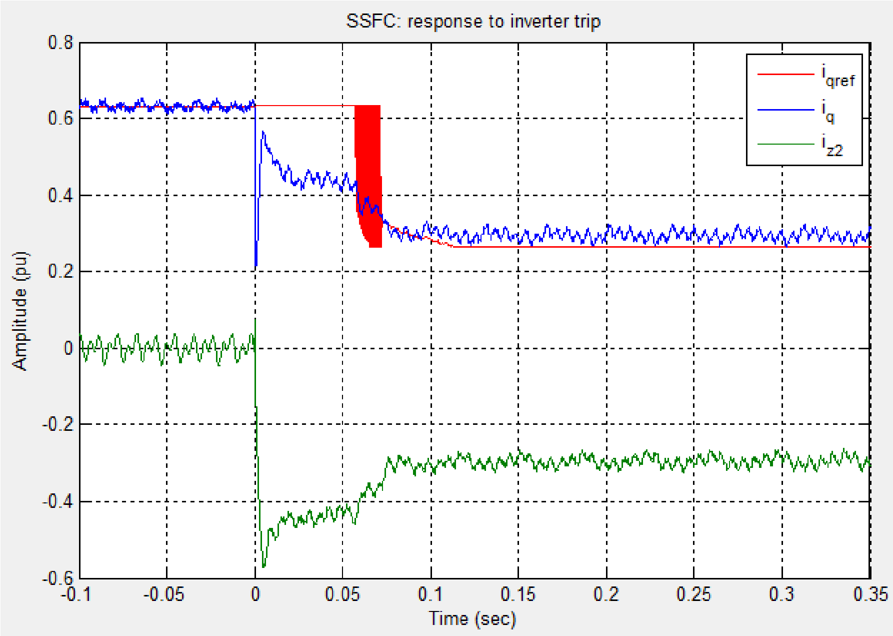

Figure 7.5: SSFC - Response to trip of inverter 2 in torque control mode

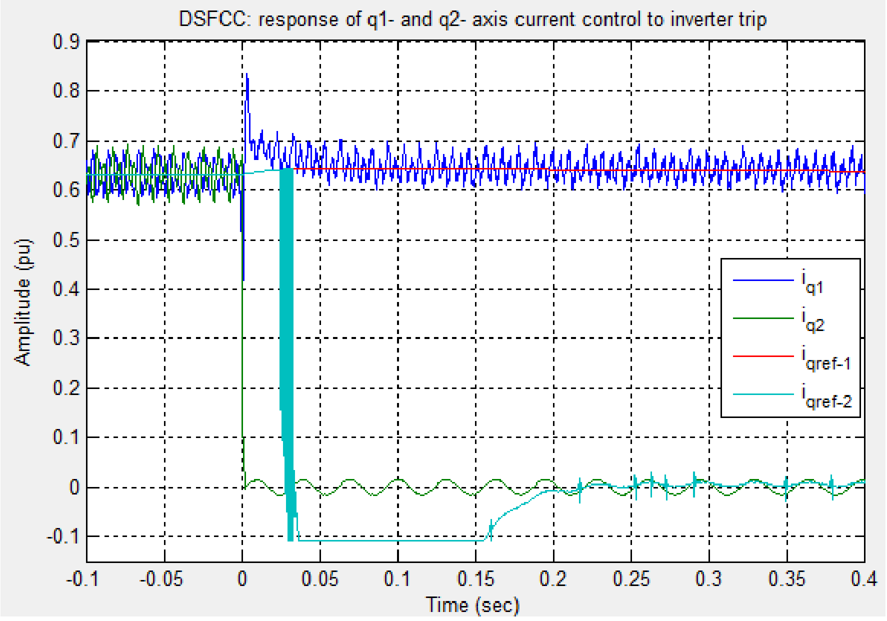

Figure 7.6: DSFC - Response to trip of inverter 2 in torque control mode

When the drive is operated in speed control mode and an inverter trips, the DSFC method was found to respond well and the drive can continue operation using the remaining inverter supply. However, the SSFC method did not work as expected and resulted in trip of the non-affected inverter.

In general, the SSFC method was found to be more difficult to implement especially during asymmetries and faults. The actual system references and asymmetries come in the form of (d_1, d_2) and (q_1, q_2) quantities, but control is done in (d, q) and (z_1, z_2) system. This causes difficulty when the asymmetries in outer control variables need to be reflected in the inner controllers. SSFC method is also more computationally demanding due to the transformations needed between (d_1, q_1, d_2, q_2) and (d, q, z_1, z_2). These transformations are not necessary in the DSFC method. This can be seen from the structure of inner controllers in figure 4.2 and figure 4.8.

7.3 Analysis of Ripple and Harmonics

When the stator measured currents are converted to the synchronous d-q system, ripples are found to be superimposed on the DC values in steady state. These ripples were observed in both control methods in all operating cases of the drive.

The buildup of ripples when the drive is started is demonstrated in figure 7.7. Before applying a torque reference of 0.8 pu, the machine had been magnetized. The d-axis current control response is has almost zero ripple before the drive is started. When the drive is started, there are ripples in both d-axis and q-axis currents. Similar results were found in the DSFC method.

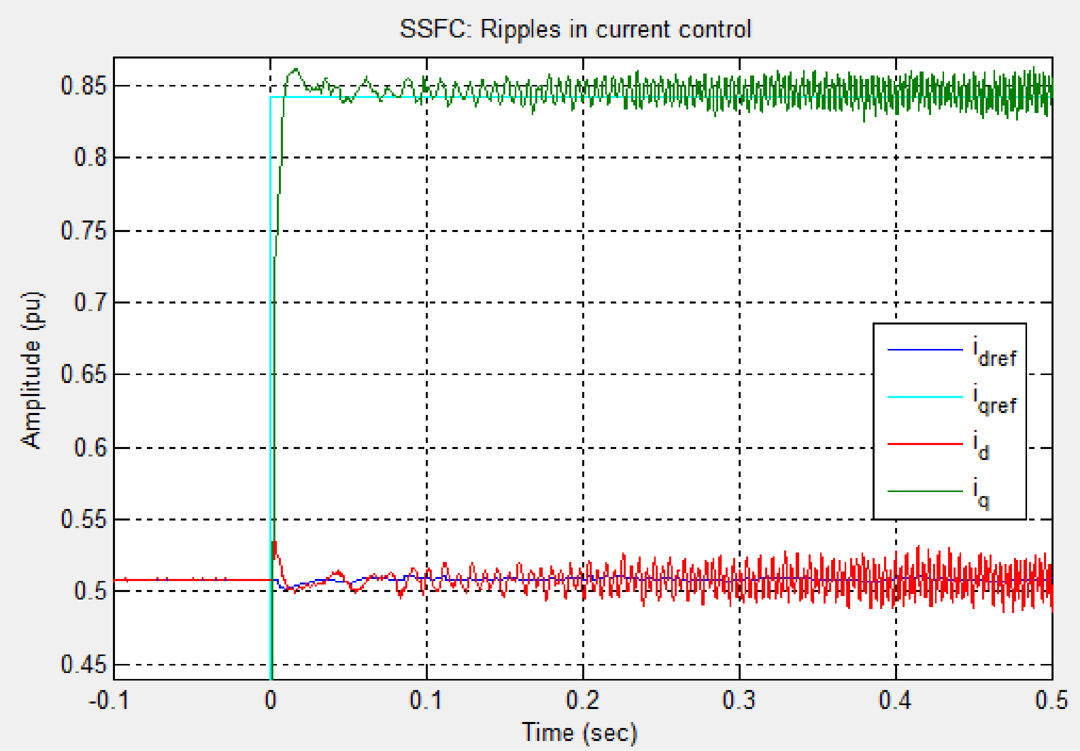

Figure 7.7: Ripple in controlled currents before and after start-up [SSFC]

The ripples were found to be strongly dependent on the rotor speed. To investigate this dependence, the ripple amplitude and frequency were measured at different speeds. The machine was run in torque control mode with a torque reference of 0.18 pu in all the cases. The load resistance connected to the DC machine was varied in order to vary the speed. The results found using DSFC method are given in table 7.1.

Speed [pu]	**Fundamental stator frequency [Hz]**	**Frequency of the main ripple components i_{d1}, i_{d2}, i_{q1} and i_{q2} [Hz]**	**Peak-peak ripple in i_{q1} & i_{q2} [pu]**	**Peak-peak ripple in i_{d1} & i_{d2} [pu]**
0.075	5.63	53.73, 134.9	0.0303	0.0143
0.13	9.75	58.65, 234.6	0.0425	0.028
0.242	18.2	110.0, 437.0	0.0453	0.0355
0.44	33.0	99.71, 199.4	0.0916	0.0581
0.56	42.0	126.1, 252.2	0.1356	0.0808
0.6	45.0	136.4, 227.3	0.21	0.1807

Table 7.1: Current ripple frequency and harmonics as function of rotor speed

From analysis of the results presented in table 7.1, it was found that:

- The ripples in both d- and q-axis currents increase with speed,
- At low speed, the largest ripple component is 6th harmonic of the fundamental stator frequency, followed by the 24th harmonic,
- At higher speeds (0.44, 0.56 and 0.6 pu in the table), the 3rd harmonic is the major component. A 6th harmonic is also observed (but 5th harmonic at 0.6 pu speed),

For the test case described above, the ripples at speeds of 0.075 pu and 0.44pu are shown in figure 7.8 and figure 7.9, respectively. During the experiment, considerable vibration was observed in the drive when the machine is operated at higher speeds (greater than 0.4 pu) and light load.

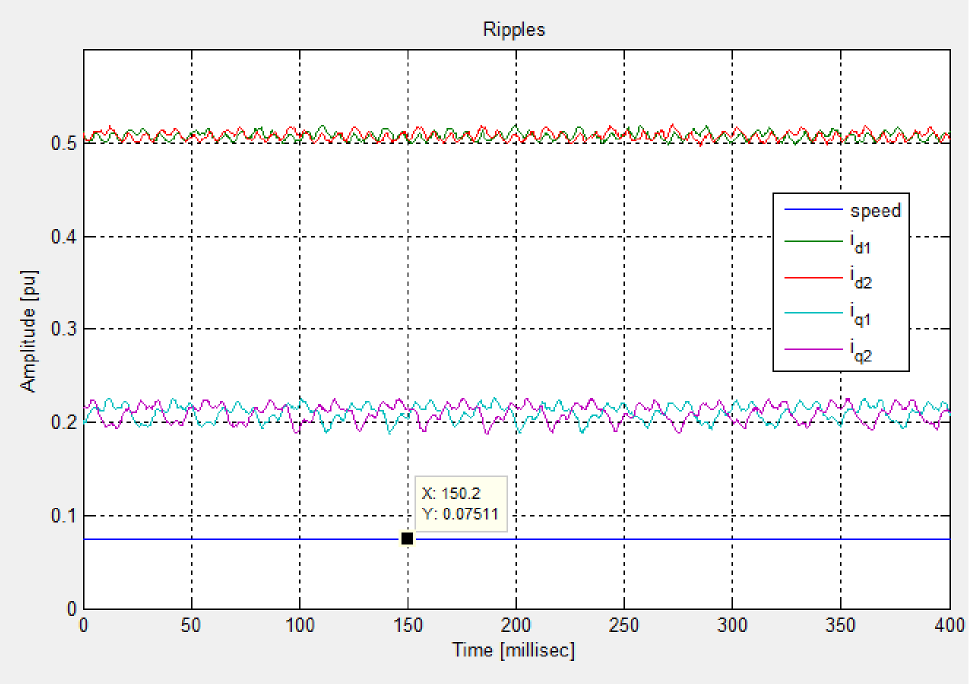

Figure 7.8: Current ripples at 0.075 pu speed [DSFC, 0.2 pu torque]

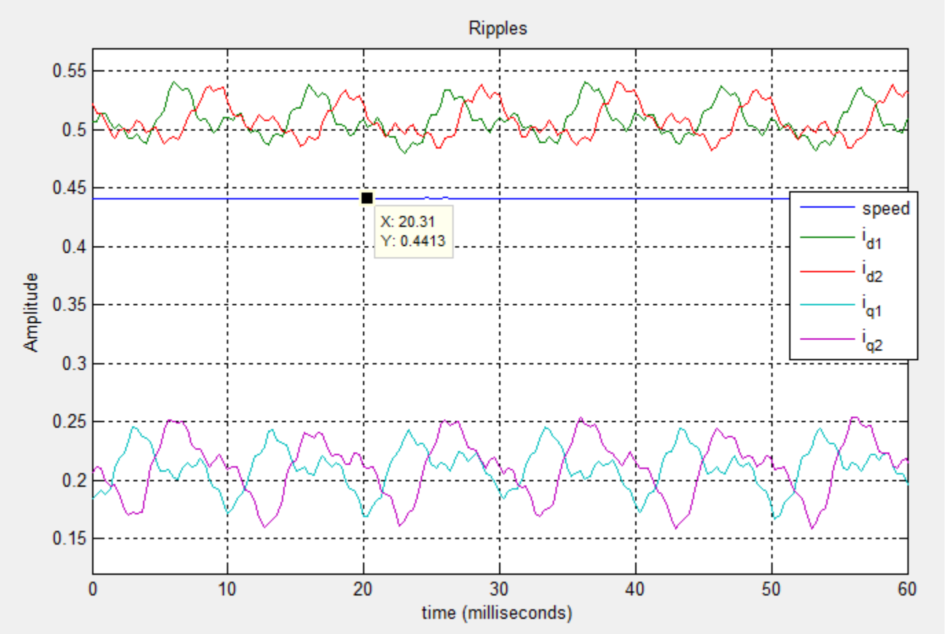

Figure 7.9: Current ripples at 0.44 pu speed [DSFC, 0.2 pu torque]

In the simulation results, the ripple in the current controllers was not found to be dependent on speed of the machine. The magnitude is also very small. A sample of the control response is shown in figure 7.10. The result is from SSFC control at a torque of 0.8 pu. The steady state speed is 0.71 pu. The magnitude of the peak-to-peak ripple is approximately 0.012 pu in both i_d and i_q. The frequency of the ripple in i_d is about 3 times the fundamental frequency

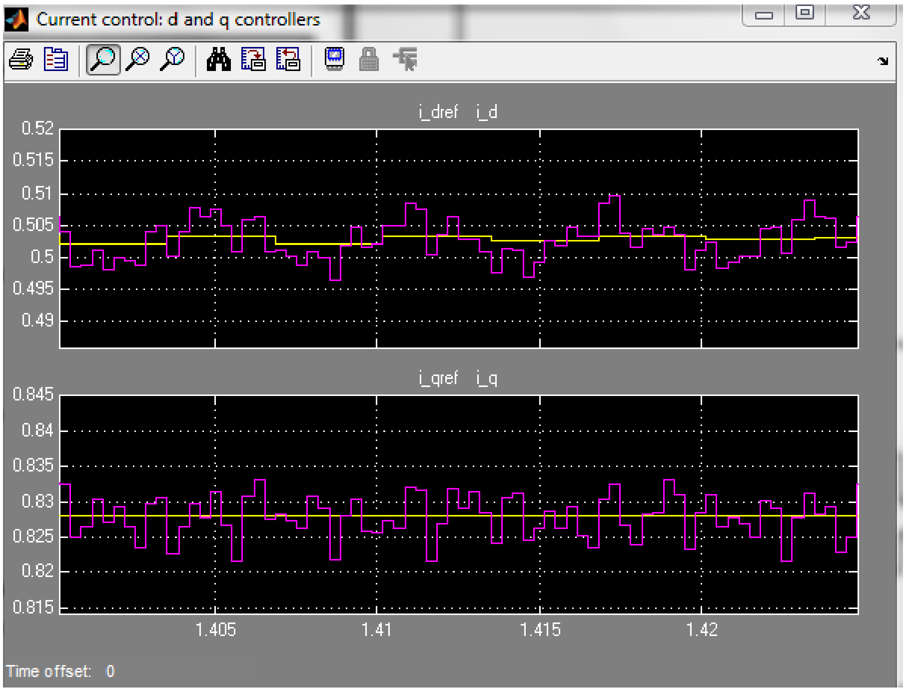

Figure 7.10: Simulation result: Ripple in current control [SSFC, torque control at 0.8 pu, speed 0.7 pu]

8 Conclusion and Further Work

8.1 Conclusion

Electric ship propulsion has recently gained considerable attention. Variable speed electrical drives, including multiphase drives, are of interest in this area of application. In this thesis, the modelling and control of a six-phase induction motor drive has been investigated. The modelling of six-phase induction machine using two different approaches was presented. Vector control techniques based on these two approaches were studied. The work included theoretical study, simulations and experimental implementation of the drive control system.

The normal operation of the drive was investigated initially. The results showed that both SSFC and DSFC control methods give desired transient and steady state performance. Control of speed and torque of the machine has been achieved for different loading conditions, from no-load up to full-load. It was also found that the outer (flux and speed) controllers are the same in both control methods. The difference between the implementation of the two methods is in the inner (current) controllers. The simulation and experimental results are similar in this operating condition.

Operation of the drive during current asymmetries and supply faults was also considered in the control design and testing. When there is current asymmetry in the two 3-phase groups of the induction machine, both SSFC and DSFC can control the drive as desired. This was the case for both simulations and experimental results.

During DC link under-voltage and variations, the two methods give acceptable response. However, the response in DSFC was found to be faster than in SSFC method. In both methods, the affected DC link is kept charged at a desired level. This is needed so that the affected inverter does not trip, for example in the case of temporary failure in the supply of the DC link. When the supply is restored to normal value, the operation of the drive automatically returns to the pre-fault state.

In the event loss of one inverter, the machine can continue to operate from the remaining healthy supply. The available torque and power is, of course, reduced to half of the total six-phase machine rating. This has been achieved in both torque control and speed control modes using DSFC. The SSFC method can also handle this case in torque control mode, but this has not been achieved in speed control mode. From the results in this work, it can be concluded that better control of the drive is achieved using the DSFC method. It can handle the system asymmetries and faults in a better way than the SSFC.

8.2 Further Work

In this work, the modelling of six-phase induction motor drive has been studied. The control system has also been designed and implementation in a laboratory setup.

The following tasks could be considered for further work in the drive system:

- Experimental identification of the six-phase induction machine parameters,
- Investigation of the ripple and harmonics in the torque and currents of the drive,
- Improvement of the SSFC method so that it can give desired performance during inverter trip when the machine operates in speed control mode.
- Investigation of other modulation techniques, and the effect on current and voltages harmonics.

References

[1] A.K. Ådnanes, "Maritime Electrical Installations and Diesel Electric Propulsion," Tutorial Report, ABB Marine AS, Oslo, Norway, April 2003. Available: www.abb.com (Accessed: 18 December 2011)

[2] V.M. Moreno and A. Pigazo, "Future Trends in Electric Propulsion Systems for Commercial Vessels," *Journal of Maritime Research,* vol. IV, no. 2, pp. 81-100, Aug. 2007. Available: http://www.jmr.unican.es/pub/00402/0040206.pdf (Accessed: 10 July 2012)

[3] G.K. Singh, "Multi-phase induction machine drive research – a survey," *Electric Power Systems Research*, vol. 61, issue 2, pp. 139-147, March 2002.
doi: 10.1016/S0378-7796(02)00007-X

[4] E.A. Klingshirn, "High Phase Order Induction Motors – Part I - Description and Theoretical Considerations," *IEEE Trans. Power App. Syst.*, vol. PAS-102, pp. 47–53, Jan. 1983. doi: 10.1109/TPAS.1983.317996

[5] R. Bojoi, M. Lazzari, F. Profumo and A. Tenconi, "Digital field-oriented control for dual three-phase induction motor drives," *IEEE Trans. Ind. Appl.*, vol. 39, no. 3, pp. 752–760, May-June 2003. doi: 10.1109/TIA.2003.811790

[6] R. Bojoi, A. Tenconi, F. Profumo, G. Griva and D. Martinello, "Complete analysis and comparative study of digital modulation techniques for dual three-phase AC motor drives," *Proc. IEEE PESC'02*, vol.2, pp.851–857, 2002.
doi: 10.1109/PSEC.2002.1022560

[7] R. Nilsen, "Modelling of multi-phase synchronous machines," Wärtsilä Norway AS, Ship Power Technology R& D, Trondheim, Norway, Tech. Rep. Rev. B, Jul. 2010.

[8] R. Nilsen, "dqz1z2 and dq01-dq02 models of 6-phase PM machines," Wärtsilä Norway AS, Ship Power Technology R& D, Trondheim, Norway, Tech. Rep., Mar. 2012.

[9] R. Nilsen, "Distributed 3-phase control of 6-phase PM Motors," Wärtsilä Norway AS, Ship Power Technology R& D, Trondheim, Norway, Tech. Rep., Jul. 2009.

[10] Ø.M.M. Hoem, "Control of Six-Phase Machines," Master thesis, Dept. Elect. Power Eng., NTNU, Trondheim, June 2010.

[11] S. Thopate, “Modelling, simulation and implementation of Multi-phase Induction Motor Drives,” Master thesis, Dept. Elect. Power Eng., NTNU, Trondheim, June 2011.

[12] N.B. Araya, “Torque Limiter in Six-phase Induction Machine Control,” Wärtsilä Norway AS, Ship Power Technology R& D, Trondheim, Norway, Tech. Rep., Aug. 2011.

[13] N.B. Araya, “Control of Multiphase Machines,” Specialization Proj., Dept. Elect. Power Eng., NTNU, Trondheim, December 2011.

[14] S.P. Smith, “The theory of armature windings,” *Journal of the Institution of Electrical Engineers*, vol. 55, no. 261, pp. 18-36, Dec. 1916.

[15] Philip L. Alger, E.H. Freiburghouse and D.D. Chase, “Double windings for turbine alternators,” *AIEE Trans.*, vol. 49, no. 1, pp. 226-244, Jan. 1930.

[16] Y.H. Ku, “Extension or 2-Reaction Theory to Multiphase Synchronous Machines,” *AIEE Trans.*, vol. 56, no. 9, pp. 1197-1201, Sept. 1937.

[17] R.H. Nelson and P. C. Krause, “Induction machine analysis for arbitrary displacement between multiple winding sets,” *IEEE Trans. Power App. Syst.*, vol. PAS-93, no. 3, pp.841-848, May 1974.

[18] T.A. Lipo, “A d-q model for six phase induction machines,” in *Int. Conf. electric Machines*, Athens, Greece, Sept. 15-17, 1980, pp. 860-867.

[19] E.A. Klingshirn, “High phase order induction motors – Part II – Experimental results,” *IEEE Trans. Power App. Syst.*, vol. PAS-102, pp. 54–59, Jan. 1983.

[20] M. A. Abbas, R. Christen and T.M. Jahns, “Six-phase voltage source inverter driven induction motor,” *IEEE Trans. Ind. Appl.*, vol. 20, pp.1251-1259, Sept./Oct. 1984.

[21] Y. Zhao and T.A. Lipo, “Space vector PWM control of dual three-phase induction machine using space vector decomposition,” *IEEE Trans. Ind. Appl.*, vol. 31, pp.1100-1109, Sept./Oct. 1995.

[22] E. Levi, R. Bojoi, F. Profumo, H.A. Toliyat and S. Williamson, “Multiphase induction motor drives - a technology status review,” *Elec. Power Appl., IET,* vol. 1, no. 4, pp.489-516, Jul. 2007.

[23] G.K. Singh, K. Nam and S.K. Lim, “A Simple Indirect Field-Oriented Control Scheme for Multiphase Induction Machine,” *IEEE Trans. Ind. Electron.*, vol. 52, no. 4, pp. 1177- 1184, Aug. 2005.

[24] R. Bojoi, F. Profumo and A. Tenconi, “Digital synchronous frame current regulation for dual three-phase induction motor drives,” *Proc. IEEE-PESC’03*, vol. 3, pp. 1475–1480, Jun. 2003.

[25] R. Bojoi, E. Levi, F. Farina, A. Tenconi, F. Profumo and, “Dual three-phase induction motor drive with digital current control in the stationary reference frame,” *IEE Proc. Elec. Power Appl*, vol.153, no.1, pp. 129- 139, Jan. 2006.

[26] R. Bojoi, F. Farina, M. Lazzari, F. Profumo and A. Tenconi, “Analysis of the asymmetrical operation of dual three-phase induction machines,” *IEEE IEMDC'03*, vol.1, pp. 429- 435, Jun. 2003.

[27] B. Farid and O. Amar, “A study of new techniques of controlled PWM inverters,” *European Journal of Scientific Research*, vol. 32, no. 1, pp. 77-87, Jun. 2009.

[28] S. Williamson, S. Smith and C. Hodge, “Fault tolerance in multiphase propulsion motors,” *Proc. IMarEST - Part A*, vol. 2004, no. 4, pp. 3-7, Mar. 2004.

[29] J.M. Apsley, “Open-circuit fault mitigation for multiphase induction motors with a unified control structure,” *5th IET Int. Conf. PEMD 2010*, pp.1-6, Apr. 2010.

[30] G. Grandi, Y. Gritli, F. Filippetti and C. Rossi, “Fault-tolerant operating analysis of a quad-inverter multiphase multilevel AC motor drive,” *IEEE Int. Symp. SDEMPED,* pp.126-132, Sept. 2011.

[31] A.E. Fitzgerlad, C. Kinglsley, Jr. and S.D. Umans, *Electric Machinery*, 3rd ed., McGraw-Hill, 2003, pp. 306-307.

[32] P.C. Sen, *Principles of Electric Machines and Power Electronics*, 2nd ed., John Wiley & Sons, 1997, pp. 207.

[33] N. Mohan, *Electric Drives: An Integrative Approach.* MNPERE, 2003, pp. 4-1 – 4-23.

[34] N. Mohan, T.M. Undeland and W.P. Robbins, *Power Electronics: Converters, Application, and Design*, 3rd ed., John Wiley & Sons, Inc., 2003, pp. 225-229.

[35] N. Mohan, *Advanced Electric Drives: Analysis, control and Modeling using Simulink.* MNPERE, 2001, pp. 7-9 – 7-10.

[36] J.A. Houldsworth and D. A. Grant, “The use of harmonic distortion to increase the output voltage of a three-phase PWM inverter,” *IEEE Trans. Ind. Appl.*, vol. IA-20, no. 5, pp.1224-1228, Sept. 1984.

[37] T.F. Nestli, R. Nilsen, "Evaluation and comparison of predictor models for rotor flux calculation in induction motors," *Proc. IEEE-PESC'94*, vol. 1, pp. 729–737, Jun. 1994.

[38] N.A. Ayehunie, "MultiPhase Permanent Magnet Synchronous Generators for Offshore Wind Energy System: Control of six phase PMSG – six leg converter system," Master thesis, Dept. Elect. Power Eng., NTNU, Trondheim, Aug. 2011.

[39] R. Nilsen, *Elektriske Motordrifter*, Kompendium, Institutt for Elkraftteknikk, NTNU, Trondheim, 2004, pp. 102 - 212.

[40] K. Ogata, *Discrete-time Control Systems*, Prentice-Hall, Inc., 1995, pp. 74 – 292.

[41] J.A. Suul, M. Molinas, L. Norum and T. Undeland, "Tuning of Control Loops for Grid Connected Voltage Source Converters," *2nd IEEE Int. Conf. on Power and Energy*, pp. 797-802, Dec. 2008.

[42] J.W. Umland and M. Safiudin, "Magnitude and Symmetric Optimum Criterion for the Design of Linear Control Systems: What is it and how does it compare with the others?," *IEEE Ind. Appl. Soc. Annu. Meeting*, pp. 1796-1802, 1988

[43] T.F. Nestli, "Modulus and Symmetric Optimum Critera for the Design of Linear Control Systems," Memo, Dept. Elec. Power Eng., NTNU, Trondheim, Mar. 2010.

[44] N.P. Quang and J.-A. Dittrich, *Vector Control of Three-Phase AC Machines: System Development in the Practice*, Springer, 2008, pp.204 – 208.

[45] H. Kolstad and K. Ljøkelsøy, "20 kW IGBT omformer. Beskrivelse," Arbeidsnotat: an 01.12.12, SINTEF Energiforskning AS, Trondheim, Norway, Sept. 2002.

[46] K. Ljøkelsøy, "Processorkort bassert på Xilinx Virtex5 FPGA. V1. 1. Beskrivelse," Arbeidsnotat: AN 09.12.14, SINTEF Energiforskning AS, Trondheim, Norway, Feb. 2009.

[47] K. Ljøkelsøy, "Library of IP modules, building blocks for FPGA based converter control system," Project Memo: AN 10.12.66, SINTEF Energy Research, Trondheim, Norway, Jun. 2010.

[48] LEM, "Current Transducer LA 205-S," LA 205-S datasheet, Available: http://www.lem.com/docs/products/la%20205-s.pdf

[49] LEM, "Voltage Transducer LV 25-600," LV 25-600 datasheet, Available: http://www.lem.com/docs/products/lv%2025-600%20sp2.pdf

[50] Heidenhain , “Rotary Encoders,” datasheet, Apr. 2005.

[51] ActveDSP AS, “ActiveDSP: A Tool for Real Time Monitoring, Operation and Maintenace of Embedded Systems,” User Manual, 2008.

[52] DRIVECOM Nutzergruppe e.V., “DRIVECOM Profile Drive Engineering 22,” May 1995.

Appendix

A Six-Phase Induction Machine Nameplate Data

The manufacturer's nameplate data of the six-phase induction machine used in the experiment are given in the table below:

Parameter	**Explanation**	**Value**
U_N	Nominal line to line voltage [V_{rms}]	400 V
I_N	Nominal line current [A_{rms}]	11.8 A
f_N	Nominal frequency [Hz]	75 Hz
p	Number of pole pairs	2
n_N	Nominal speed [mechanical rpm]	2235 rpm
M_N	Nominal output torque [Nm]	50 Nm
P_N	Nominal power output [kW]	11.7 kW
$cos\varphi_N$	Nominal power factor	0.77
n_{MAX}	Maximum speed [mechanical rpm]	5000

Table A.1: Six-phase induction machine nameplate data

B Per Unit system

The per unit system used in the implementation of the system are given in The base (reference) values are based on the following three nominal quantities obtained from the nameplate of the six-phase induction machine given in Appendix A:

1. U_N, the nominal line-to-line voltage
2. I_N, the nominal stator line current
3. f_N, the nominal stator frequency

Physical quantity	Base quantity definition	Value of base quantity
AC Voltage	$U_n = \sqrt{2} \cdot \frac{U_N}{\sqrt{3}}$	326.6 V
DC link voltage	$U_{dc,n} = 2 \cdot \sqrt{2} \cdot \frac{U_N}{\sqrt{3}}$	653.2 V
Current	$I_n = \sqrt{2} \cdot I_N$	16.7 A
Impedance	$Z_n = \frac{U_n}{I_n}$	19.56 Ω
Power	$S_n = 2 \cdot \sqrt{3} \cdot U_N \cdot I_N$	16.351 kW
Frequency	$f_n = f_N$	75 Hz
Angular speed (electrical)	$\omega_n = 2 \cdot \pi \cdot f_N$	471.24 $^{rad}/_{s}$
Speed (mechanical)	$n_n = 60 \cdot \frac{f_N}{p}$	2250 rpm
Torque	$M_n = p \cdot \frac{S_N}{\omega_n}$	69.4 Nm
Flux linkage	$\Psi_n = \frac{U_n}{\omega_n}$	0.693 Wb

Table B.1: Per unit system

C Six-Phase Induction Machine Equivalent Circuit Parameters

A method of calculating three-phase induction machine circuit parameters from the nameplate data is given in [44]. The method uses inverse-Γ equivalent model of induction machine. This method is adapted to estimate parameters of the six-phase induction machine. Only the stator resistance was estimated experimentally using DC resistance measurement and averaging the phase resistances. Experimental identification of the other parameters is beyond the scope of this work. The values are scaled according to the per unit system used in this thesis.

Parameter	**Value [pu]**
r_s	0.031
r_R	0.0068
x_s	2.086
x_σ	0.2175
x_H	1.8685
σ_r	0.0566

Table C.1: Circuit parameters of six-phase induction machine

D Control Parameters

The PI controller time constants in the following tables are expressed as the sampling time divided by the actual time constant for digital implementation. The sampling times are given in each table.

Parameter	**Value**
K_{pd}	0.15
K_{pq}	0.13
K_{pz1}	0.1
K_{pz2}	0.1
$Ts\_div\_T_{id}$	0.07
$Ts\_div\_T_{iq}$	0.045
$Ts\_div\_T_{iz1}$	0.04
$Ts\_div\_T_{iz2}$	0.04
$T_{samp,i}$	(1/3000) sec
$f_{c,i}$	1 kHz

Table D.1: SSFC current controller parameters

Parameter	**Value**
K_{pd1}	0.12
K_{pq1}	0.12
K_{pd2}	0.12
K_{pq2}	0.12
$Ts\_div\_T_{id1}$	0.050
$Ts\_div\_T_{iq1}$	0.050
$Ts\_div\_T_{id2}$	0.050
$Ts\_div\_T_{iq2}$	0.050
$T_{samp,i}$	(1/3000) sec
$f_{c,i}$	1 kHz

Table D.2: DSFC current control parameters

Parameter	**Value**
K_ψ	18.11
Ts_div_$T_{i\psi}$	0.035
K_n	12.0
Ts_div_T_{in}	0.082
T_{samp}	(1/300) sec

Table D.3: Parameters of outer (flux and speed) controllers

Parameter	**Value**
f_{sw}	3 kHz
T_v	0.1667 ms
$u_{st,max}$	1.15

Table D.4. Inverter parameters

E Additional Results in SSFC

I. Speed Control

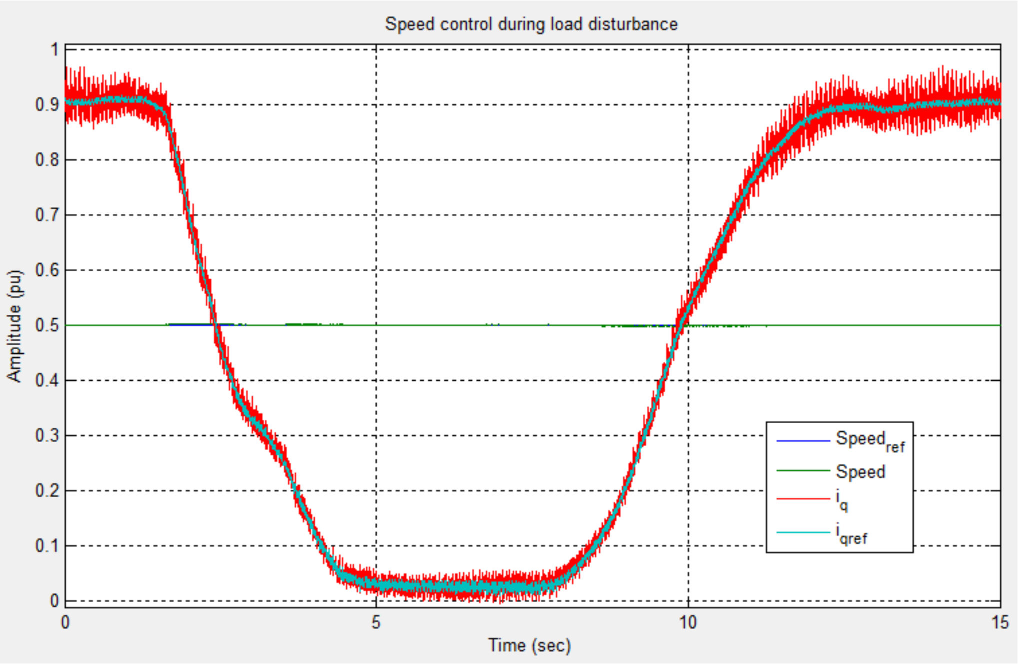

Figure E.1: Speed control during load disturbance

Speed control under load disturbance with speed control at 0.5 pu is given above. Load torque is varied by varying the field voltage of the DC machine.

II. Rectifier turn off and DC link loss

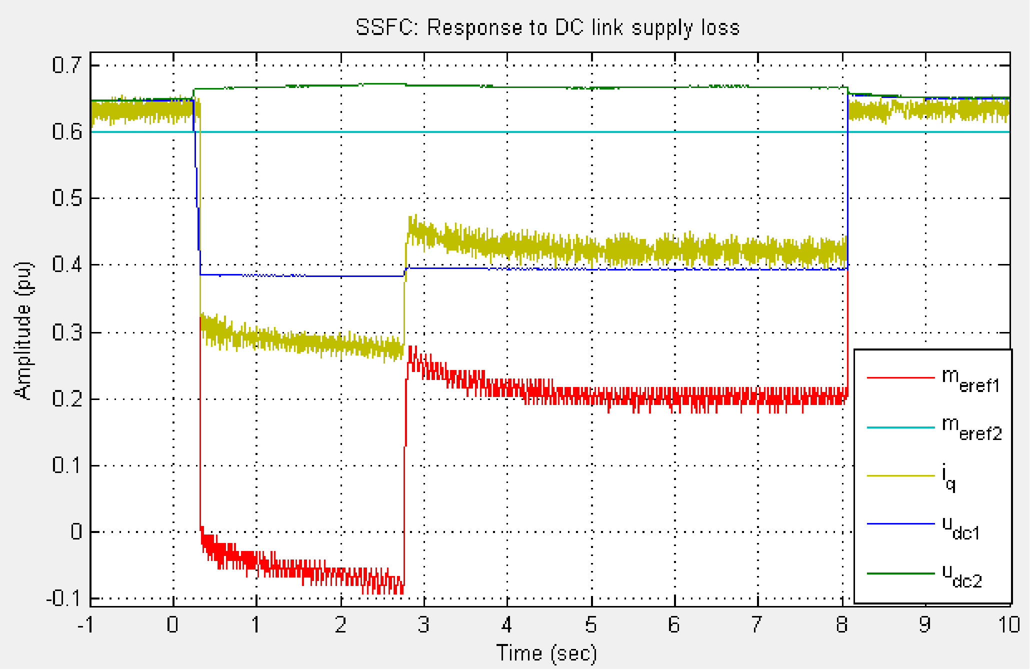

Figure E.2: Rectifier turn off and on

III. Inverter trip

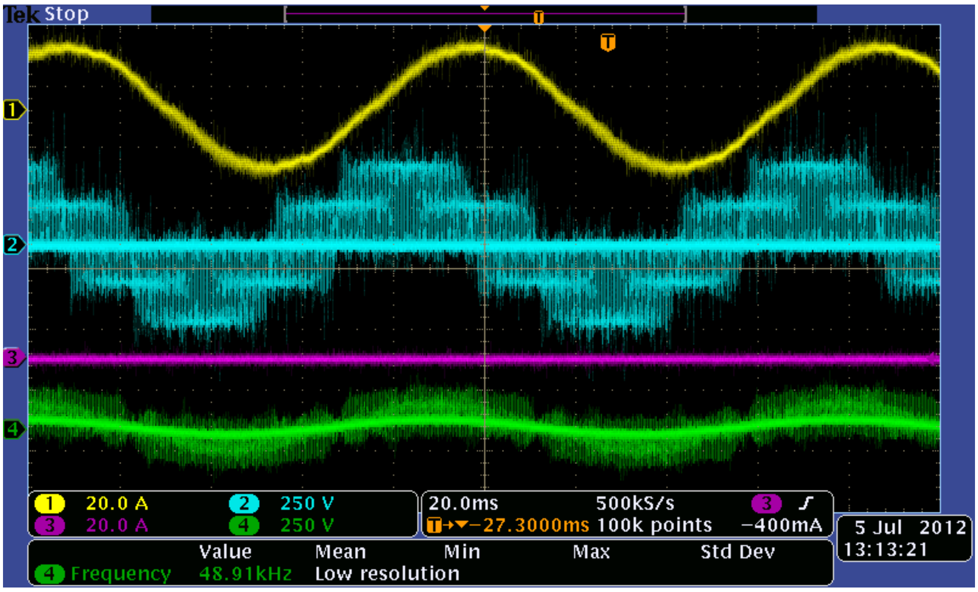

Figure E.3: Phase currents and voltages after trip of inverter 2

F Additional Results in DSFC

I. Speed control

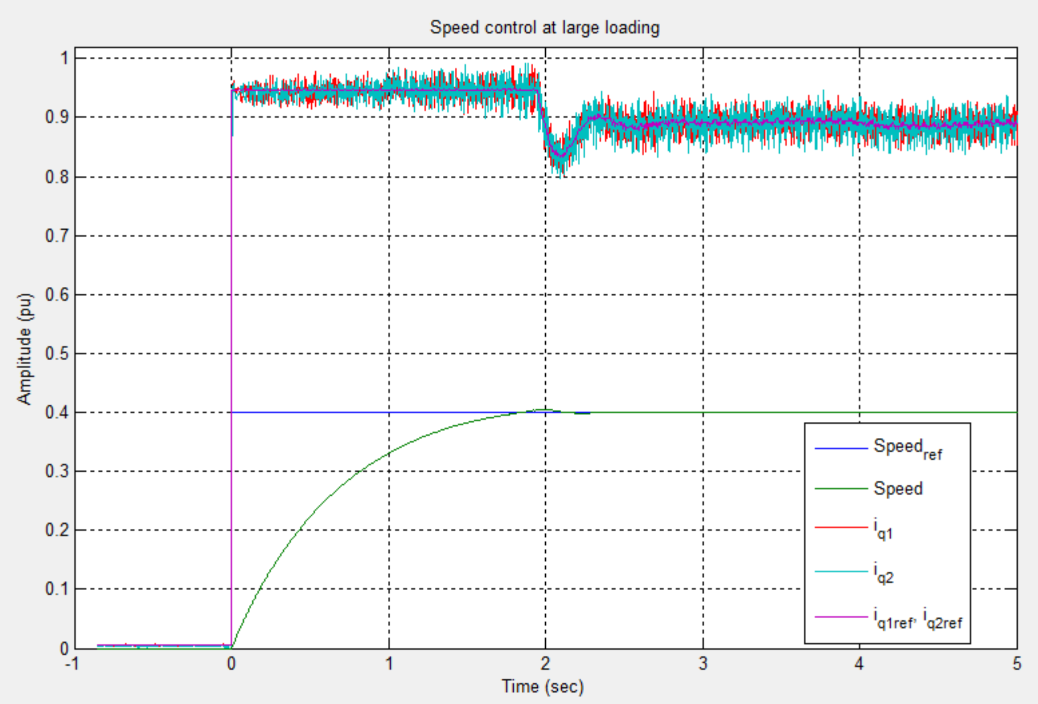

Figure F.1: Speed control in loaded machine

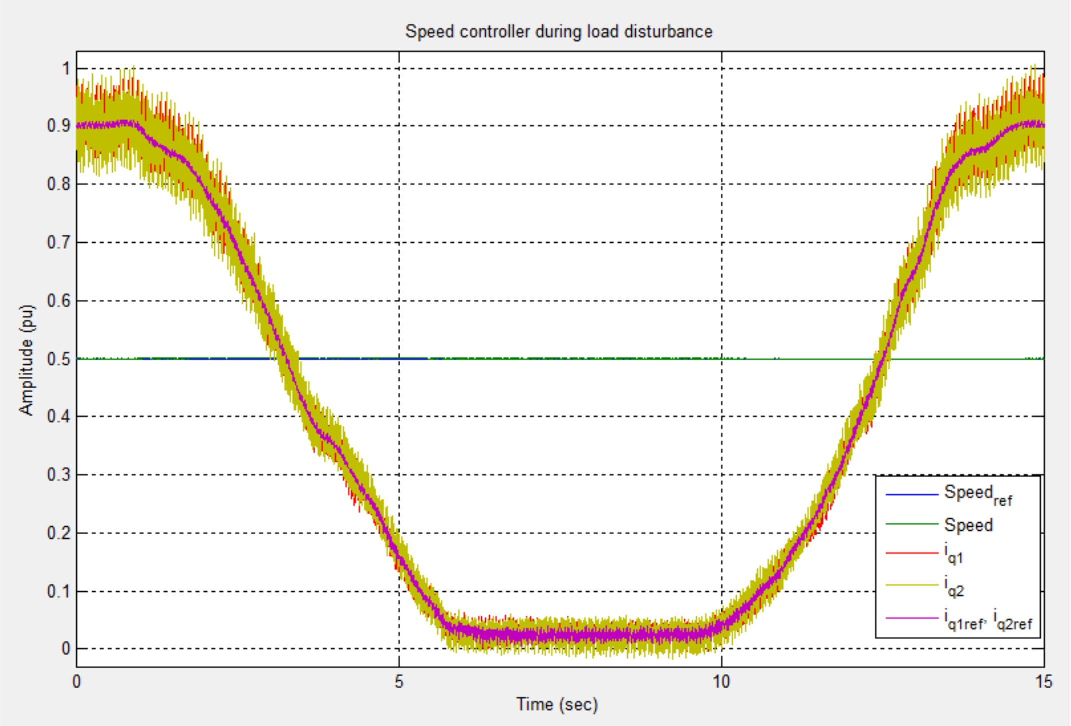

Figure F.2: speed control during load disturbance

II. DC link undervoltage

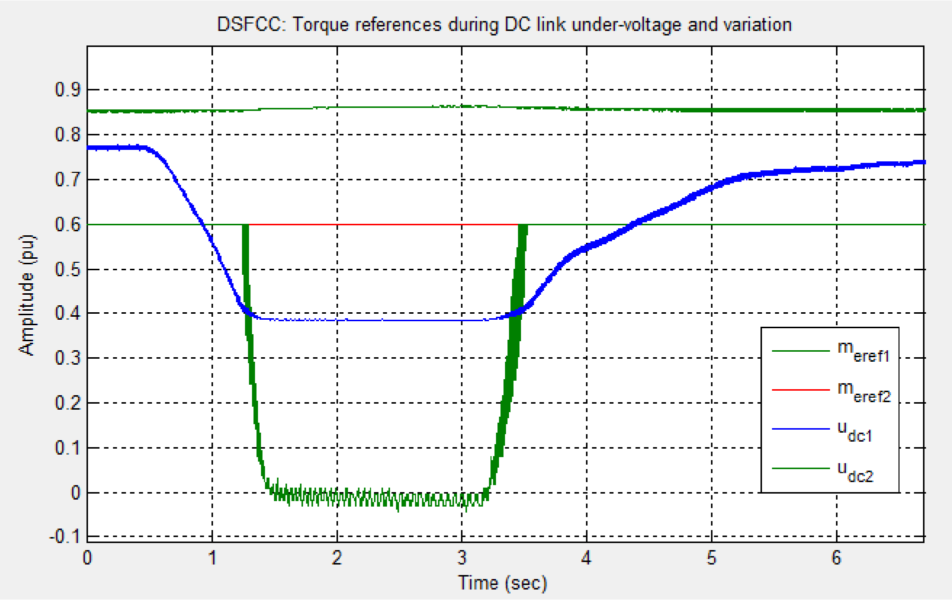

Figure F.3: Torque references during DC link undervoltage

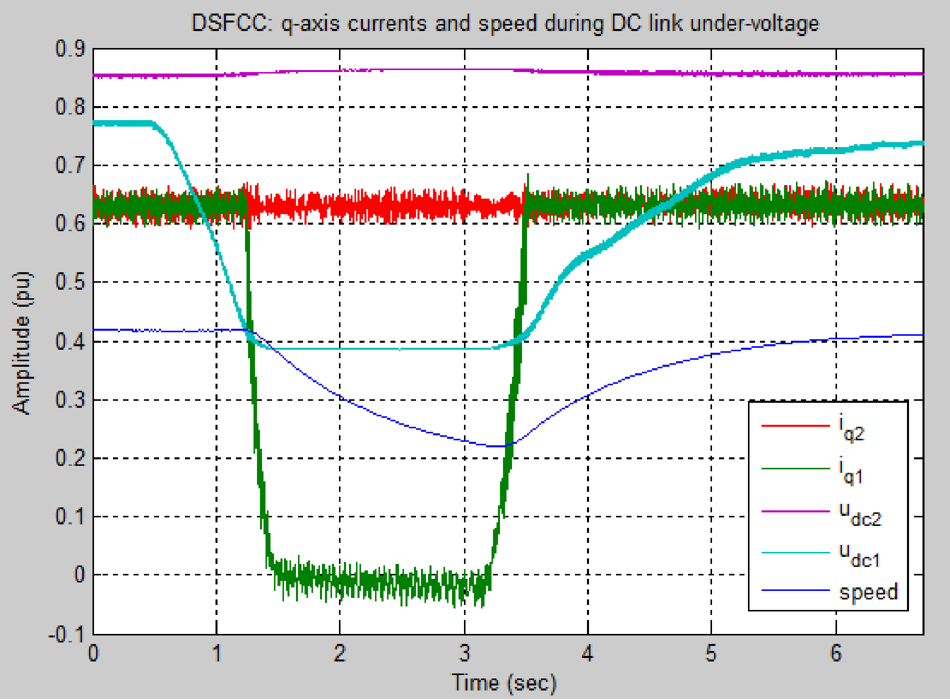

Figure F.4: Currents during DC link undervoltage